Abstract

Structural Studies of Actin-Binding Proteins Involved in Actin Dynamics, Organization, and Force Sensing

Andrew Robert Huehn

2020

Actin represents one of the three main cytoskeletal filaments and plays a key role in forming cell structure, cell motility, intracellular transport, cytokinesis, and many other biological activities (2). Its role in these diverse processes is accomplished with the fine regulation of actin dynamics and organization and through interactions with numerous actin-binding proteins. However, due to the filamentous nature of actin, high resolution structural information on proteins directly interacting with the filament have long eluded researchers, limiting our understanding. Fortunately, recent developments in cryo-electron microscopy (cryo-EM) (4) have enabled us to analyze these structures in atomic detail. My thesis details the results of several collaborations where we leveraged our expertise and developed new methods in cryo-EM to study actin-binding proteins that regulate, organize, or interact with actin to perform specialized functions.

The first chapter of my thesis focuses on a the published results (5, 6) of a collaboration with the De La Cruz laboratory at Yale University on the protein cofilin, a key regulator of actin. Cofilin severs actin filaments, increasing the number of filament ends available for polymerization or depolymerization, thus modulating the overall turnover rate of actin networks (7, 8). Cofilin binds actin filaments with positive cooperativity, forming clusters of contiguously bound cofilin (cofilactin) along the filament lattice (9, 10). Cooperative binding has been proposed to originate from conformational changes that propagate allosterically from clusters of bound cofilin to bare actin segments (11), although estimates of the length scale over which

these changes propagate vary dramatically (8, 9, 12-20). In addition, filament severing occurs preferentially at or near these boundaries (8, 9, 21-23) and is biased at one side of a cluster (24, 25). However, a molecular understanding of cooperative binding and filament severing has been impeded by a lack of structural data describing boundaries. Here, I analyze partially-decorated cofilactin filaments using new methods for filament cryo-EM data to reveal how far allosteric, conformational changes propagate from boundaries by tracking small variations in filament geometry (e.g. twist) and directly investigate boundary structures. My results demonstrate that cofilin-induced changes in filament twist propagate only 1-2 subunits from the boundary into the bare actin segment, independent of the boundary polarity. Furthermore, sub-nanometer resolution maps of isolated, bound cofilin molecules and an actin-cofilactin boundary indicate that cofilin-induced actin conformational changes are local and limited to subunits directly contacting bound cofilin. Comparison of these structures indicates that filament disruption is substantially greater at pointed end sides of cofilactin clusters than at the barbed end. These results reveal the structural origins of cooperative cofilin binding and actin filament severing.

The second chapter of my thesis details the published results (26) of a collaboration with the Calderwood laboratory at Yale University on the actin crosslinking protein Filamin A (FLNa). FLNa is a homodimer that organizes actin filaments into orthogonal arrays (27) and serves as a scaffold for numerous other actin-interacting partners (28). The actin-binding domain of FLNa is composed of tandem calponin homology (CH) domains (29-32), where missense mutations underlie numerous genetic diseases (29, 30, 33). We combine cryo-EM and functional studies to reveal at near-atomic resolution how the first CH domain (CH1) and residues immediately N-terminal to it engage actin. We further show that reorientation of CH2 relative to CH1 is required to avoid clashes with actin and to expose F-actin-binding residues on CH1. Our data

explain localization of disease-associated loss-of-function mutations to FLNaCH1 and gain-of-function mutations to the regulatory FLNaCH2.

The third chapter of my thesis details the published results (34) of a collaboration with the Ostap and Shuman laboratories at the University of Pennsylvania on myosin-IB, a molecular motor from the myosin superfamily that functions as a tension-sensitive anchor (35). We reveal the structural basis for myosin's force-sensing mechanism based on high-resolution structures of actin-bound states of myosin-IB determined by cryo-EM. We describe an allosteric pathway that links the release of MgADP to a rotation of the myosin lever arm via a mechanism unlike that reported for the initial force-generating power stroke, and we identify a structural component that stabilizes the rigor-like orientation of the lever in both the MgADP-bound and rigor states. We further show structural diversity in the actomyosin binding site, and we reveal the high-resolution structure of actin-bound phalloidin. The results provide a framework to understand the spectrum of force sensing capacities among the myosin superfamily.

In light of the independence of these topics, each chapter includes its own separate introductory section.

Structural Studies of Actin-Binding Proteins Involved in Actin Dynamics, Organization, and Force Sensing

A Dissertation

Presented to the Faculty of the Graduate School of Yale University

In Candidacy for the Degree of Doctor of Philosophy

By

Andrew Robert Huehn

Dissertation Director

Professor Charles V. Sindelar

May 2020

Table of Contents

List of Figures

List of Tables

Acknowledgements

First and foremost, I give my thanks to my wife, Titilayo Omotade, for her boldness, compassion, insight, humor, and love. It's no exaggeration to say I would be lost without her, and to stand alongside her is my greatest source of pride. We were blessed to be able to enter our graduate programs together and support each other throughout the journey. I also thank my family, my parents Donald Barry Huehn and Loraine Proska, and my brother Scott, to whom I owe everything and love deeply.

I'm deeply grateful to my advisor Dr. Charles Sindelar, who was an excellent mentor and friend in lab, and a source of constant enthusiasm and inspiration. I'm also greatly indebted to the members of the Sindelar lab - Kimberley Gibson, Garrett Debs, Megan Brady, Drs. Kirill Grushin and Xueqi Liu, as well as former graduate students Drs. Michael Hyo Keun Cha and Daifei Liu. Their support was invaluable to me as a graduate student, and their kindness made lab feel like a second home. I'm also thankful to my committee members Drs. Fred Sigworth and Enrique De La Cruz for all their encouragement and advice.

I'm grateful to the cohort of students who entered the program together with me. I was blessed to study and work alongside creative, funny, kind, and hard-working people, and I regret that I didn't make more time to get to know them better. I'm also thankful to our department as a whole - it has been a wonderful home to learn and grow in as a scientist. The collaborative and intellectually stimulating atmosphere that has been cultivated in our department is something I hope to find again in the future.

Finally, I'm thankful to the collaborators with whom I had the exceeding good fortune to work with during my graduate training. I worked with Dr. Enrique De La Cruz and his lab members Drs. Wenxiang Cao, Jeffrey Bibeaux, and W. Austin Elam on the cofilin project, Dr.

David Calderwood and his former graduate student Dr. Daniel Iwamoto from Yale University on the filamin project, and Drs. Michael Ostap, Henry Shuman, and Ahmet Mentes from the University of Pennsylvania on the myosin-IB project. Their insight, expertise, and dedication were a privilege to work beside.

Chapter I. Actin changes conformation abruptly at cofilin decorated boundaries

Introduction

Members of the cofilin/ADF family of actin regulatory proteins (7, 36) bind actin filaments cooperatively (8-10) and promote severing preferentially at and near junctions between bare and cofilin-decorated (cofilactin) segments (8, 9, 11, 21, 22), hereafter referred to as boundaries. Cofilin alters the average actin filament twist (37) and subunit tilt (1, 38). Bound cofilin molecules do not directly interact with one another (37), indicating that cooperative binding originates from allosteric conformational changes that propagate from bound cofilin(s) to vacant sites. Current models posit that this propagation occurs via allosteric alterations in filament twist ((11) and references therein), which is strongly linked to cofilin decoration.

Estimates of the length over which cofilin-induced conformational changes and cooperative binding interactions propagate along actin vary, ranging from N = 1-2 up to N > 100 subunits (8, 9, 12-20). Equilibrium (9, 12, 21, 39) and transient kinetic (12, 14) binding data are well described by models invoking positive cooperativity between nearest neighbors (N = 1-2). In contrast, differential scanning calorimetric (13) and spectroscopic lifetime (15) measurements estimate allosteric propagation of changes in structure, stability, and/or dynamics over N > 100 subunits. More recently, a single-molecule TIRF study measured positive cooperative binding interactions that propagated exponentially with a decay length of N ~24 subunits (18), and atomic force microscopic imaging directly observed a change in the crossover distance of N ~14 bare actin subunits towards the pointed-end side of the boundary, but no propagation in the bare actin subunits towards the barbed-end side of the boundary (11).

Severing occurs preferentially at boundaries (8, 9, 21-23), where structural and mechanical discontinuities exist (8, 23, 40). Cluster growth (11) and filament severing (24, 25, 41) is biased and occurs more readily at the pointed end side of clusters compared to the barbed end side.

These activities of cofilin are regulated by phosphorylation; phospho-cofilin and phosphomimetic mutants bind and sever filaments weakly (19).

Previous cryo-EM studies of stable, saturated cofilactin filaments revealed that cofilin binds between longitudinal neighboring actin subunits and rotates the outer domain of actin with respect to the inner domain (1, 38, 42). This subunit tilting displaces the actin D-loop, compromising longitudinal subunit interactions (1, 38, 42, 43). Bound cofilins bridge neighboring actin filament subunits, compensating for the loss of stabilizing D-loop interactions. Despite this extensive research, our understanding of the molecular mechanism of cooperative cofilin binding and filament severing has been limited by lack of structural data and atomic level models of individual, bound cofilin and boundaries where severing occurs. These structures have remained elusive due to their scarcity as well as ongoing challenging in 3D reconstruction of helical assemblies with introduced asymmetry (*e.g.* boundaries).

Here, I describe the published results of my research on the extent of allosteric propagation from boundaries (44) and structural intermediates (6) from an extensive collaboration with the De La Cruz laboratory at Yale University. First, I developed a procedure to analyze electron cryo-micrographs of actin filaments that captures the position, orientation, and cofactor (e.g. cofilin) binding occupancy of individual filament subunits. This procedure allowed us to establish with single subunit precision the allosteric propagation of filament twist induced by cofilin binding. Our analysis indicates that cofilin-linked changes in actin filament twist are local and propagate allosterically over a distance of only N = 1–3 subunits. Next, I developed models of single, bound cofilin and cofilactin boundaries at sub-nanometer resolution, which has allowed us to directly investigate conformational states that promote severing and cooperative binding.

Results

Procedure for deriving filament geometry and cofilin occupancy from electron micrographs

I acquired a set of 197 micrographs of pyrene-labeled actin filaments partially decorated with cofilin at a binding density (v) of ~0.5 cofilin per actin subunit, and a second set of 500 micrographs of a similarly prepared sample but with unlabeled actin filaments. I manually identified boundaries between bare and cofilin-decorated segments from changes in the width and helical pitch of filaments (Fig. 1G). We limited our analysis to boundaries defined by contiguous clusters of bound cofilin (N > 20) that were distinguishable by eye; smaller clusters are subject to corruption from background noise levels inherent to cryo-EM. Because of the limited field of view at the magnification used here (0.5 µm x 0.5 µm), only one end of a given cofilin cluster was ever seen and filament ends were rarely observed. We analyzed 64 total boundaries with unlabeled actin: 57 with bare actin flanking the barbed end side of the cluster, and 7 with bare actin flanking the pointed end side; and 28 total boundaries with pyrene-labeled actin: 24 with bare actin flanking the barbed end side of the cluster, and 4 with bare actin flanking the pointed end side. All boundaries were validated objectively through single particle 3D classification analysis (discussed below).

Imaged filaments were divided into square, overlapping segments (repeating distance ~N = 1 filament subunit, dimensions ~N = 12 subunits) and processed using the IHRSR single-particle helical refinement method (45, 46), as implemented in the RELION software package (47, 48), to generate a 3D filament reconstruction (nominal resolution 8.3 Å). Bare and cofilin-decorated filament segments were included in the reconstruction, to preserve the geometric relationship between all subunits in a given filament, and thus allow the relative positions of all subunits to be calculated. The resulting hybrid map (Fig. 1B) exhibits features of both actin and cofilactin filaments. Accordingly, the density of bound cofilin is substantially weakened in this map (Fig.

1B). Moreover, the helical twist of this map (-163.9˚) is intermediate between the reported canonical (average) twist of cofilactin (-162.3˚; (1)) and bare actin (-166.6˚; (49)), because actin and cofilactin filament segments were present at approximately equal mole fractions.

In order to measure the filament twist as a function of subunit number (i.e. axial position along the actin filament), I used alignment parameters from the preceding analysis of filament segments to generate subunit-by subunit coordinate models of each imaged filament, after filling in gaps (length $\leq$ 1-2 subunits) using an interpolation scheme (Fig. 1H; see Methods). This approach differs from the usual method for 3D structure determination of heterogeneous filaments by cryo-EM, in which multiple, distinct reference volumes are used to sort boxed segments into different conformational classes during structure refinement, and geometric relationships between neighboring filament segments are not considered (45). In contrast, by performing a global alignment with a single common reference volume as done here, the geometries of actin subunits in neighboring filament segments can readily be related to each other– even when traversing boundaries between bare and decorated regions.

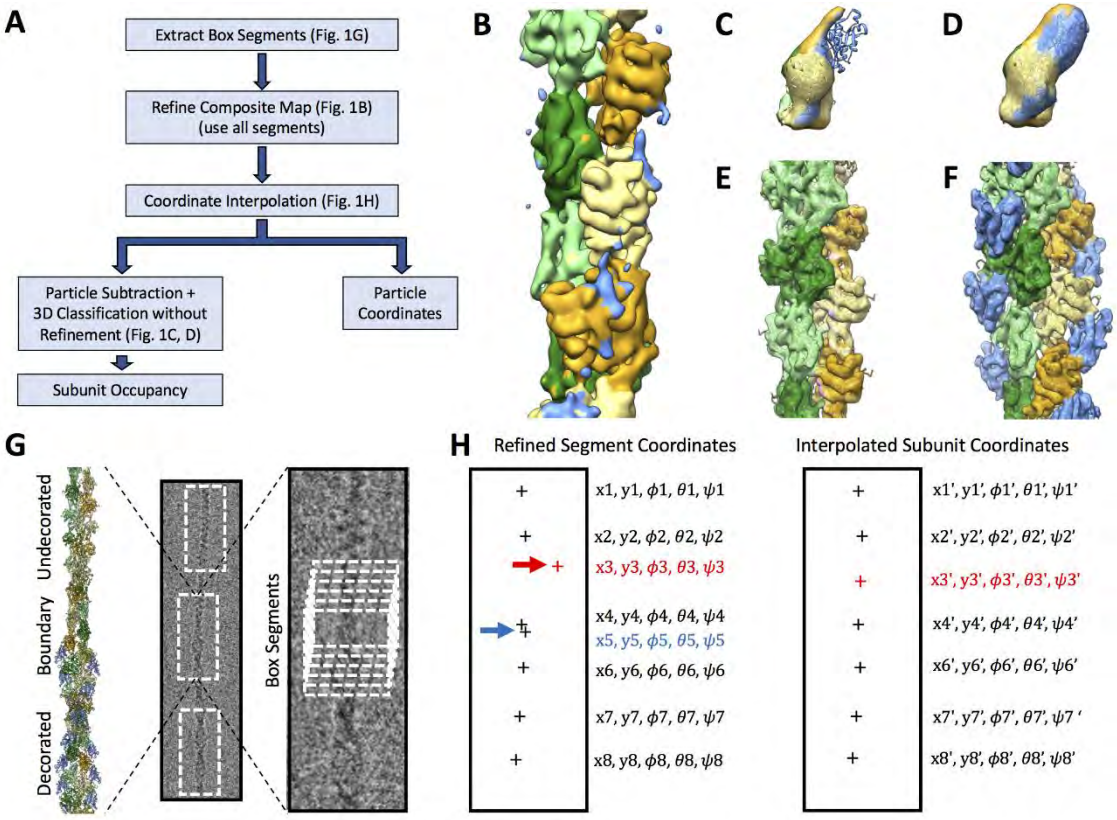

Figure 24. Identification of cofilin boundaries in cryo-EM micrographs of partially decorated actin. A, Flow chart of the procedure used in the current work for analysis of actin filaments heterogeneously decorated by cofilin. B, Electron cryo-microscopy structure composite generated using all filament segments, representing a mixed population of (equimolar) bare and cofilin-decorated subunits. C – D, The two predominant structural classes obtained by reference-free masked 3D classification of individual subunit sites, corresponding to bare (left) and cofilin-decorated (right) actin. E – F**,** Unmasked reconstructions of the bare (E) and cofilactin (F) classes, corresponding to the assigned classes illustrated in (C) and (D), respectively. G, Illustrative heterofilament model (left) built from cofilactin (PDB code 3J0S (1)) and bare actin (PDB ID 3J8I (3)) structures. Cofilin is colored blue; actin is colored in shades of green and orange. Representative cryo-EM image (middle) of a boundary between bare (top) and cofilin-decorated (bottom) regions, and a close-up of the boundary region (right). H, Schematic depiction of the coordinate interpolation process, starting with coordinates of filament segments derived from the first refinement step (left) in which some subunits may be represented by multiple segments (blue arrow) while others are represented poorly or not at all (red arrow) due to refinement errors. Following interpolation and smoothing (see Methods), the resulting subunit coordinates more closely represent the true geometry of the filament (right).

Notably, the quality of the resulting 3D 'hybrid' map is compromised due to mixing of different structural states of the filament. Nevertheless, alignments obtained by this approach for a given filament segment are expected to register the position and orientation of subunit(s) located near the center of the segment. In this way, alignment information from neighboring segments can be merged by our interpolation scheme in order to model the position and orientation of each subunit within an imaged filament. Moreover, as demonstrated below, alignments produced by this analysis can subsequently be used to perform structural classification at the level of single subunits. Thus, highly detailed descriptions of individual filaments can be obtained by combining the above two types of information (position/orientation, and structural classification) at the subunit level. Importantly, distinct structural classes can subsequently be reconstructed in 3D by separating, reprocessing and/or re-refining the corresponding image segments to potentially achieve higher resolution than the original hybrid map. Each of these properties of our method is illustrated below.

Structural classification of individual subunits

To distinguish cofilin-decorated from bare actin subunits, while ensuring that every filament subunit is included in the classification, I re-extracted a new set of filament segments from the micrographs using subunit-by-subunit coordinate models derived above. I then performed a focused 3D classification by subtracting all but the central subunit from image segments using a masked reference volume (see Methods).

This procedure yielded bare and cofilin-decorated classes (Fig. 1C, D), with approximately half of the subunits assigned to each class. As a qualitative check of classification accuracy, I performed separate, unmasked reconstructions of each class. The cofilactin class (Fig. 1E) refined to 7.9 Å, while the bare actin class (Fig. 1F) refined to 8.3 Å. The resulting maps (Fig. 1E,

F) exhibit density features and helical geometries indistinguishable from previously determined structures of actin (3, 50) and cofilactin (1) filaments, indicating that the classification assignments used here were accurate.

Method for detection of small variations in filament twist

The filament twist is defined by the difference in axial rotation angles between adjacent filament subunits (following the genetic, one start helix of actin filaments), where estimates of these axial rotation angles are taken from the Euler angles recorded during 3D structure refinement. Summing the twist values from our filament coordinate model yields the cumulative subunit rotation as a function of filament length. An important feature of this summation is that its uncertainty is independent of sample size (i.e. filament length), due to cancellation of all terms except those belonging to the first and last subunits. Viz., if we let ϕ represent the measured axial orientation of a given subunit with uncertainty σ, then the cumulative subunit rotation for a filament of length *N* is estimated by $(\phi_N - \phi_{N-1}) + (\phi_{N-1} - \phi_{N-2}) + \ldots + (\phi_2 - \phi_1)$. This sum reduces to $(\phi_N - \phi_1)$ with uncertainty $\sqrt{\sigma_N^2 + \sigma_1^2}$, according to error propagation, thus eliminating all other terms and their associated uncertainties. In other words, the uncertainty of a given sum depends only on the uncertainties associated with the first and the last subunits being considered. Moreover, because the sum scales linearly with filament length while its uncertainty does not, the *relative* uncertainty in the average cumulative subunit twist decreases linearly with filament segment length. Thus, cumulative subunit rotation is an exceptionally sensitive indicator of variations in twist along a filament.

For purposes of presentation and to emphasize features of the transition region, we subtracted the cumulative twist of bare actin from the cumulative subunit rotation to obtain a 'cumulative twist difference' (Fig. 2A). Given this definition (i.e. bare actin subtraction), bare

actin segments exhibit no cumulative twist difference (e.g. left-hand portion of the graph of Fig. 2A), whereas the overtwist of cofilactin segments gives rise to a positive cumulative twist difference (e.g. positive slope in the right-hand portion of Fig. 2A).

Changes in filament twist occur abruptly and bidirectionally at boundaries

The cumulative twist difference displays an abrupt transition at boundaries between bare and cofilin-decorated segments within an individual filament (Fig. 2A). Averaging this quantity over many boundaries reduces the noise and reveals that this structural transition occurs (on average) over a length of 0.78 ± 0.04 subunit at the barbed end side of cluster (n = 57) and 1.6 ± 0.5 subunits at the pointed end side (n = 7) for unlabeled actin, and a length of 1.1 ± 0.1 (n = 24) subunit at the barbed end side of cluster (Fig. 2C) and 1.9 ± 0.3 (n = 7) subunits at the pointed end side (Fig. 2D) for pyrene-labeled actin. This observation indicates that allosteric propagation of the cofilactin twist into the bare actin segment occurs bidirectionally, with minimal differences between the barbed and pointed-end sides of the cofilin clusters.

The twist change at a given boundary appears to also spread bidirectionally into the bare and cofilin-decorated segments, as determined from the best fit of the data (Fig. 2E and F). That is, the midpoint of the 'twist transition' lies between the bare and cofilin-decorated filament segments, extending ~1 subunit to each side of the boundary (Fig. 2E and F).

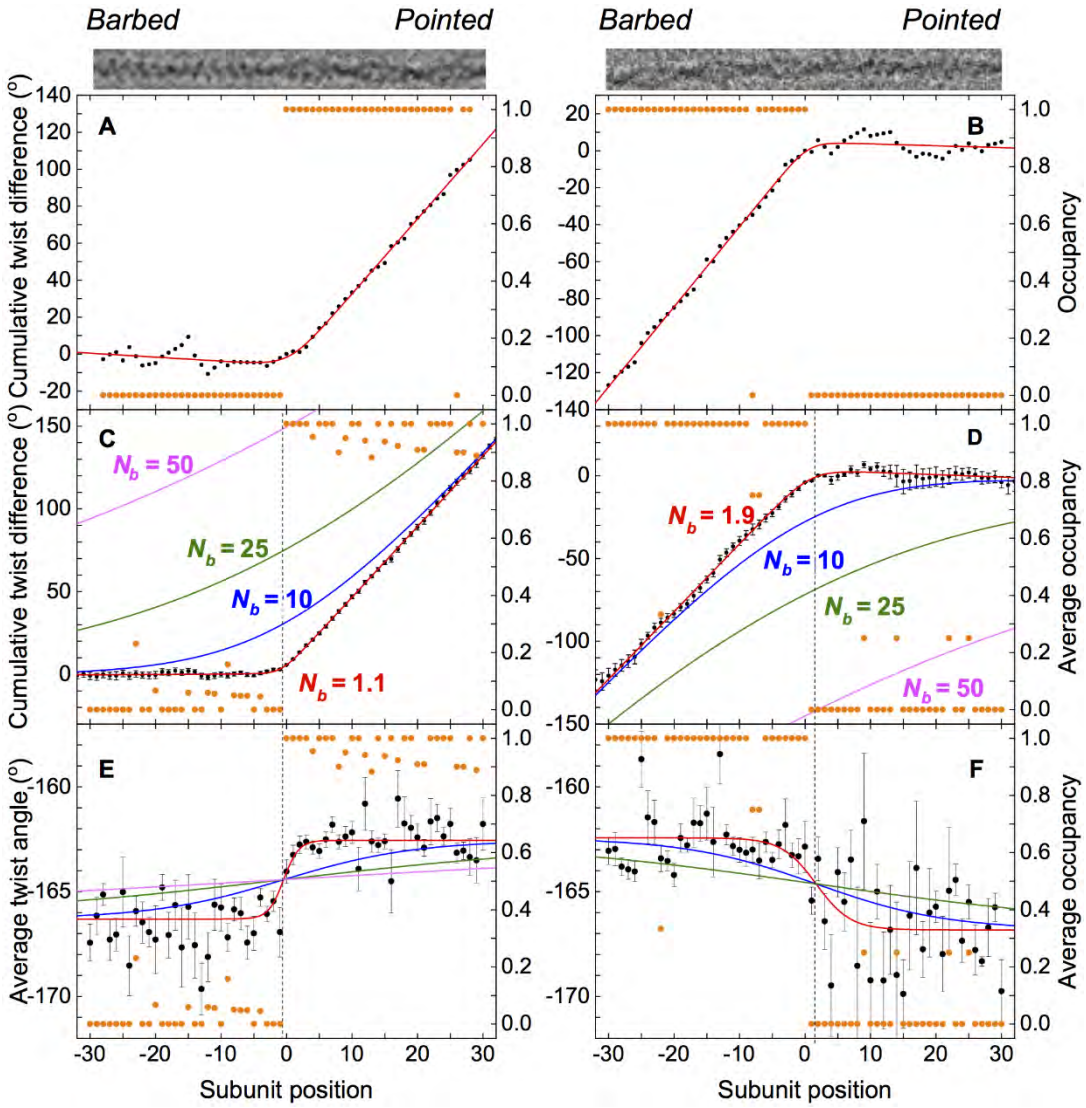

Figure 25. The actin filament twist changes abruptly at boundaries between bare and cofilin-decorated segments. A, For an imaged filament with a boundary (top), the 'net twist difference' (i.e. the excess twist with respect to a canonical bare actin filament, accumulated subunit-by-subunit starting from the left (barbed end)), is plotted together with the single-site cofilin occupancy. An abrupt, 'hockey stick' transition from a measured excess twist value of ~0° per subunit (corresponding to bare actin) to a value of ~4° per subunit (corresponding a cofilin-decorated actin filament) coincides with the cofilin cluster boundary (n = 0). B, Results similar to A for a filament where bare actin was found on the pointed-end side of a cluster and the accumulated 'net twist difference' was calculated starting from the pointed end. C, The quantities in A (cumulative net twist difference and cofilin occupancy) are averaged for 24 filaments where bare actin was found on the barbed-end side of a cofilin cluster. The error bar for the n^{th} estimate of the cumulative net twist difference is about the same as the error of n^{th} ϕ value, and the smooth red curve corresponds to the best fit of the data to an empirical function (integral of a sigmoid function; see Methods), which yielded an estimate for the characteristic decay length of the twist transition, N_b, of 1.3 ± 0.1.

Figure 2. (Continued) Three other smooth curves (blue, green, magenta) depict perturbations of the fitting function where $N_b$was set to larger values that within the range previously reported in the literature. D, Results similar to C for 4 filaments where bare actin was found on the pointed-end side of a cluster. The fitted value for N_b was 1.9 ± 0.3. E. The average axial rotation between subunits n and n – 1 for the population of 24 filaments in C. The smooth red curve represents the best fit of the data to an empirical sigmoid function (see Methods), yielding estimates for N_b (1.3 ± 0.3), the average twist for cofilactin (–162.6°) and the average twist for bare actin (166.3°). This analysis reveals that the transition from the axial rotation corresponding to canonical actin to that of fully decorated cofilactin occurs within 1-2 subunits from the boundary. F, The average axial rotation for the population of 4 filaments in D, and the corresponding fitted sigmoid function (yielding parameter estimates for $N_b(2.6 \pm 1.6)$, the average relative twist for cofilactin (–162.4°), and the average relative twist for actin (–166.8°). Magnitudes of the uncertainty bars are larger than in E due to smaller sample size; nevertheless, the transition in axial rotation value is localized to no more than 1-2 subunits.

High-resolution reconstructions of bare actin and cofilactin filament segments derived from a heterogeneous sample

After the above results were published, I collected a much larger data set (~3000 micrographs) to obtain a sufficient number of particles to perform 3D structure analysis of the boundaries directly. To facilitate filament identification, instead of manual boxing segments I used a recently devised template-matching procedure (51) to automatically detect filament paths and extract contiguous, overlapping box segments centered on consecutive 27.5 Å repeats along the filament (Fig. 3). I repeated the refinement strategy employed earlier to generate a hybrid map, which refined to a nominal resolution of 3.6 Å. Again, the map quality was compromised due to averaging of cofilactin and bare actin segments, and featured weak density for bound cofilin, as expected due to substoichiometric cofilin occupancy.

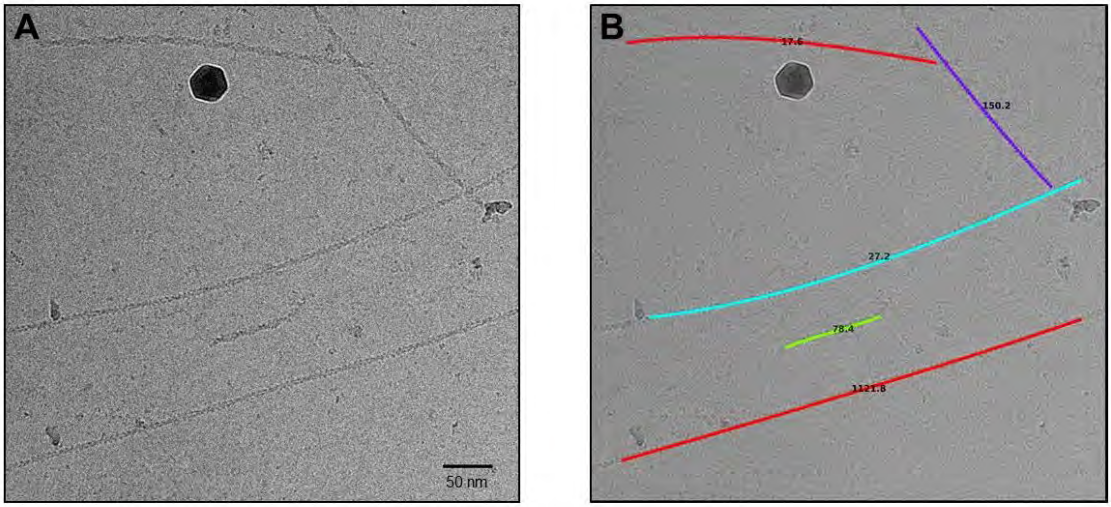

Figure 26. Representative image of decorated and bare actin filament segments. A. Representative motion-corrected micrograph of partially cofilin-decorated actin filaments. B. Filament tracing performed automatically by MicHelixTrace from the SPRING package. Some, but not all, filament intersections were avoided. Colors are for visualization purposes only and the figures note the computed persistence length of the tracings.

I separated actin and cofilactin classes on a single subunit basis following the earlier procedure (34, 44), yielding cofilactin (nominal resolution 4.1 Å) and bare actin (nominal resolution 4.4 Å) structural classes. I improved the resolution of cofilactin to 3.4 Å (Fig. 4) and bare actin to 3.5 Å (Fig. 5) with independent refinement of these two classes. Despite originating from a heterogeneous mixture, these maps are largely indistinguishable from comparable or slightly lower resolution structural models derived from homogeneous samples of bare actin (52) or cofilactin (1, 42). Cofilin bridges longitudinally adjacent filament subunits, changes the filament twist, and tilts the actin outer domain, which displaces and disorders the actin D-loop (Fig. 4). Bare actin filaments retain the untilted conformation and maintains extensive intersubunit D-loop contacts (Fig. 5).

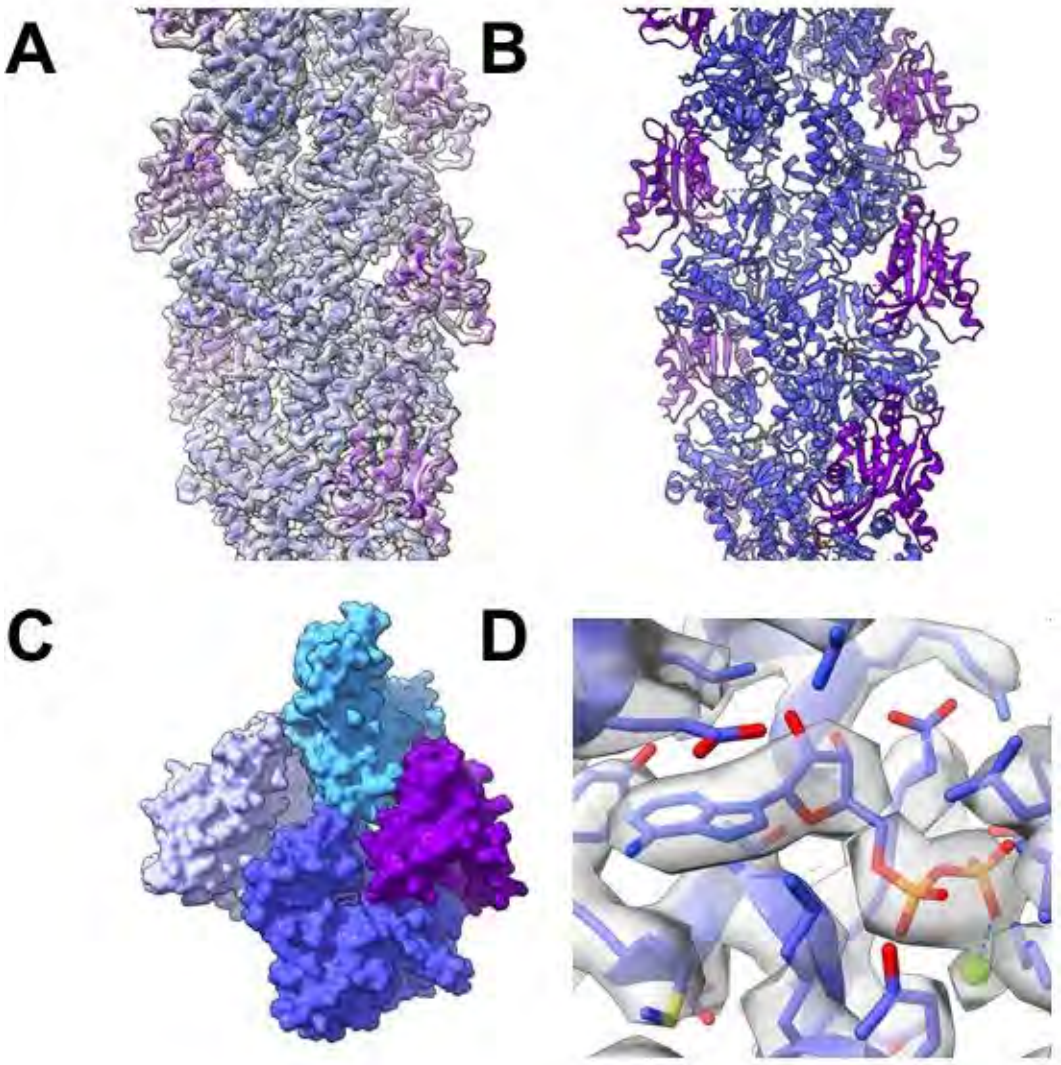

Figure 27. Atomic resolution structure of cofilactin actin from partially cofilin-decorated samples. A. Cryo-EM reconstruction and fitted ADP-cofilactin model (PBD ID: 5YU8, blue: actin, purple: cofilin (42)) of cofilactin class following single subunit classification and independent refinement. B. Model as in A without the cryo-EM density. C. Surface representation of 3 actin filament subunits colored in different shades of blue and a single cofilin subunit in purple. D. Magnified view of Mg.ADP in the cryo-EM density.

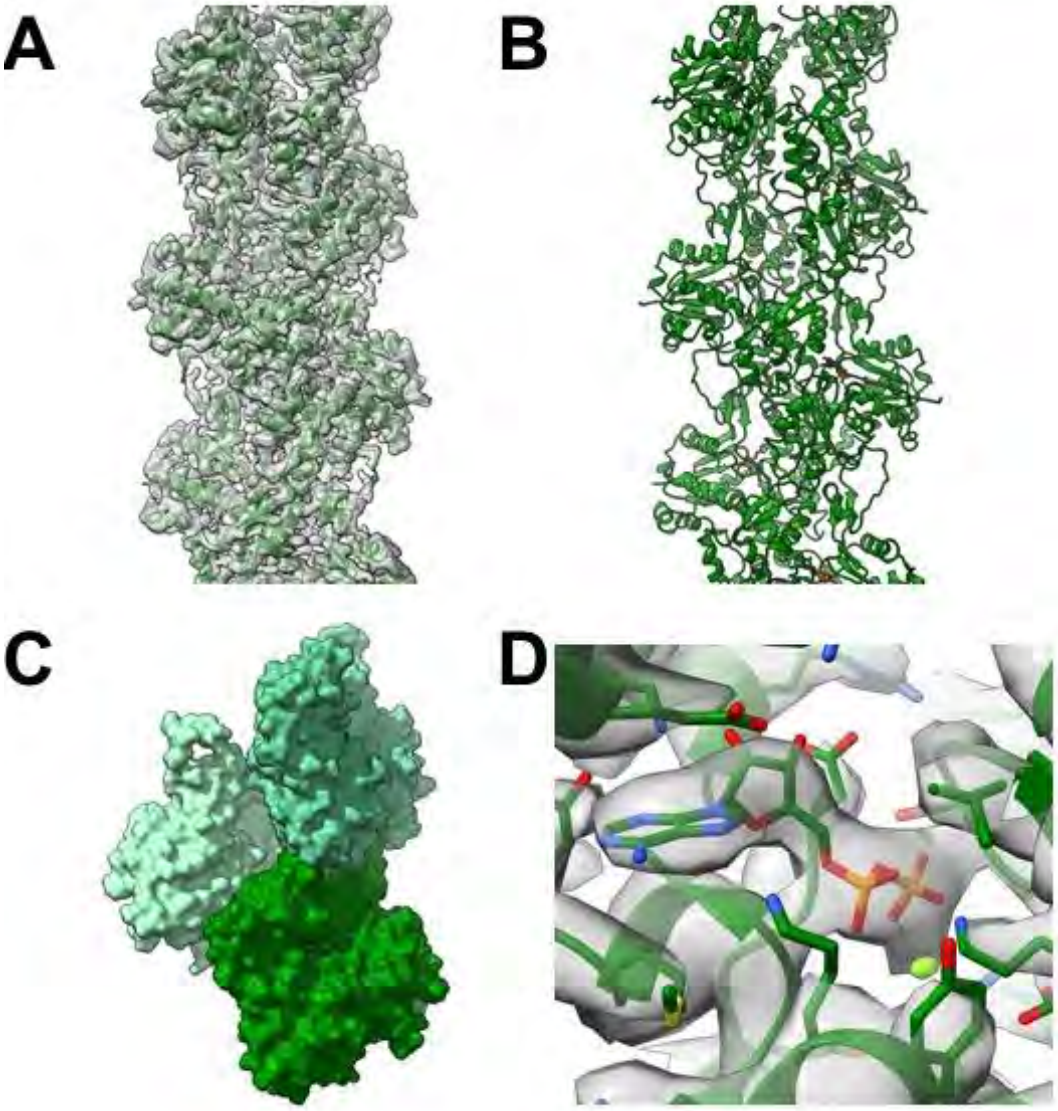

Figure 28. Atomic resolution structure of bare actin from partially cofilin-decorated samples. A. Cryo-EM reconstruction and fitted ADP-actin model (PBD ID: 6DJO, green (52)) of the bare actin class following single subunit classification and independent refinement. B. Model as in A without the cryo-EM density. C. Surface representation of 3 actin filament subunits colored in different shades of green. D. Magnified view of Mg.ADP in the cryo-EM density.

A single cofilin tilts and disorders the D-loop of one actin subunit

This single subunit classification procedure allowed me to determine the structure of an actin filament with single bound cofilin. I reconstructed a 7.8 Å resolution cryo-EM density map from 8,917 particles (Fig. 6A, 10A), revealing a unique configuration of actin in which the single, bound cofilin induces highly local perturbations in the actin filament (Fig. 6C, 10A).

Cofilin compromises the integrity of the filament in this structure by perturbing a longitudinal actin-actin interface without forming a compensating bridging interaction across the same interface (Fig. 6, 10A). As with canonical cofilactin, the individual, bound cofilin bridges two neighboring actin subunits (*i*, *i* - 2) along a single protofilament. However, independent rigid body fitting of the actin inner and outer domains into this map reveals that only the pointed end binding partner (subunit *i*) tilts (Fig. 6C, 10A) – its outer domain tilts in the same direction and by nearly as much (~10° vs 18°) as in cofilactin (Fig. 4). The second subunit in contact with cofilin (subunit *i* - 2) retains an untilted, bare actin conformation, as do all other actin subunits in the reconstruction (Fig. 6C, 10A). Minor discrepancies (~2-3°) between the tilt magnitude of untilted and canonical bare actin subunits (Fig. 6C) likely reflect uncertainties in the rigid body fits of the atomic models into the density map, due to limited resolution.

Actin subunit (*i*) tilting by cofilin disrupts canonical interactions between filament subunits *i* and *i* + 2. (Fig. 6A, 10A). Repositioning and disordering of the subunit *i* D-loop upon tilting detaches it from the adjacent actin in the pointed end direction (subunit *i* + 2) (Fig. 6C, D, 10A). Loss of this longitudinal contact introduces a structural 'defect' in the protofilament that could potentially compromise filament integrity.

A single bound cofilin also disrupts canonical interactions between subunits *i* and *i* - 2, but this perturbation is compensated by cofilin 'bridging' of these two subunits (Fig. 6, 10A). These

cofilin bridging interactions are distinct from those in large cofilin clusters (*i.e.* saturated cofilactin, Fig. 10) due to the untilted conformation of subunit *i* - 2. The untilted subunit *i* - 2 forms a previously unidentified contact with the cofilin with its D-loop (Fig. 6D, 10A). Subunit bridging by a single cofilin, while distinct from that observed in large cofilin clusters, should stabilize the subunit *i* and *i* - 2 interface.

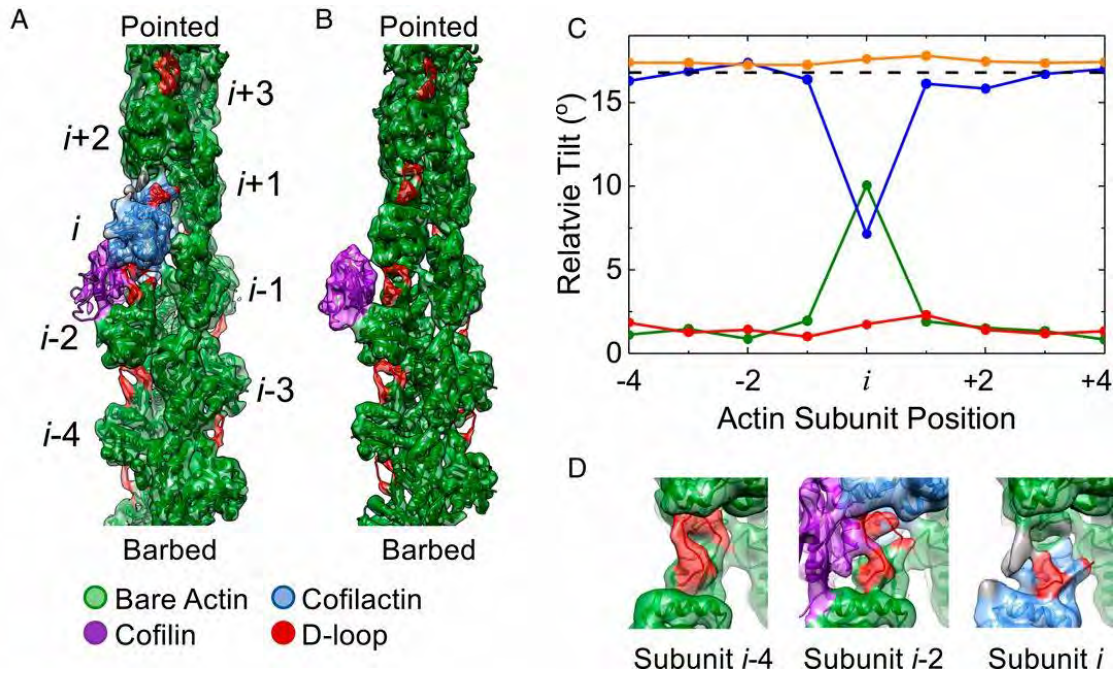

Figure 29. A single, bound WT cofilin disrupts intersubunit contacts between the actin subunit to which it is bound (subunit *i*) and its nearest, longitudinal neighbor (subunit *i* - 2). A. Cryo-EM density map reconstructed from filament segments (n = 8,917) containing ≥ 5 bare sites, followed by 1 cofilin-occupied site, followed by ≥ 4 bare sites progressing from the barbed to the pointed end of the filament. PDB models of actin and cofilactin were fit into the cryo-EM density. The cofilactin models are colored blue (PDB ID 5YU8), bare actin is colored green (PDB ID 6DJO), and cofilin is colored purple (PDB ID 5YU8). The actin D-loop is colored red. B. Cryo-EM reconstruction of 24,000 isolated, bound S3D-cofilin molecules identified by 3D classification on 5 actin subunit-long segments, colored as in A. C. Fitted outer domains into the WT and S3D-cofilin maps were compared with reference cofilactin (WT: blue, S3D: orange) or bare actin (WT: green, S3D: red) models that were aligned to the actin inner domain region of the map. The rotation angle between the outer domains of the reference models is also shown (dashed black line). Only the actin subunit bound to WT cofilin towards the pointed end of the filament (subunit *i*) adopts a cofilactin-like conformation, all other subunits adopt bare actin. D. Close-up view of the D-loops from actin subunits *i*, *i* - 2, and *i* - 4 from the single, bound WT cofilin fragment from identical orientations. Cofilin disrupts the D-loop cryo-EM density of the 2 actin subunits adjacent to it (subunits *i* and *i* - 2), while the D-loop cryo-EM density of all other D-loops remains properly positioned and relatively strong. Some unaccounted additional density (grey) appears near the D-loop of subunit *i*, which may originate from conformational mixing with an alternative structural state where cofilin is incompletely bound and/or fails to tilt subunit *i*.

A single S3D-cofilin adopts a unique binding mode that does not alter the actin conformation

The phosphomimetic S3D-cofilin mutant binds and severs actin filaments more weakly than WT cofilin (19), but the fully decorated S3D-cofilin:actin complex is indistinguishable from WT cofilactin at ~8 Å resolution (*i.e.* actin is in the tilted conformation) (19), leaving the mechanism behind weak binding and severing unclear. To investigate further, we reanalyzed a published data set (19) of actin filaments partially decorated with S3D-cofilin (referred to as S3D-cofilactin) using a modified classification scheme (see Methods) and identified 23,918 particles of isolated S3D-cofilactin subunits. This was a sufficient number of particles to reconstruct a map of single, bound S3D-cofilin (Fig. 6B).

The resulting structure reveals that, in contrast to WT cofilin, a single, isolated S3D-cofilin fails to detectably perturb the filament; all subunits maintain the bare actin conformation (Fig. 6C, 10B). Moreover, S3D-cofilin primarily contacts subunit *i* - 2 and forms no detectable contacts with subunit *i* (Fig. 6B, 10B). The S3D-cofilin contacts with actin subunit *i* - 2 resemble those observed with fully decorated cofilactin. However, since subunit *i* - 2 remains in the untilted bare actin conformation, bound S3D-cofilin tilts away from subunit *i* and the filament long axis (Fig. 6B, 4A). In this arrangement, the S3D-cofilin N-terminus resides > 10 Å from its binding site on subunit *i* (Fig. 6B), consistent with the cofilin N-terminus undocking from actin subunit *i* (19). Thus, a single S3D-cofilin forms fewer contacts with actin and does not visibly affect the filament structure, consistent with its reported weak binding and negligible severing activity (19).

Classification and 3D reconstruction of boundaries between bare and cofilactin filament segments

We identified barbed and pointed end boundaries by searching the single-subunit occupancy data for cofilin clusters (n ≥ 5) adjacent to a bare actin segment (n ≥ 5). Here, we

define boundaries according to contacts made with bound cofilin: actin subunits in direct contact with cofilin are considered part of a cofilactin segment and all other actin subunits are considered part of a bare actin segment. This procedure identified 671 WT cofilin barbed end boundaries (bare actin at the cluster barbed end) and 146 WT cofilin pointed end boundaries (bare actin at the cluster pointed end) within the 1,117,338 particles defining the data set. The resolution achieved by these reconstructions (9.5 Å and 24 Å for the barbed and pointed end boundaries, resp.) permitted analysis of conformational changes at the barbed end boundary.

Attempts to identify S3D cofilin barbed and pointed end boundaries were unsuccessful. The binary classification scheme utilized for wild-type cofilactin did not yield a decorated class, which we attribute to higher background noise in the S3D images due to a large excess of unbound cofilin. In addition, the higher cooperativity of S3D-cofilin compared to WT cofilin introduces fewer boundaries (19), which presumably reduced the observed boundary population. I devised an alternate classification scheme to detect isolated, bound S3D cofilin molecules (see Methods) by including multiple adjacent cofilin sites within the focused mask region. This scheme also failed to detect boundaries involving multiple bound cofilins, but does not rule out their presence in the S3D sample.

Longitudinal D-loop contacts persist at the barbed end side of cofilin clusters, despite an abrupt transition in actin conformation

Analysis of a 3D reconstruction of the barbed end boundary indicates that the inherent twist of cofilactin persists to the actin subunits cofilin directly contacts and not further (Fig. 7). That is, neither does the cofilactin twist propagate from the boundary into bare actin segments, nor do these bare actin segments alter the intrinsic twist of the adjoining cofilactin segment. This result confirms and refines our previous conclusion, derived from alignment parameters from 2D

image processing, that the filament twist changes abruptly (within 1-2 subunits) at barbed end boundaries (44). The current results make it clear that a cofilin cluster includes all actin subunits in direct contact with cofilin (including subunits *i* - 1 and *i* - 2, Fig. 4C), and that there is no twist propagation beyond this boundary.

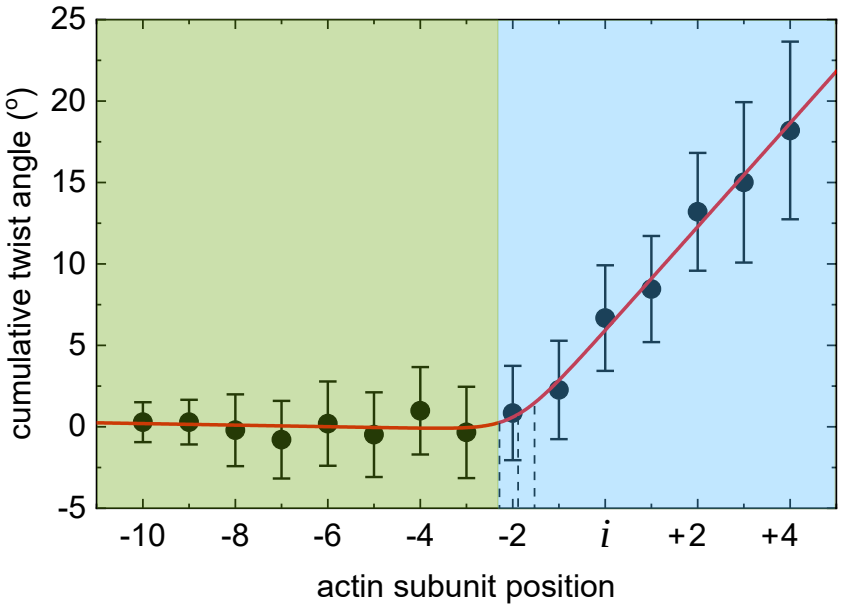

Figure 30. The actin filament twist changes abruptly at the barbed end side of cofilactin clusters. The first cofilin in the cluster binds between actin *i* - 2 and *i*. The light green shaded region represents actin subunits not in contact with cofilin and subunits within the light blue shaded region directly contact cofilin. The twist rotation between 2 adjacent subunits, plotted as the cumulative twist difference (25), indicates that cofilactin filament twist transition occurs near first subunit in direct contact with cofilin (subunit *i* – 2). The best fit of the data to an integrated form of the Boltzman equation (25) is indicated by a red line and yields a transition center at subunit *i* – 1.92 and transition width of ± 0.4 actin subunit (indicated by three vertical dashed lines). The uncertainty bars represent the standard deviation of 4 measurements from separate reconstructed maps centered on adjacent subunits in the filament segment. The data was scaled to bare actin with zero cumulative twist as the reference.

Measurements of subunit tilt at the barbed end boundary revealed an abrupt transition in actin conformation that coincides with the terminal cofilin-bound actin subunits (Fig. 8C, 10C). However, in contrast to single, bound WT cofilin, which only converts its pointed end binding partner to the tilted conformation (Fig. 6C, 10A), both actin subunits in contact with the terminal cofilin molecule of a cluster adopt the tilted conformation at barbed end boundaries (Fig. 8C, 10C). As a consequence, the abrupt tilt transition in the actin filament at the barbed end boundary is displaced from the cofilin-bound region where it is not bridged by bound cofilin (Fig. 8, 10C). This lack of a bridge, combined with an abrupt tilt transition, introduces a potential weakness in the filament lattice at the (*i* - 1, *i* - 2)-(*i* - 3, *i* - 4) interface.

Cluster barbed end boundaries retain an ordered D-loop that forms substantial longitudinal intersubunit contacts (Fig. 8, 10C), but these appear strained when compared to those of canonical (bare) actin due to the abrupt tilt transition (Fig. 8; Fig. 10C, gold dashed line). This contrasts with the cluster pointed end observed in isolated, bound WT cofilin, where D-loop contacts are completely broken (Fig. 6; Fig. 10A, red dashed line). This observed reduction in longitudinal contacts at pointed end boundaries compared with barbed end boundaries in our structures is consistent with pointed end boundaries severing more readily than those at the barbed end side of cofilin clusters (24, 25, 41). The greater disruption at the pointed end side of a cluster may also facilitate cofilin binding, thereby contributing to preferential growth on this side of a cluster (11).

A similarly detailed analysis was not feasible for the pointed end boundary due to the lower resolution observed for this reconstruction. However, features of this boundary can be inferred from the single bound cofilin reconstruction (see Discussion).

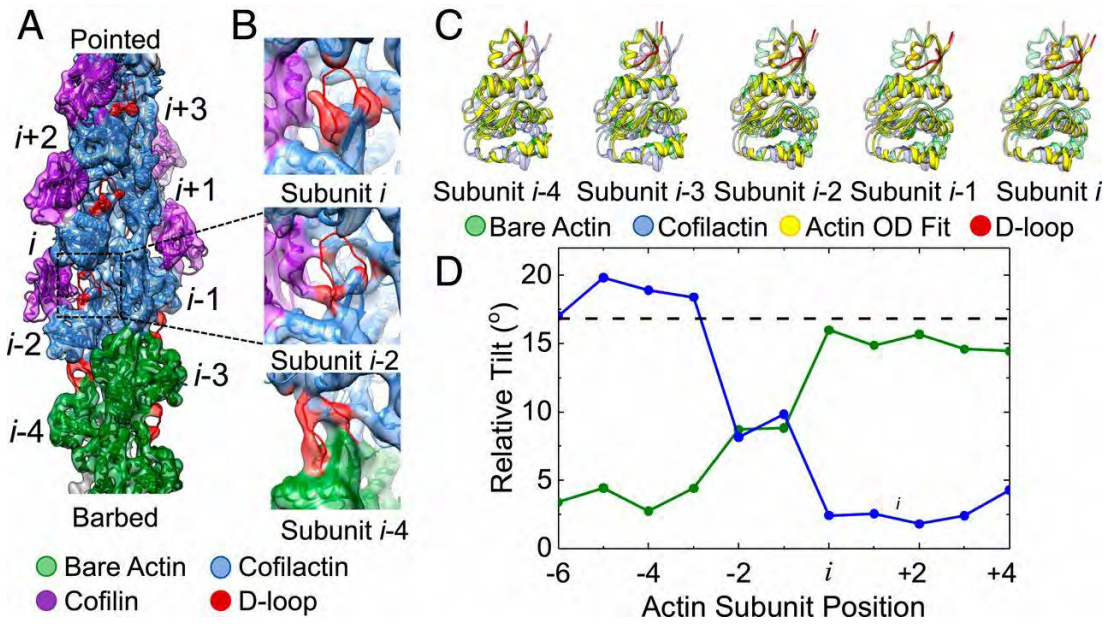

Figure 31. Actin conformation changes abruptly at the barbed end-boundary of large cofilin clusters. A. Cryo-EM density map reconstructed from filament segments (n = 671) containing ≥ 5 bare sites followed by ≥ 5 cofilin-occupied sites progressing from the barbed to the pointed end of the filament. PDB models of actin and cofilactin were fit into the cryo-EM density. The cofilactin models are colored blue (PDB ID 5YU8), bare actin is colored green (PDB ID 6DJO), and cofilin is colored purple (PDB ID 5YU8). The actin D-loop is colored red. B. Close-up view of the D-loops from actin subunits *i*, *i* - 2, and *i* - 4 along the segment shown from identical orientations. The D-loop cryo-EM density indicates a loss of order for all subunits directly in contact with cofilin. C. The orientation of the outer domain of an actin subunit (solid yellow) changes abruptly from the cofilactin (transparent blue) to the bare actin conformation (transparent green) at the boundary. Fitted outer domains were compared with reference cofilactin (transparent blue) or bare actin (transparent green) models that were fitted into the actin inner domain region of the map. The visible portions of the D-loop are colored red. D. The rotation angle between the fitted and reference bare actin (green) and cofilactin (blue) outer domains shown in C. The rotation angle between the outer domains of the reference models is also shown (dashed black line).

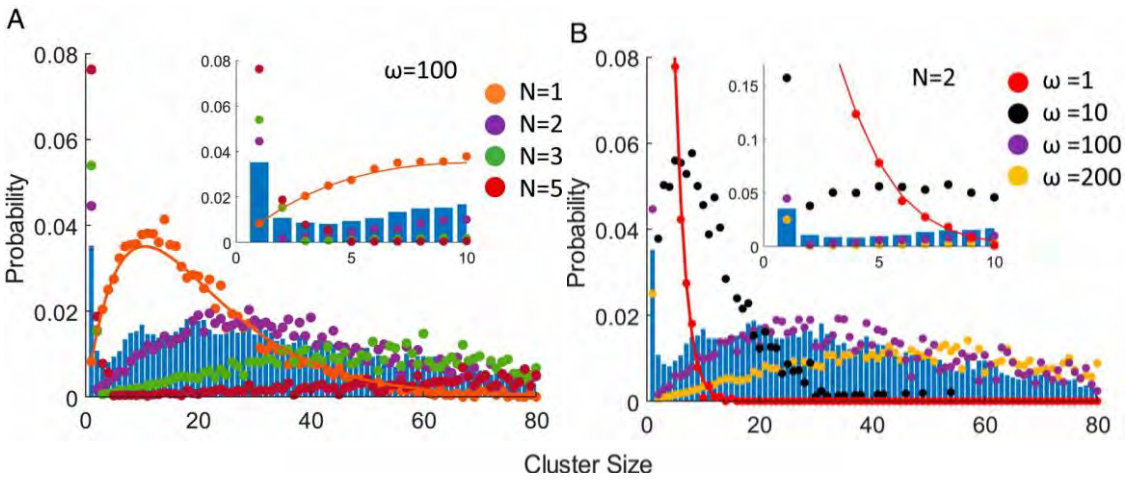

Figure 32. Probability of a bound (WT) cofilin being in a cluster of given size (*C*). A) The size distribution of clusters formed from contiguously bound cofilin molecules observed in cryo-EM specimens (blue histogram) compared with distributions predicted by Monte Carlo simulations for nucleus sizes (*N*) of 1 (orange), 2 (purple), 3 (green), or 5 (red) with a cooperativity (ω) of 100 and a binding density (v) of 0.5. The orange line through the simulated data for $N = 1$ represents the analytical solution for a nucleus size (*N*) of 1. Analytical solutions for higher nucleus sizes are not available. Inset shows a magnified view of the same plot for cluster sizes (*C*) 0-10. B) Cluster size distribution observed in cryo-EM specimens (blue histogram) compared with distributions predicted by Monte Carlo simulations for cooperativity (ω) of 1 (red), 10 (black), 100 (purple) or 200 (yellow) with a critical cluster size (*N*) of 2. Inset displays a magnified view of the same plot for cluster sizes (C) 0-10.

The probability distribution of bound cofilin suggests two contiguously bound cofilins 'nucleate' cooperative cluster growth

The single-subunit cofilin occupancy data developed here permits analysis of the cofilin cluster size (*C*) distribution (Fig. 9). A significant population of single bound cofilin is readily observed at a cofilin binding density (v) of 0.5 (Fig. 9), from which I determined the structure of an isolated, bound cofilin (Fig. 6). In contrast, substantially fewer cofilin clusters of $C > 1$ were identified in these samples (Fig. 9).

Equipped with this experimental distribution profile of bound cofilin, Jeffrey Bibeaux from the De La Cruz laboratory performed equilibrium binding simulations to investigate the critical

cofilin binding parameters. He found that the observed distribution places strong constraints on the value of the critical cluster size needed for full cooperative binding interactions (*i.e.* "nucleus" size required to activate cooperative interactions, *N*). At a given cofilin binding density, two binding parameters significantly influence the distribution profile at equilibrium (or steady-state): the degree of cooperativity (given by the cooperativity parameter ω) and the nucleus size (*N*) required for cooperative interactions. The observation of small clusters ($C < N$) places constraints on the possible nucleus size (*N*), and the distribution profile of large clusters ($C > N$) places constraints on the degree of cooperativity (ω). Because we are analyzing an equilibrium distribution of bound cofilin, the cluster size distribution is independent of the binding kinetics.

At a cofilin binding density of 0.5, values of $\omega = 100$ and nucleus size $N = 2$ predict bound cofilin distributions that qualitatively match my experimentally observed distribution (Fig. 9), displaying a prominent population at $C = 1$, followed by a sharp reduction in frequency of $C = 2,3,4\ldots$, before gradually increasing to a maximum at $C \approx 20$, followed by a subsequent reduction (Fig. 9). A nucleus size (*N*) of 1 predicts relatively few singly bound cofilin (Fig. 3A), independent of the cooperativity, and a nucleus size of $N = 9$ predicts a distribution that does not coincide with that observed in our data set. Thus, a nucleus size (*N*) of 2 best accounts for the experimentally observed cofilin cluster size distribution (Fig. 9), suggesting that 2 contiguously bound cofilin molecules serve as the nucleus for cooperative cofilin binding. Furthermore, lower or higher cooperativity values (ω) also predict distributions that do not coincide at all with the observed distribution (data for a nucleus size (*N*) of 2 shown in Fig. 9B). Thus, $N = 2$ and $\omega = 100$ is consistent with the probability distribution of a bound cofilin being in a cluster of a given size.

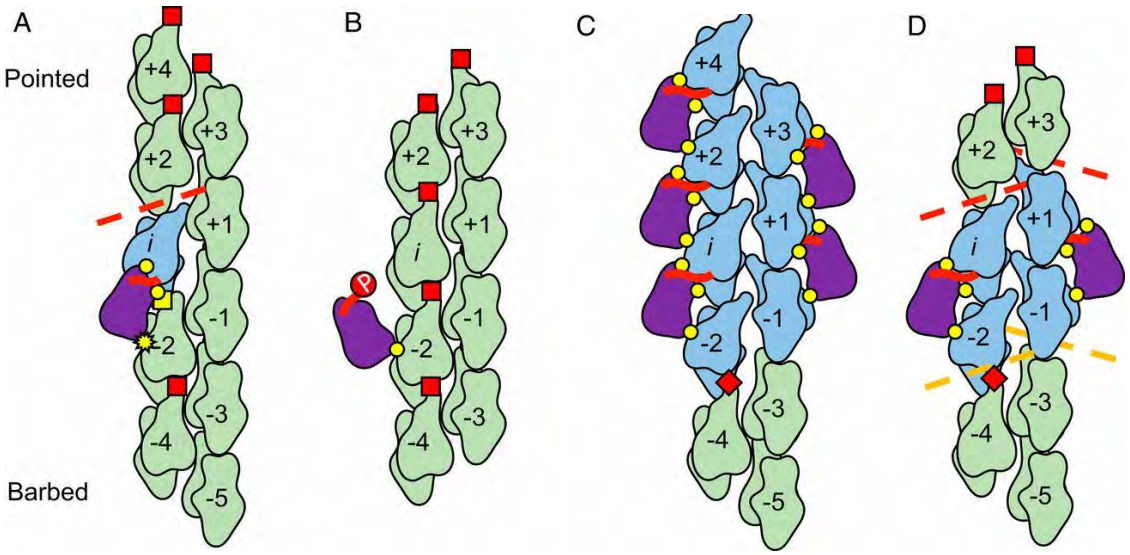

Figure 33. Cooperative cofilin binding model on actin filaments. A. Rotation of the outer domain of actin (subunit *i*; blue) breaks the D-loop contacts (dashed red line) with the longitudinal neighbor (subunit *i* + 2) and allows the N-terminus of isolated, bound wild type cofilin (thick red line) to make significant contacts with the filament (i.e. "docking"). The barbed end of the neighboring actin (subunit *i* - 2) does not tilt, but its D-loop is blocked from forming native intersubunit contacts by bound cofilin, with which it forms a novel interaction (yellow square). Intact D-loop interactions with adjacent neighbors are represented by red squares and canonical cofilin-actin contacts are represented by yellow circles. The yellow star represents a cofilin:actin contact perturbed by a lack of tilting in subunit *i* - 2. B. Phosphorylation (red circle labeled 'P') of the cofilin N-terminus prevents its interaction with the actin outer domain, significantly weakening the binding interaction and disfavoring rotation of the outer domain. C. At a cluster barbed end, outer domain rotation by the terminal cofilins deforms (dashed orange lines) but fails to break native D-loop contacts with adjacent neighbors in the bare region (red diamonds). D. In a cluster, illustrated as the minimal cluster (*i.e.* nucleus) that occupies both protofilaments, all actin subunits directly contacting cofilin adopt the tilted conformation. A-D. I emphasize for the general reader that the filament is illustrated as an untwisted helix to better visualize all of the intersubunit interfaces, some of which would be out of the plane of view if the filament was illustrated with a realistic helical twist.

Discussion

Method for directly correlating regulatory protein occupancy with filament geometry

Here I presented a structure-based method for classifying individual filament subunits with distinct structural states while maintaining their spatial relationships, including subunits positioned across topological boundaries. This method is general and readily applicable to other classes of linear, helical polymers. Previous cryo-EM methods have not resolved filament occupancy at the level of individual subunits because classification was performed on particles that included multiple subunits and binding sites. Such approaches obscure the precise location of the boundary.

Allosteric effects of cofilin on actin filament twist

I demonstrated that actin filaments partially-decorated with cofilin display an abrupt and marked change in twist at boundaries between bare and cofilactin segments (Fig 2). A recent AFM study (11) reported that cofilactin-like twist propagates >10 subunits into bare actin segments from the pointed end side of cofilin clusters. I observe no detectable long-range propagation of the cofilactin-like twist into the bare actin segment, or vice versa (i.e. into the cofilin cluster), nor do I detect a significant bias towards the filament barbed or pointed ends (Fig 2). I have no explanation for the differences observed with the different methods. A potential explanation for this discrepancy is filament tethering to a surface (e.g. membrane or glass, either directly or through a binding protein), which has been shown to affect filament structural dynamics and cofilin severing activity (53), differences in actin and/or cofilin isoforms (9, 10) in some cases, and/or modification of protein components with fluorescent probes (9).

Limitations in boundary zone characterization

The structural discontinuity at the boundary is likely sharper than estimated by our twist analysis. Particle parameters used to calculate net twist values were derived by aligning particles

within masks that include up to 9 subunits, so that the estimated position and orientation of a given subunit is influenced by neighbors up to 4 subunits away. In addition, the smoothing algorithm implemented here (local fitting using a 7-subunit window centered on the subunit of interest using the method of least-trimmed squares; see Methods) introduces further correlations between the estimated position and orientation of given subunit relative to that of its neighbors, although this effect may be partially mitigated due to our discarding (or 'trimming') two outliers from each fitting window. Both of these effects could smooth the structural transition at the boundary relative to its true geometry. Nonetheless, the geometric transitions reported here abruptly change at the boundary, indicating that cofilin-induced cooperative conformational changes in actin are local and limited to nearest-neighbor interactions. We reiterate that these conclusions are derived from analysis of cofilin cluster sizes $N > 20$ in length. Accordingly, we cannot eliminate the possibility that conformational changes in the filament propagate farther from small clusters ($N < 20$) than larger clusters.

Origins of cooperative binding interactions

My results and analyses indicate that cofilin-linked changes in actin filament twist are local (*i.e.* not long-range). If one assumes that cooperative cofilin binding originates from allosteric changes in filament twist, as might be expected since cofilin changes the filament twist, this observation explains why a nearest neighbor cooperativity model accounts for both equilibrium (9, 12, 21, 39) and transient kinetic (12, 14) binding data. It is possible that long-range, sub-stoichiometric effects observed by calorimetry (13, 20), phosphorescence anisotropy (15), AFM (11) or super-resolution fluorescence microscopy (18) originate from factors other than changes in filament twist.

Asymmetries in boundary polarity

Due to the polarity of actin, two types of cluster boundaries exist: those with bare actin positioned at the pointed-end side of the cluster, and those with the bare actin positioned at the cluster barbed end. While quantifying the boundary types by cryo-EM has its limitations and assumptions, my sampling methods identified significantly more boundaries with bare actin positioned at the barbed-end side of the cluster. Several phenomena could give rise to this observation. For example, barbed-end boundaries may be more readily identified than pointed-end ones. Alternatively, this behavior could arise if severing occurred preferentially at the pointed-end side of the cluster, as reported (24, 25). A third possible explanation would be a mechanism in which cofilin clusters grew asymmetrically and more rapidly in the pointed-end direction, such that clusters extended to the filament pointed end.

Conformational changes in actin are limited to subunits in direct contact with cofilin

The sub-nanometer boundary reconstructions presented here also demonstrate that only actin subunits in direct contact with cofilin undergo substantial conformational changes; actin subunits not directly contacting cofilin retain the bare actin conformation (Fig. 10). Thus, the geometry of cofilin cluster boundaries is determined by local, nearest neighbor interactions, rather than long-range, non-nearest neighbor effects extending from the boundary. This presumably explains why nearest neighbor models of cooperative cofilin binding can account for much of the equilibrium and kinetic data reported in the literature, including the correlation of boundary density with severing activity ((17) and references therein).

The lower resolution of the pointed end boundary reconstruction leaves open the possibility that conformational changes could propagate further into the bare actin segment than in the case of isolated, bound cofilin. However, it appears unlikely that conformational changes would propagate multiple ($n > 3$) subunits away from the boundary in the absence of direct cofilin-

binding interactions, given the abrupt twist transition observed at pointed end cluster boundaries (44) and recent MD results (54) that indicate the tilted conformation of actin is inherently unstable. Therefore, we conclude that the pointed end boundary of cofilin clusters resemble the pointed end protofilament boundary of an isolated, bound cofilin, in that stable cooperative conformational changes do not persist beyond subunits in direct contact with cofilin.

Maximal cooperative cofilin binding requires a nucleus of 2 adjacent, contiguously-bound cofilins

Analysis of the cluster size (*C*) distribution in my data set strongly favors a model in which the critical cluster size, or nucleus (*N*), for cooperative cofilin binding interactions is 2 contiguously bound cofilins (Fig. 9). While in principle these cofilins could be laterally or longitudinally adjacent, our simulations are based on a linear, one-dimensional filament lattice model and do not consider two longitudinally adjacent cofilins (i - $i \pm 2$) to be contiguously bound. The reduced population of both laterally and longitudinally adjacent bound cofilin pairs in my observed cluster size distribution raises the possibility that both clusters could serve as nuclei for cooperative cluster growth.

A cluster of $C = 2$ could achieve full cooperativity if its boundaries closely resembled those of large clusters, where the two cofilins at the barbed end side of the cluster tilt the adjacent, unoccupied actin subunits on each protofilament (Fig. 8, 10C). This scenario could be readily achieved with a laterally adjacent dimer (Fig. 10D). However, similar cooperativity may be achieved via other configurations of $C = 2$ clusters, if for example, tilting of multiple subunits in one protofilament leads to compensatory tilting in the other protofilament (42). A common feature of these nuclei would be conversion (*e.g.* tilting) of (at least) 4 contiguous actin subunits in the filament.

A single, bound WT cofilin tilts one of the two actin subunits it directly contacts (Fig. 6, 10A). This tilting displaces SD2 from the neighboring longitudinal subunit (*i* + 2) at its pointed end side, which is expected to facilitate cofilin binding at this neighboring site (12, 14, 52). Thus, a single, bound cofilin molecule could potentially exert cooperative binding effects with its longitudinal neighbors. We anticipate that the degree of cooperativity is less than that of two adjacent cofilins, given that the observed cofilin cluster size (*C*) distribution (Fig. 9) features a substantial population of isolated, bound cofilin (this population would be diminished if isolated, bound cofilins functioned as nuclei).

These results do not explain the different cooperativity of the S3D mutant compared to wild-type cofilin (19, 55). Although isolated, singly bound S3D-cofilin has no detectable effect on the filament structure (Fig. 6B), clusters of contiguously bound S3D-cofilin together do tilt filament subunits (19), which presumably arises from the additional binding energy associated with binding of multiple S3D-cofilins.

Implications for filament severing

Filament fragmentation occurs preferentially at boundaries between bare and cofilin-decorated segments (8, 9, 11, 21, 22), but the structural origins of this behavior have not been established. My results suggest that subunits directly adjacent to the boundary adopt conformations distinct from those within bare and cofilin-decorated segments. The lack of complementarity with neighboring subunits could potentially render these subunit interfaces more susceptible to fragmentation (e.g. phase boundary problem; (8, 40, 56)), thereby accounting for the observed preferential severing at and near boundaries. Alternatively or in addition (since multiple severing pathways may exist), severing could occur in the adjacent, bare segment that adopts a cofilactin-like twist but without the stabilizing cofilin-actin interactions

(1). However, my data indicate that the region susceptible to severing via this pathway would be limited to the nearest neighbors immediately adjacent to the boundary.

Asymmetry between the pointed and barbed end boundary structures presented here offer a structural explanation to how severing activity can be biased towards the pointed end side of bound cofilin clusters. Tilted cofilactin subunits have compromised longitudinal interactions with neighboring, untilted actin subunits (Fig. 10). These compromised interactions can be viewed as structural defects in the filament lattice. The more dramatic loss of these interactions on the pointed end side of bound cofilin clusters, compared to the barbed end side (Fig. 10) would render these filament subunit interfaces more susceptible to fragmentation by external loads (56-59) or thermally-driven (21, 22, 24) fluctuations in filament shape.

These results indicate that isolated WT cofilin disrupts the filament lattice, suggesting that it has a capacity to promote severing. The substantial loss of subunit *i* D-loop density and contacts compromises longitudinal intersubunit contacts with subunit *i* + 2 (Fig. 6, 10A). However, as this disruption only occurs on one protofilament, the severing activity is likely significantly weaker than at cluster boundaries, where both protofilaments are compromised. This observation is consistent with a single, bound WT cofilin having severing activity (9, 10, 19), but is at variance with studies concluding that clusters of bound cofilin must reach a critical size to sever filaments (24, 25). The discrepancy between my conclusions, derived from an equilibrium analysis, and these other studies may result from severing being in a kinetic competition with cluster growth in the latter cases, such that small cofilin clusters grew more rapidly than filaments severed. It is also possible that larger clusters ($C > 3$) sever filaments more readily than smaller clusters, though we consider this unlikely, for reasons stated above.

The cofilin N-terminus plays a critical role in actin binding and severing

The structures presented here suggest that direct contact with the N-terminus of cofilin is strongly linked to actin subunit tilting and thus presumably to the changes in filament mechanical properties (15, 16, 21, 60-62) associated with conversion to the cofilactin-like conformation. The N-terminus of single, bound WT cofilin is positioned to interact with the pointed end binding partner of cofilin (subunit *i*), which adopts the tilted conformation (Fig. 6, 10A); in contrast, the barbed end binding partner (subunit *i* - 2), which does not interact with the cofilin N-terminus, retains an untilted conformation. These observations are accounted for by steric occlusion of cofilin by actin SD1 in the untilted conformation (1); tilting allows cofilin to bind and its N-terminus to insert.

Chemically modifying the cofilin N-terminus to mimic phospho-cofilin (S3D-cofilin) displaces the N-terminus of an isolated, bound cofilin from the actin filament, allowing the actin subunits to which it is bound to retain their native actin conformation (Fig. 6, 10B). This binding mode accounts for the weak binding and severing activity of single, isolated S3D-cofilin compared to WT cofilin (19). However, this unique binding mode is not observed in clusters of S3D-cofilin, which appear indistinguishable from clusters of WT cofilin at ~8Å resolution despite distinct mechanical properties and severing activities (19). The structures presented here do not address the origins of this behavior.

Partial tilting is observed in the barbed end binding partners of the terminal cofilin molecules in a barbed end boundary (subunits *i* - 1, *i* - 2, Fig. 8, 10C), which are positioned distal from the cofilin N-terminus where they cannot interact. Thus, actin subunit tilting is necessary for cofilin N-terminus insertion, but subunits can partially tilt without cofilin N-terminal insertion. This observation is consistent with cofilin trapping a partially tilted thermal conformer of actin (12, 14), with N-terminal insertion leading to the fully tilted conformation. Collectively

these observations suggest that cooperative cofilin incorporation into a growing cluster is mediated by partial tilting of subunits immediately adjacent to the boundary (*i.e.* nearest neighbors).

Methods

Protein purification and modification

Samples were prepared by Wenxiang Cao from the De La Cruz laboratory. Rabbit skeletal muscle actin and recombinant human non-muscle cofilin-1 proteins were purified as described (19). Actin was labeled with pyrene (*N*-(1-pyrene)Iodoacetamide, ThermoFisher Scientific, cat. #: P29) as described (9). Immediately before polymerization, Ca-actin monomers were converted to Mg-actin with addition of EGTA and $MgCl_2$ and equilibrated on ice for 5 min. (63). Actin was polymerized by addition of 0.1 volume of 10x KMI6.6 buffer (500 mM KCl, 20mM $MgCl_2$, 200mM imidazole), yielding final solution conditions of 0.2 mM ATP, 50 mM KCl, 2 mM $MgCl_2$, 2 mM DTT, 1 mM NaN_3, 20 mM imidazole (pH 6.6), and equilibrated at room temperature for one hour. Cofilin binding to pyrene actin filaments was measured by fluorescence (9, 12, 19). Samples with a cofilin binding density (*v*) of ~0.5 cofilin per actin were used for cryo-EM sample preparation.

Sample freezing and cryo-EM data collection

Cofilin-decorated actin at a binding density (*v*) of ~0.5 was applied without dilution to holey carbon grids (C-flat™ CF-1.2/1.3-4C; Protochips, Inc, Morrisville, North Carolina, USA). No glow discharge was applied to grids prior to sample application. Grids were subsequently blotted and plunge-frozen in liquid ethane using a home-built cryo-fixation device. Movie frames of samples with pyrene-labeled actin were collected on a F20 electron microscope at a nominal defocus of 3-4 µm using a K2 camera in electron-counting mode (~1.3 electrons/pixel/sec, nominal pixel size: 1.247Å, ~4K x 4K pixels); samples with unlabeled actin were collected on a Titan Krios microscope at a nominal defocus of 2-3 µm, using a K2 camera in super-resolution mode (~1.3 electrons/physical pixel/sec; nominal pixel size: 0.666Å, ~8K x 8K virtual pixels). Movie frames

were aligned with Motioncor2 software (64), which was also used to bin the Krios frames by two (final pixel size: 1.333Å, ~4K x 4K pixels).

Initial Helical Reconstruction

Filaments partially decorated with cofilin were manually selected using the boxer program from the EMAN software package (65), and the resulting boxed segments (approximately one per 27 Å repeat) were processed further using RELION. Following an initial round of refinement with a partial (composite) dataset, a tight filament mask was generated using the *relion_mask_create* tool (corresponding to a length of approximately 9 actin subunits), and 26 rounds of refinement were performed with the entire (composite) dataset, followed by 3 additional rounds of refinement with a truncated filament mask (length of approximately n = 5 subunits). Reconstructed volumes were not symmetrized between successive refinement rounds.

High Resolution Helical Reconstruction

After collecting a larger data set, filaments partially decorated with cofilin were selected with *Michelixtrace*, an automated template-matching procedure from the Spring package (51), and the resulting boxed segments (approximately one per 2.75 nm repeat) were imported into RELION for further processing. Following 22 rounds of refinement with the entire (composite) data set, a tight filament mask was generated using the *relion_mask_create* tool (corresponding to a length of approximately 5 actin subunits), and an additional 4 rounds of refinement were performed. Reconstructed volumes were not symmetrized between successive refinement rounds. Following single subunit 3D classification, cofilactin and bare actin classes were independently refined using the same mask as in the composite data set.

The resolution and B-factor of the composite, bare actin, and cofilactin final maps were calculated from the Fourier shell correlation (FSC) of independent half-maps in postprocessing with RELION following gold standard protocols. Symmetry was first imposed in real space on the

independent half maps in the bare actin (27.42 Å rise, −166.63˚ twist) and cofilactin (27.24 Å rise, −162.5˚ twist) data sets using the *relion_helix_toolbox* command. The imposed helical parameters were derived from local searches of symmetry on the full map in RELION.

Obtaining continuous filament paths via smoothing and interpolation

Refined box segment *x* and *y* displacements were added to box segment coordinates to produce estimates of the subunit coordinates (*x*, *y*) with respect to the micrograph coordinate system. The distance (*d*) between consecutive subunit coordinate estimates was used to identify duplicates (i.e. cases where *RELION* refinements for two or more box segments were centered on the same subunit) or gaps (corresponding to subunits for which no centered box segment was identified); duplicate subunits were discarded, and the coordinates and Euler angles for 'gap' subunits were estimated by interpolation from measured values from neighboring points (Fig. 1H). The resulting estimates of subunit coordinates (*x*, *y*) and orientations (Euler angles ϕ, θ, ψ where ϕ represents the axial twist) were parameterized with respect to the subunit number (*n*), and this parameterization was used to perform a final smoothing step using the method of least trimmed squares (66). For smoothing, each of the coordinates (*x*(*n*), *y*(*n*), ϕ (*n*), $\theta(n)$, $\psi(n)$) was re-estimated by performing least-squares linear fitting using a 7-subunit window centered on *n*. For each estimated value, trimming was performed by enumerating all ways to select 5 of the 7 measured coordinate values (*x*, *y*, or ϕ) within the designated window (21 total possibilities) and choosing the combination that yielded the lowest residual. The corresponding fitting parameter values were used to re-estimate the given coordinate value located at subunit *n*.

Parametric fitting of the filament twist

The following theory and equations were developed by Wenxiang Cao from the De La Cruz laboratory. The measured, subunit-dependent twist angle, $\Delta\phi_n = (\phi_n - \phi_{n-1})$ (Fig. 2E-F), was fitted to a sigmoidal empirical function in the following form:

$$\Delta\phi(n) = \Delta\phi_i - \frac{\Delta\phi_i - \Delta\phi_f}{1+e^{\frac{n-n_0}{N_b}}} \quad \text{(Eq. 1)}$$

where n is the subunit number, n_0 is the midpoint of the twist transition, N_b is characteristic decay length of the twist transition, $\Delta\phi_i$ is asymptotic value of the twist angle at $n = -\infty$, and $\Delta\phi_f$ is the asymptotic value of the twist angle at $n = +\infty$.

The cumulative twist:

$$\boldsymbol{\Phi}_n = \sum \Delta\phi_i = \sum_{i=2}^{n}(\phi_i - \phi_{i-1}) = \phi_n - \phi_1 \quad \text{(Eq. 2)}$$

was transformed to the cumulative twist difference ($\boldsymbol{\Phi}_{n,\mathrm{diff}}$) by subtracting the cumulative twist of canonical, bare actin ($\phi_{i,\mathrm{bare}}$) according to:

$$\boldsymbol{\Phi}_{n,\mathrm{diff}} = \sum_{i=2}^{n}\left(\Delta\phi_i - \Delta\phi_{i,\mathrm{bare}}\right) = (\phi_n - \phi_{n,\mathrm{bare}}) - (\phi_1 - \phi_{1,\mathrm{bare}}) = \phi_n - \phi_{n,\mathrm{bare}} \quad \text{(Eq. 3)}$$

where we have set the value of $\phi_{1,\mathrm{bare}}$ (which is arbitrary) equal to ϕ_1. Experimentally determined values of $\boldsymbol{\Phi}_{n,\mathrm{diff}}$ (Fig. 2C-D) were fitted to the function $\boldsymbol{\Phi}_{\mathrm{diff}}(n)$, obtained by subtracting the twist of canonical, bare actin $\Delta\phi_{\mathrm{bare}}$ from Eq. 1 and integrating with respect to *n*:

$$\boldsymbol{\Phi}_{\mathrm{diff}}(n) = C_1 n + C_2 N_b \ln\left(1 + e^{\frac{n-n_0}{N_b}}\right) + C_3 \quad \text{(Eq. 4)}$$

where C_1, C_2, and C_3 are parameters determined by the fit.

Determining occupancies of individual sites

We used a combined particle subtraction and 3D classification strategy (67) as adapted for helical assemblies (34) to determine the cofilin occupancy of the central actin subunit in each

box segment. After reconstructing the composite map, pdb coordinates of actin (PDB ID 3J8I; (3)) and cofilactin (PDB 3J0S; (1)) filaments were fitted into the cryo-EM density of the central subunit using UCSF Chimera (68). A 'central subunit mask' was generated from these atomic models by generating a density map using the pdb2mrc tool of EMAN2 (69), low-pass filtering the map to 30 Å and generating a mask (10 Å soft edge) using the *relion_mask_create* tool from RELION. This central subunit mask was then subtracted from a mask of the full reconstructed filament using the *relion_image_handler* tool from RELION, and the resulting 'reverse' mask was used in conjunction with the composite map to generate a new stack of box segments from which all but the central subunit had been subtracted. This 'subtracted' particle stack was then separated into 2 classes with a subsequent round of masked 3D classification, using the central subunit mask and constraining the particle shift and Euler parameter values to those obtained from the prior refinement. Unsubtracted box segments corresponding to the two classes were then separately subjected to an additional refinement step (15 iterations for the actin class, 22 iterations for the cofilactin class), using a newly-generated tight subunit mask (length of ~9 subunits).

Boundary selection for reconstruction

The resulting 3D classification data were screened for specific patterns of cofilin decoration along filaments using a script coded in the awk unix language. Barbed boundaries were defined as 5 contiguous bare subunits adjacent to 5 contiguous cofilin bound subunits from the barbed to the pointed end of filament segments. Pointed end boundary searches used the same pattern of decoration in the reverse order. Isolated, bound cofilin was arbitrarily defined as a cofilin-occupied site, flanked by 4-5 contiguous bare sites to avoid potential confounding effects from nearby decorated sites. Specific subunits from each pattern of decoration were selected and

assembled into new particle stacks, maintaining particle parameters derived from the composite map refinement. These particle stacks were randomly halved for FSC calculations.

S3D cofilactin refinement and 3D Classification

A published cryo-EM data set (19) of actin filaments partially decorated with S3D-cofilin was re-analyzed. All filament segments were manually boxed with *e2helixboxer* from the EMAN software package (65) and refined together in RELION. Following filament smoothing (44), a class of single, isolated S3D-cofilin was identified by masked 3D classification focused on the 5 central subunits of the map (N = 8 total classes). Particles within 3 subunits of filament segment ends were removed from this class. Other classes yielded by this analysis represented either fully decorated or bare stretches of actin, and therefore could not be used to conclusively locate boundaries of larger (C > 1) clusters.

Subunit tilt measurements

Maps centered on each subunit of each boundary type were reconstructed to place the measured subunit at the center of the resulting map. Models of the actin inner domain and outer domain were derived from recent models by Chou and Pollard (52) using definitions from Holmes (70), and modified by removal of the D-loop from the outer domain. These models were independently fit into the central subunit cryo-EM density with the '*Fit in Map*' tool in UCSF Chimera (68). Models of bare (PDB ID 6DJO (52)) and cofilactin (PDB ID 5YU8 (42)) were subsequently aligned to the position of the fitted inner domain model using the '*Matchmaker*' command. Next, the tilt between the outer domain of the reference models and the fitted outer domain was calculated with the '*measure rotation*' command.

Intersubunit twist measurements from reconstructed maps

Models of the actin inner domain (PDB ID 6DJO (52)) were fit into the 5 central subunits of each map using the '*Fit in Map*' command in UCSF Chimera (68). The twist rotation between 2

adjacent subunits was measured using the '*measure rotation*' command and assigned to the subunit on the pointed end. The cumulative twist difference (44) was calculated by summing these subunit twist measurements from the barbed to the pointed end of the filament, and subtracting from that the cumulative twist of a reference bare actin filament.

Simulation of cofilin binding kinetics

These methods were developed and the simulations performed by our collaborators in the De La Cruz laboratory. Simulated time courses of cofilin binding to actin filaments were implemented with the Gillespie Monte Carlo algorithm, treating actin filaments as an Ising model with nearest-neighbor cooperative interactions (71). Briefly, the Gillespie algorithm is an event based variable time step algorithm which we found yielded better overall performance than previous fixed time step approaches (72). In the Gillespie algorithm, each time step, τ, is chosen stochastically where

$$\tau = \frac{1}{k_s} \ln (1/r).$$

Here, r, is a random number sampled from a uniform distribution between 0 and 1 and k_s is sum of all forward and reverse rate constants, representing all binding and unbinding reactions:

$$k_s = (k_+[C_{free}](f_{iso} + f_{sc}\omega_+ + f_{dc}\omega_+^2)) + (k_-(b_{iso} + b_{sc}\omega_- + b_{dc}\omega_-^2))$$

Here $[C_{free}]$ is the concentration of free cofilin, f_{iso}, f_{sc}, and f_{dc} are the number of available free ligand binding sites that are isolated, singly contiguous, and doubly contiguous, resp., and b_{iso}, b_{sc}, b_{dc} are the numbers of actin subunits that are bound with isolated, singly contiguous, and doubly contiguous cofilin, resp. Within that time step, an event is then chosen based on the relative rate constants of the 6 possible events. Specifically, the probability (p_i) of a specific event being chosen is given by:

binding to free isolated site (event 1): $p_1 = \frac{k_+[C_{free}]f_{iso}}{k_s}$

binding to free singly contiguous site (event 2):

$$p_2 = \frac{k_+ \omega_+ [C_{free}] f_{sc}}{k_s}$$

binding to free doubly contiguous site (event 3):

$$p_3 = \frac{k_+ \omega_+^2 [C_{free}] f_{dc}}{k_s}$$

dissociation of isolated bound cofilin (event 4):

$$p_4 = \frac{k_- b_{iso}}{k_s}$$

dissociation of singly contiguous bound cofilin (event 5):

$$p_5 = \frac{k_- \omega_- b_{sc}}{k_s}$$

dissociation of doubly contiguous bound cofilin (event 6):

$$p_6 = \frac{k_- \omega_-^2 b_{dc}}{k_s}$$

To determine which of the six possible events takes place, an additional random number r_2 is sampled from a uniform distribution between 0 and 1. The event μ is chosen that satisfies the following relation:

$$\sum_{i=1}^{\mu-1} p_i < r_2 \leq \sum_{i=1}^{\mu} p_i$$

Once the type of event is chosen, a specific location *j* of that event is chosen by random sampling from all available locations for that event. The concentration of free cofilin and actin lattice configuration are updated, and the algorithm iteratively proceeds until equilibrium is achieved.

To simulate special cases with defined critical cluster sizes required for cooperativity (*i.e.* "nuclei", *N*), the definitions for the types of actin sites are modified as follows. A given free, unoccupied cofilin binding site is classified f_{iso} if both of its nearest neighboring sites (left and

right) contain a cluster of contiguously bound cofilin (*C*) smaller than nucleus, *N*. A free site is classified f_{sc} if at least *N* consecutive cofilin are bound on either the left or right side. f_{dc} sites have at least *N* contiguously bound cofilins on both their left and right sides. The definitions for cofilin-occupied sites work similarly, where the number of contiguously bound cofilins on the left and right sides of a given bound cofilin dictates the site classification.

Model refinement and validation

Cryo-EM density maps were globally sharpened using *AutoSharpen* (73) in phenix (74). We used PDB ID 6DJN (52) as an initial model for the bare actin structure after manually removing the phosphate group, and PDB ID 5YU8 (42) as an initial model for the cofilactin structure after mutating the chicken cofilin-2 sequence to match human cofilin-1. These initial models were refined against their respective maps with real-space refinement in phenix. Simulated annealing was applied in the initial round of refinement. Substantial model displacements from the cryo-EM density were corrected manually with real-space refinement in Coot (75), followed by additional rounds of real-space refinement without simulated annealing in phenix. Next, models were manually edited in Coot to remove geometric outliers, rotamer outliers, and severe steric clashes, with progress monitored by MolProbity (76).

Chapter II. Structural basis of the filamin A actin-binding domain interaction with F-actin

Introduction

Actin crosslinking proteins mediate assembly of actin filaments into higher-order structures, such as bundles and orthogonal networks, that play essential roles in determining cell morphology and behavior(2, 77). Defects in the actin cytoskeleton underlie numerous genetic diseases, and can arise from missense mutations in the actin-binding domains (ABDs) of these crosslinking proteins(29, 30, 33). Crystal structures of isolated ABDs have shown that they are composed of tandem calponin homology (CH) domains(29-32) but a complete molecular understanding of actin-binding or its perturbation in disease has been hampered by the lack of a high-resolution structure of any actin-crosslinking protein bound to actin filaments.

Prior to publication of the first ABD crystal structures, three ABD actin-binding sites (ABS1, ABS2 and ABS3) were predicted based on peptide and fragment binding studies and mutagenesis of a variety of ABDs (78-82). However, their precise boundaries and relative contributions to actin filament binding were controversial. ABD crystal structures subsequently revealed that the three putative ABSs do not form a continuous surface and include many buried residues (29, 32, 83). Indeed, ABS1, which lies in the first helix of CH1, is largely buried at the interface between CH1 and CH2 in the “closed” conformation of the ABD observed in most crystal structures (83-85). This, together with biophysical experiments and electron microscopy studies of ABDs bound to actin filaments (86-91), led to models where inter-domain rearrangement opens the tandem CH domains, exposing CH1 domain actin-binding sites and removing steric clashes between CH2 and actin that would prevent binding. The conformational equilibrium between “closed” and “open” states would thus determine ABD binding to actin filaments but the identity of the actin-binding residues and the nature of the conformational changes remained to be determined.

To understand the molecular basis of ABD binding to actin we investigated the essential actin-crosslinking protein filamin A (FLNa), which is composed of an N-terminal ABD followed by 24 immunoglobulin-like domains, the last of which mediates homodimerization (92). In addition to crosslinking actin filaments, FLNa binds numerous scaffolding, signaling, and transmembrane proteins, and so plays vital roles in the regulation of cell morphology, adhesion, migration, differentiation, and mechanical force sensing (28, 93). Consistent with these essential roles, nonsense or frameshift mutations in the gene for FLNa, which is on the X chromosome, are typically embryonically lethal in males (33, 94). In heterozygous females, null FLNa mutations cause periventricular nodular heterotopia (PVNH), a neuronal differentiation or migration disorder often associated with cardiovascular abnormalities (95, 96). Notably, PVNH can also be caused by rare missense mutations that cluster in the FLNaCH1 domain, suggesting that these point mutations result in a loss of function, possibly by disrupting actin binding, but this has not been experimentally tested (95, 97). In contrast, missense point mutations in the FLNaCH2 domain are linked to developmental malformations associated with otopalatodigital syndrome spectrum disorders (OPDSD). Unlike PVNH mutations, OPDSD mutations are believed to confer a gain-of-function effect on FLNa (32, 98, 99) and in the case of the E254K mutation increased affinity for actin filaments has been reported (32).

Here, I describe the published results (26) of a collaboration with Daniel Iwamoto, a former graduate student from the Calderwood laboratory at Yale University. I employed cryo-EM to solve the structure of FLNa constructs bound to actin filaments and refined an atomic model of FLNa-E254K, while Daniel performed biochemical and cellular assays on structure-guided mutants. Together, our research characterizes the mechanism of ABD binding to actin and provides a molecular explanation to rationalize FLNa human disease mutations.

Results

A high-affinity FLNaABD mutant reveals the actin-binding interface at near-atomic resolution

To understand FLNaABD binding to actin and potentially explain the molecular basis of disease mutations, I used cryo-EM to visualize the complex between actin filaments and a FLNaABD construct encompassing the N-terminal 42 residues plus the tandem CH domains. In initial experiments with WT FLNaABD and phalloidin-stabilized actin filaments on an FEI F20 Tecnai electron microscope I was only able to reproduce low-resolution structures similar to those seen in other ABD-F-actin structures and only the CH1 domain was evident (88, 91) (Fig. 11a). In an attempt to improve ABD decoration of actin filaments and increase resolution, I performed experiments using FLNaABDs containing OPDSD-associated gain-of-function point mutations in FLNaCH2 (32). This yielded 6.6 Å and 7.4 Å resolution maps for the Q170P and E254K mutants respectively (Fig. 11b, c). Notably, the FLNaABD-E254K map included density for the CH2 domain, albeit at lower resolution (Fig. 11c). I therefore used a Titan Krios electron microscope to image FLNaABD-E254K in complex with actin filaments, allowing me to approach atomic resolution, resolving both the CH1 domain and actin to 3.6 Å resolution (Fig. 12a). The CH2 domain was also visible but again was at lower resolution and is described further in later sections. The actin structure in the complex is indistinguishable from previously reported structures of phalloidin-stabilized actin filaments (PDB 6C1D, root mean square deviation [RMSD] of Cα atoms in residues T5-C374 is 0.713 Å) (34).

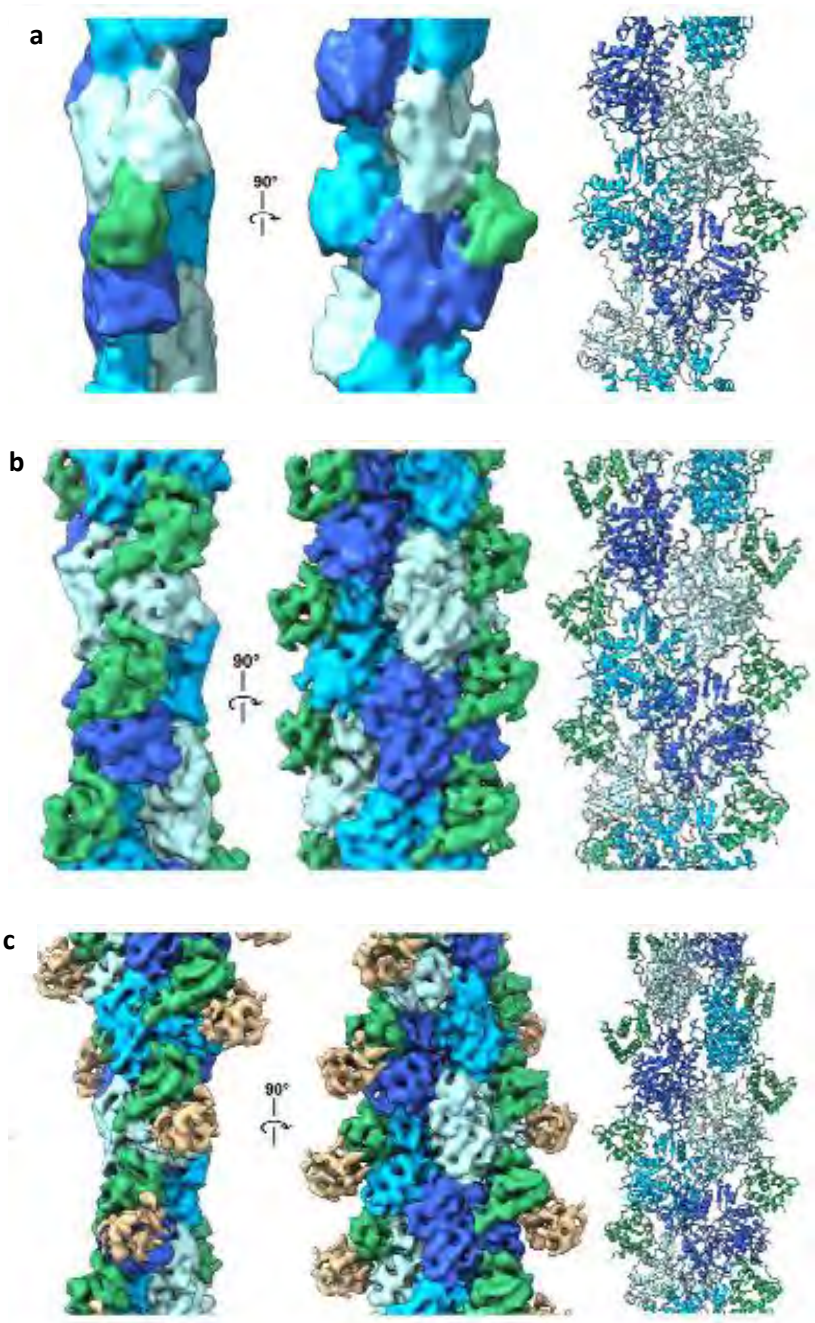

Figure 34. FLNaABD-actin complexes. a A 10 Å-filtered cryo-EM density map of WT FLNaABD (left and middle) was rigid-body docked with crystal structures for actin (PDB 6C1D, different subunits in dark blue, cyan, and light blue) and FLNaCH1 (PDB 3HOP, green) (right). **b** A 6.6 Å-filtered cryo-EM density map of the gain-of-function mutant FLNaABD-Q170P (left and middle) was docked with the refined actin and FLNaCH1 models (right) and colored as in (**a**). **c** A 7.4 Å-filtered cryo-EM density map of the gain-of-function mutant FLNaABD-E254K (left and middle) was docked with the refined actin and FLNaCH1 models (right) and colored as in (**a**). Observed extra density (tan) for FLNaCH2 could not be reliably docked with a FLNaCH2 model.

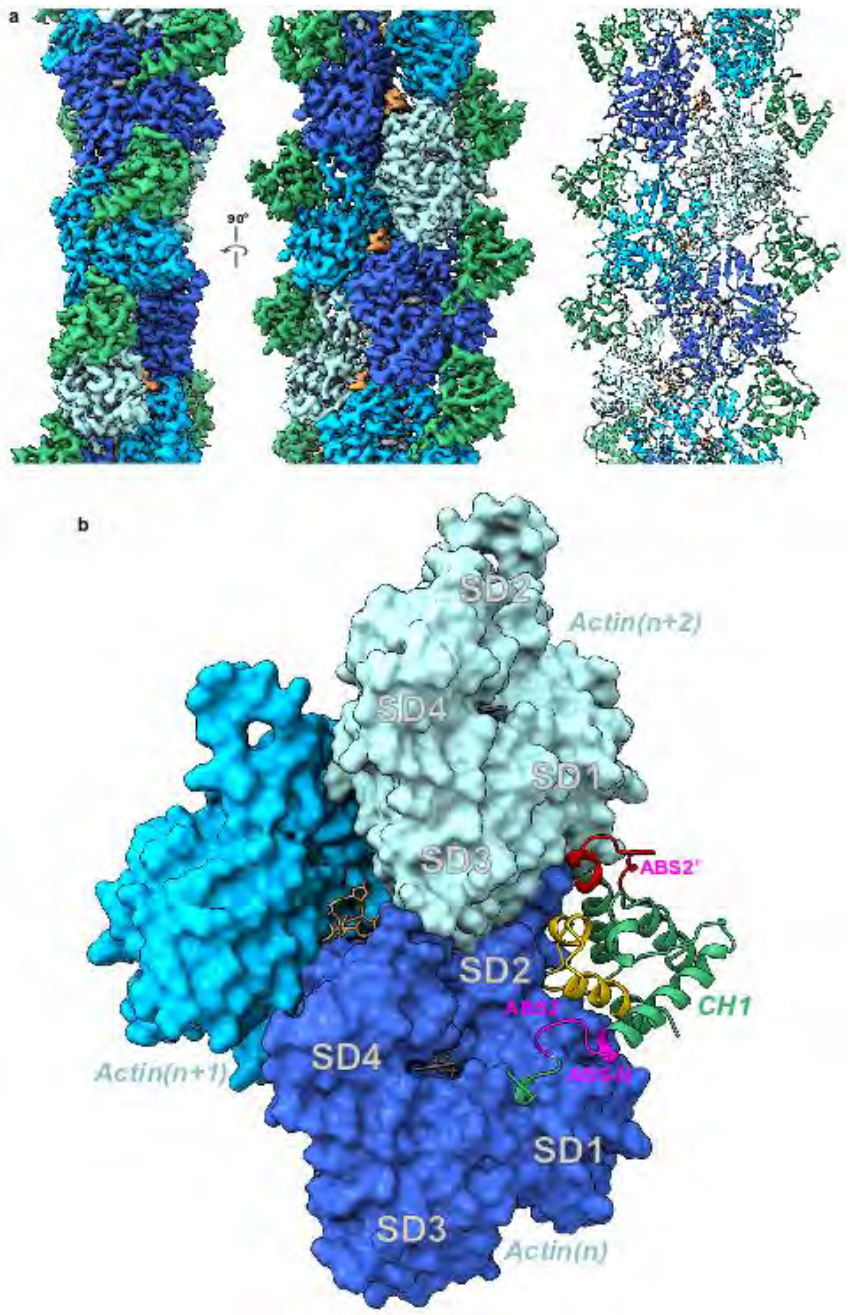

Figure 35. Cryo-EM map and model of FLNaABD-E254K bound to actin. a The cryo-EM map (left and middle) has been filtered to 3.6 Å resolution, masked to illustrate the actin and FLNaCH1 region, and fit with computationally refined models (right) for actin (different subunits in dark blue, cyan, and light blue) and the FLNaCH1 domain (green). Phalloidin (orange) and Mg.ADP (grey) were resolved within actin. **b** The binding interface of the FLNaABD (green ribbon) consists of the N-terminal actin-binding site ABS-N (pink), actin-binding site 2 (ABS2, yellow) and the ABS2 extension (ABS2', red), which makes contacts with actin subunits (*n*) (dark blue, surface representation) and (*n*+2) (light blue, surface representation) on actin subdomains 1 and 2 (SD1 and SD2, labeled in grey).

Until now, mapping actin-binding sites (ABS) in ABDs has been contentious; three putative sites (ABS1, 2, and 3) have been proposed but there has been a lack of consensus on the boundaries of these sites and crystallographic data have been unable to reconcile these sites with a continuous binding surface (29, 32). Contrary to prior predictions, my structure reveals that neither the proposed ABS1 (coarsely mapped to residues 46-56) in helix-A of CH1 nor ABS3 (residues 163-181) in helix-A of the CH2 domain directly engages actin. Instead, the ABD binds actin filaments through a short sequence immediately N-terminal to the CH1 domain (residues L35-K42) which we term ABS-N, as well as the predicted ABS2 (residues V122-W142), and structurally adjacent residues R91-L104 which were not previously implicated in actin binding and which we term ABS2' (Fig. 12b). These sites mediate ABD binding in the groove between subdomains 1 and 2 on one actin monomer (*n*) (1348 $Å^2$ of buried surface area) and subdomain 1 on the adjacent (*n+2*) monomer (burying 505 $Å^2$) (Fig. 12b).

FLNa residues immediately N-terminal to CH1 contribute to F-actin binding

Although most of the actin-bound FLNaCH1 domain in my cryo-EM structure closely resembles that of the unbound FLNaABD-E254K crystal structure (PDB 3HOC, RMSD of Cα atoms in residues A39-S149 is 1.094 Å) the first turn of helix-A rearranges to engage actin and I can resolve additional N-terminal residues 29-38 which were largely disordered in prior FLNa X-ray structures (31, 32) (Fig. 13a,b). To test the importance of this region in actin binding, Daniel Iwamoto from the Calderwood laboratory generated a series of N-terminal truncations of C-terminally GFP-tagged FLNaABD constructs (FLNaABD-GFP) and assessed co-localization with actin filaments in transfected NIH-3T3 fibroblasts. He found that loss of amino acids 1-27 or 1-32 had no impact on actin co-localization, loss of 1-37 or 1-40 partially inhibited co-localization, and loss of 1-44 abrogated it (Fig. 13c,d) – implicating residues 33-44, encompassing ABS-N, in actin binding. Of these N-terminal residues, only 37-44 are visible in FLNaABD X-ray crystal structures

(31, 32), forming the N-terminus of the first α helix (helix-A). In the actin-bound conformation, the N-terminus of helix-A is deformed, moving up to ~3Å (Fig. 13b) to engage actin via a probable cation-π interaction between W41 (conserved in the ABD of all filamins and α-actinins) and actin R28, potentially buttressed by additional interactions with actin F21 and R95 (Fig. 13e,f). Mutating W41 inhibited FLNaABD targeting to actin filaments in cells (Fig. 13g,h), further supporting the importance of this region in actin binding. Moreover, our collaborators previously reported that a double K42R,K43R mutation in FLNa helix-A inhibits actin binding (100) and my structure shows that K42 may help stabilize ABS-N. Residues N-terminal to helix-A also contribute to actin binding and the importance of hydrophobic contacts between L35 and actin as seen in my structure is supported by the strongly impaired actin targeting of an L35A mutant (Fig. 13g,h). Together our structural and functional studies firmly establish the biological relevance of ABS-N in ABD-actin binding. Furthermore, despite low sequence conservation of this region, recent biochemical studies on utrophin (101) and a lower-resolution cryo-EM structure of the actin-bound β-III-spectrin ABD (91) indicate a general role of the ABD N-terminus in actin binding.

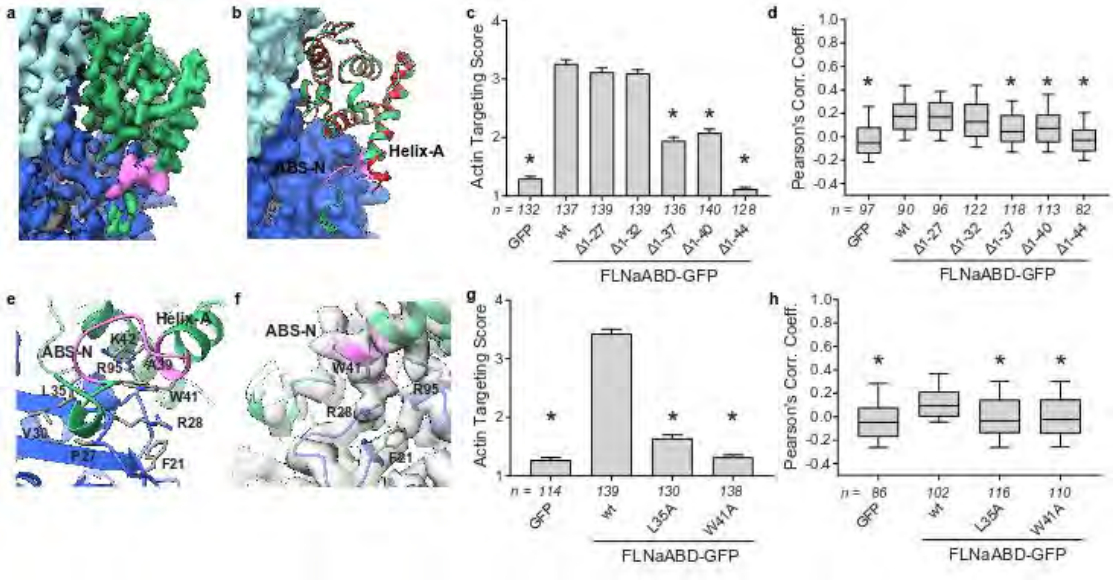

Figure 36. ABS-N contributes to actin binding. a Cryo-EM density depicting ABS-N (residues P29-K43, pink) extending from helix-A of the FLNaCH1 domain (green) alongside actin (*n*) (dark blue). **b** Superposition of the refined actin-bound FLNaCH1 and ABS-N (green, pink) cryo-EM structure and the published unbound FLNaCH1 crystal structure PDB 3HOC (red) illustrates the formation of the structured ABS-N upon actin-binding. Actin in surface representation and FLNa in ribbon representation, colored as in (**a**). **c** Actin filament targeting of WT and N-terminal deletion constructs of FLNaABD-GFP expressed in mouse NIH-3T3 fibroblasts. Bars = mean ± SEM. n≥128 cells/condition from 3 independent experiments. **d** Pearson's correlation coefficient (PCC) scoring of FLNaABD-GFP co-localization with N-terminal truncations. Boxes, 25th through 50th and 50th through 75th percentile; whiskers, 10th through 90th percentile, n≥82 cells/condition from 3 independent experiments. **e** Detailed view of actin-binding by ABS-N with binding residues in stick representation. **f** Cryo-EM density supports a probable cation-π interaction between FLNa W41 and actin R28. **g** F-actin targeting of ABS-N-mutant FLNaABD-GFP as scored in (**c**). Bars = Mean ± SEM. n≥114 cells/condition from 3 independent experiments. **h** PCC scoring of ABS-N-mutant FLNaABD-GFP. n≥86 cells/condition from 3 independent experiments. * significantly different from FLNaABD-wt targeting, $p < 0.05$, ANOVA with Dunnett's post hoc test.

ABS2' and ABS2 facilitate binding in the groove between adjacent actin subunits

Beyond the ABS-N site, the remaining ABD interface with actin is mediated by ABS2 and ABS2'. ABS2' extends from the middle of the C-E loop into the N-terminus of helix-E and engages both subdomain 2 of the primary interacting actin subunit (*n*) and subdomain 1 of the adjacent actin (*n+2*) – mainly via hydrophobic and H-bonded interactions (Fig. 14a). Our collaborators validated the importance of these interactions by mutating R91, which is well positioned to form an H-bond with T351 in actin (*n+2*), F99 which contacts I345 in actin (*n+2*), and L104 which is stabilized by CH1-V130 to make a hydrophobic contact with M47 in actin (*n*). R91E, F99A, and L104A mutations each inhibited binding in the cellular actin filament targeting assay (Fig. 14b,c). ABS2 encompasses part of the E-F loop, the short helix-F and the N-terminal half of helix-G, and engages actin (*n)* subdomains 1 and 2 (Fig. 14d). Our collaborators previously reported that a K135R substitution in ABS2 strongly inhibits actin binding (100) and now show that the K135A mutation has a similar effect (Fig. 14e,f). K135 is highly conserved across all ABDs and its sidechain density is directly resolved, indicating potential ionic interactions with actin E93 and D56 (Fig. 14d). The importance of ABS2 is further supported by the strong inhibition of actin targeting of a charge-reversing lysine mutation at D125, which forms an ionic bond with K61 and potentially H-bonds with Y53 on actin (Fig. 14d-f).

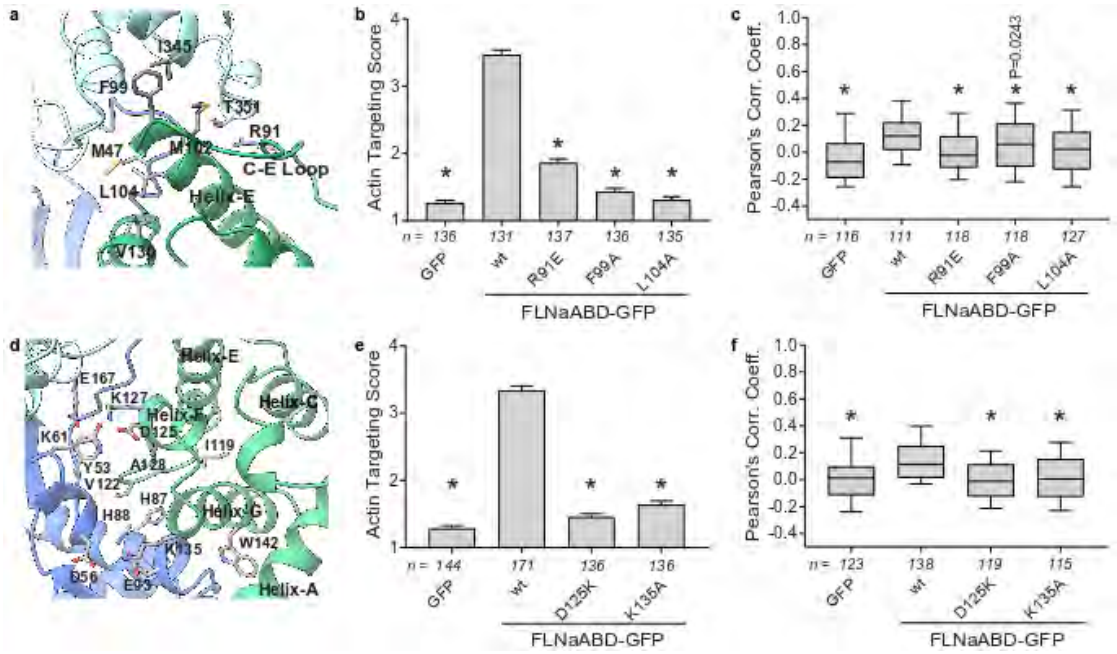

Figure 37. ABS2 and ABS2' facilitate major binding interactions with actin. a Detailed view of the FLNa ABS2' (green) binding interface with the actin (*n*+2) subunit (light blue) and actin (*n*) (dark blue). **b** Actin filament targeting scores of ABS2'-mutant FLNaABD-GFP. Bars = Mean ± SEM. n≥131 cells/condition from 3 independent experiments. **c** PCC scoring of ABS2'-mutant FLNaABD-GFP. n≥111 cells/condition from 3 independent experiments. **d** Detailed view of the FLNa ABS2 (green) binding interface with the actin (*n*+2) subunit (light blue) and actin (*n*) (dark blue). **e** Actin filament targeting scores of ABS2-mutant FLNaABD-GFP. n≥129 cells/condition from at least 3 independent experiments. Bars = Mean ± SEM. **f** PCC scoring of ABS2-mutant FLNaABD-GFP. n≥119 cells/condition from 3 independent experiments. * significantly different from FLNaABD-wt targeting, $p < 0.05$, ANOVA with Dunnett's post hoc test.

FLNaABD-E254K binds actin in an open conformation

Further examination of my structure reveals the necessity for significant CH2 domain reorientation to prevent steric clashes with actin upon ABD binding. In my WT and OPDSD mutant Q170P structures (Fig. 11a,b), as well as other published lower-resolution structures (87, 88, 91), density for the CH2 domain was not evident, consistent with CH2 domain motion in the actin-bound form. In contrast, in both my F20 and Krios E254K structures the CH2 domain is apparent, albeit with weaker cryo-EM density and at lower resolution than the rest of the map (Fig 11c, 15a). The lower resolution of this domain again indicates its mobility but was sufficient to reveal that it is oriented outwards and away from actin. Comparison of my actin-bound FLNaABD-E254K structure with the closed conformation seen in the FLNaABD-E254K crystal structure (32) indicates that the closed conformation is incompatible with actin filament binding. As reported previously for α-actinin (88), superposition of the CH1 domains in the actin-bound crystal structures reveals that, in the closed conformation, CH2 would clash with actin (Fig. 15b). We therefore conclude that an outward movement of the CH2 domain facilitates CH1-mediated binding to actin (Fig. 15c). Consistent with this model, isolated FLNaCH1-GFP strongly targeted to F-actin (100) while FLNaCH2-GFP showed no targeting, even with OPDSD mutations Q170P or E254K which otherwise promote ABD targeting (Fig. 15d,e).

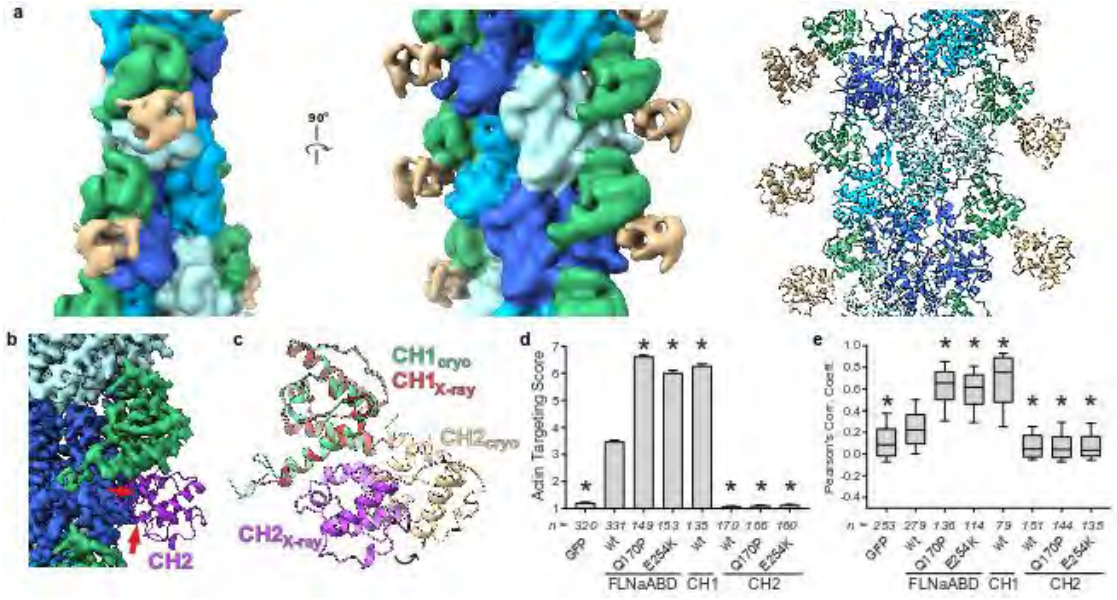

Figure 38. Opening of the ABD is required to avoid steric clashes and facilitate actin binding. **a** Low-pass filtered (10 Å resolution) map of FLNaABD-E254K bound to actin. FLNaCH2 from the FLNaABD crystal structure (PDB 3HOC) was independently rigid-body docked into additional density (tan, right). **b, c** The FLNaABD crystal structure is superimposed onto the actin-bound cryo-EM structure to align CH1 domains. Instances of steric clash between the crystallographic CH2 domain (purple) and F-actin cryo-EM density are indicated by red arrows (**b**). Repositioning of the CH2 domain from the closed crystalized form (purple) into its open actin-bound form (tan) is depicted with an arrow (**c**). **d** Actin-targeting scores of FLNa-ABD, -CH1, or -CH2-GFP with OPDSD mutations. n≥135 cells/condition from at least 3 independent experiments. Bars = Mean ± SEM. **e** PCC scoring of FLNa-ABD, -CH1, or -CH2-GFP with OPDSD mutations. n≥114 cells/condition from at least 3 independent experiments. * significantly different from FLNaABD-wt targeting, $p < 0.05$, ANOVA with Dunnett's post hoc test.

In addition to avoiding steric clashes with actin, my structure reveals that CH2 reorientation also exposes a previously-unrecognized and highly-conserved actin-binding residue (W142) at the C-terminus of ABS2. Notably, in unbound FLNaABD crystal structures W142 interacts with H255 in CH2, possibly 'latching' the ABD in a closed conformation (Fig. 16a). In contrast, in my actin-bound structure, this interaction is replaced by hydrophobic contacts between W142 and actin (Fig. 16b), and a W142A mutation inhibited targeting to actin filaments in cells (Fig. 16c,d). These data argue that W142 plays a regulatory role by binding either CH2 in a closed inhibitory state, or actin filaments in the open active conformation. In α-actinin-4, the homologous W147 may serve a similar role by engaging K255 in CH2. Consistent with this, K255 mutations that presumably unlatch the ABD and increase affinity for actin are associated with the kidney disease focal segmental glomerulosclerosis (102). Indeed, disease-associated gain-of-function mutations are found throughout the CH2 domain of FLNa and other ABDs including in its hydrophobic core. In further scanning fluorimetry experiments performed by Daniel Iwamoto, purified OPDSD-associated mutant FLNaABDs (Q170P or E254K) exhibited sharp melting points at lower temperatures than WT FLNaABD, indicative of altered stability (Fig. 16e). Consistent with their enhanced actin filament targeting (Fig. 15d,e), OPDSD-associated ABD mutants also displayed increased affinity for actin in co-sedimentation assays (Fig. 16f,g). We hypothesize that OPDSD mutations destabilize the CH2 domain in the closed ABD position and shift the conformational equilibrium in favor of ABD opening, facilitating CH1-mediated actin binding.

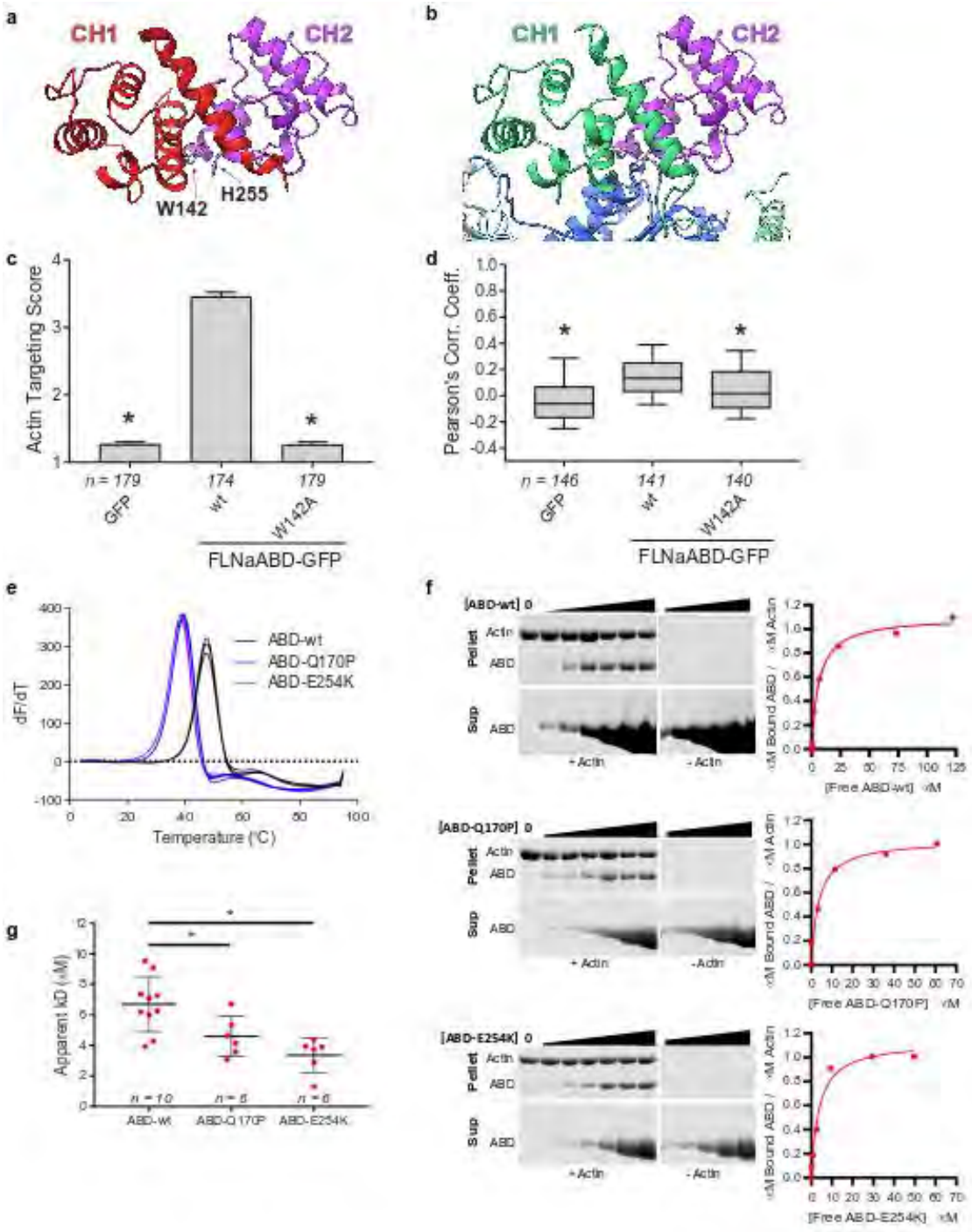

Figure 39. ABD opening is mediated by an inter-CH domain latch. a FLNaABD crystal structure showing the W142-H255 cation-π interaction that may latch the CH1 (red) and CH2 (purple) domains closed. **b** Actin-bound FLNaCH1 (green) reveals W142 interaction with actin (dark blue). In the closed CH2 conformation (purple) H255 would clash with actin. **c** F-actin targeting score of the W142A mutant FLNaABD-GFP. n≥174 cells/condition from at least 3 independent experiments. Bars = Mean ± SEM.

Figure 16. (Continued) d PCC scoring of the W142A-mutant FLNaABD-GFP. n≥119 cells/condition from at least 3 independent experiments. * significantly different from FLNaABD-WT targeting, $p < 0.05$, ANOVA with Dunnett's post hoc test. **e** Triplicate derivative melting curves from differential scanning fluorimetry for purified WT, Q170P, and E254K FLNaABDs indicate a single melting temperature peak for each protein: WT = 48.1 ± 0.6 °C, Q170P = 40.1 ± 0.8 °C, E254K = 39.3 ± 0.5 °C (± SD). **f** Left, representative Coomassie-stained actin co-sedimentation assay gels containing pellet (top) or supernatant (bottom) samples with no-actin controls (middle) for purified WT, Q170P, and E254K FLNaABDs. On the right, assay data points were plotted to generate a binding curve to calculate an apparent dissociation constant (K_d). **g** Apparent K_d was averaged for each ABD from at least six co-sedimentation assays. Bars = Mean ± SEM. * $p < 0.05$, ** $p < 0.005$, unpaired two-tailed t-test

Filamin A CH1 domain disease mutations confer loss of function

In addition to the gain-of-function CH2 domain mutations that cause OPDSD, mutations in FLNa are also linked to the neuronal migration disorder PVNH (95). Most FLNa PVNH mutations are nonsense and frameshift resulting in the loss of FLNa protein (33, 95). However, rare PVNH-associated missense mutations that cluster in the FLNaCH1 domain are also seen, and result in phenotypically similar, albeit somewhat milder, disease (95). We propose that these mutations, many of which are found in the ABS-N, ABS2 and ABS2', disrupt the actin-binding interface and cause a loss-of-function. Consistent with this, experiments performed by our collaborators in the Calderwood laboratory demonstrate that the PVNH mutations A39G and A128V strongly impaired FLNaABD targeting to actin filaments in cells (Fig. 17a,b) and actin filament binding in *in vitro* co-sedimentation assays (Fig. 17c,d). Furthermore, their ability to purify soluble recombinant FLNaABD mutants with size-exclusion chromatography profiles consistent with monomeric protein (Fig. 18a) argues that the mutations do not result in general misfolding. This conclusion is supported by their sharp melting points in differential scanning fluorimetry experiments also performed by Daniel Iwamoto (Fig. 17e). Notably, despite a WT elution profile and melting point (Fig 17e, 18a), indicating that FLNaABD A39G is properly folded, it does not appear to bind actin with the 1:1 ratio seen for the WT and other gain- and loss-of-function

mutations (Fig 17c). This suggests an anomalous binding mechanism. We propose that A39 (in ABS-N) normally stabilizes the actin-binding residue W41 (Fig. 13e,f). While loss of this stabilization is likely to account for the observed reduction in binding affinity, it is difficult to envisage how it also alters stoichiometry of binding, either by occluding adjacent binding sites or by altering actin conformation. As this low-occupancy low-affinity interaction is not conducive to structural analysis we cannot currently explain the reduced stoichiometry of FLNaABD A39G. For a second PVNH mutation, A128V, we note that A128 does not make direct contact with actin but packs tightly behind the main interacting surface of ABS2 (helix-F). An A128V substitution would perturb this surface (Fig. 18b), likely explaining its disruption of actin binding and possibly contributing to the decrease in thermal stability seen in scanning fluorimetry experiments (Fig. 17e). My structure also allows us to rationalize the previously unexplained M102V PVNH-associated mutation which lies in ABS2' and inhibited actin binding in cells (Fig. 17a,b). M102, in conjunction with F99, extends towards I345 of actin (*n+2*) (Fig. 14a) and substitution with the shorter valine likely prevents this interaction. Two other PVNH-associated FLNa mutations that lie outside the actin-binding interface (E82V and S149F) had little or no effect on actin targeting, producing only modestly reduced actin-targeting scores but no reduction in Pearson's correlation coefficient (Fig. 17a,b, 18c), and the basis for their clinical effects remains unclear. Additional FLNaCH1 domain PVNH mutations also occur in ABS2. The V122 side chain is wedged between H87 and H88 of actin (*n*) and a V122G mutation strongly inhibited association with actin filaments (Fig. 17a,b). The K127N severely inhibited actin targeting, and in my structure K127 is in range to make an ionic bond with E167 in actin (*n+2*) (Fig. 17a,b). Notably, disease-associated mutations in the ABD of FLNc and α-actinin-2 also localize to regions corresponding to FLNa ABS2 (103, 104). Mutations at I119 inhibited actin binding (Fig. 17a,b), probably due to

disruption of the hydrophobic core of CH1, and α-actinin-1 and -2 also contain disease-associated mutations in this region (105, 106).

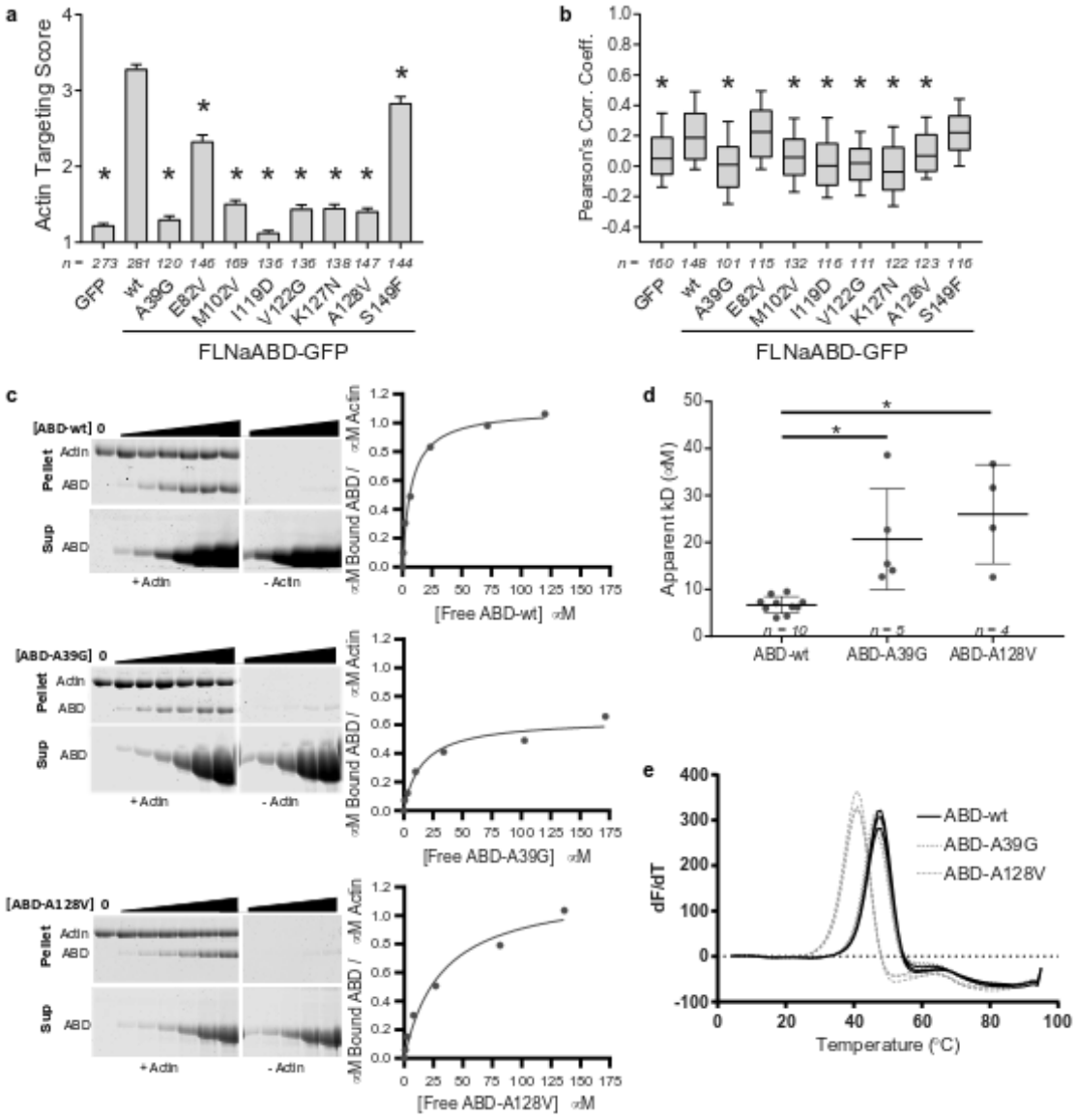

Figure 40. FLNaCH1 domain mutations confer a loss-of-function to actin binding. a Actin filament targeting scores of periventricular nodular heterotopia disease mutant FLNaABD-GFP. n≥120 cells/condition from at least 3 independent experiment. Bars = Mean ± SEM. **b** PCC scoring of periventricular nodular heterotopia disease mutant FLNaABD-GFP. n≥101 cells/condition from at least 3 independent experiments. * significantly different from FLNaABD-WT targeting, $p < 0.05$, ANOVA with Dunnett's post hoc test. **c** Left, representative Coomassie-stained actin co-sedimentation assay gels containing pellet (top) or supernatant (bottom) samples with no-actin controls (middle) for purified WT, A39G, and A128V FLNaABDs. On the right, assay data points were plotted to generate a binding curve to calculate an apparent dissociation constant (K_d). **d** Apparent K_d was averaged for FLNaABD-wt, -A39G, or -A128V protein from at least four assays (wt here is the same as appears in Fig. 16g for comparison purposes). Bars = Mean ± SEM. ** $p<0.005$, **** $p<0.0001$, unpaired two-tailed t-test.

Figure 17. (Continued) e Triplicate derivative melting curves from differential scanning fluorimetry for purified wt, A39G, and A128V FLNaABDs indicate a single melting temperature peak for each protein (wt here is the same as appears in **Fig. 16e** for comparison purposes): wt = 48.1 ± 0.6 °C, A39G = 47.3 ± 0.5 °C, A128V = 42.0 ± 0.9 °C (± SD).

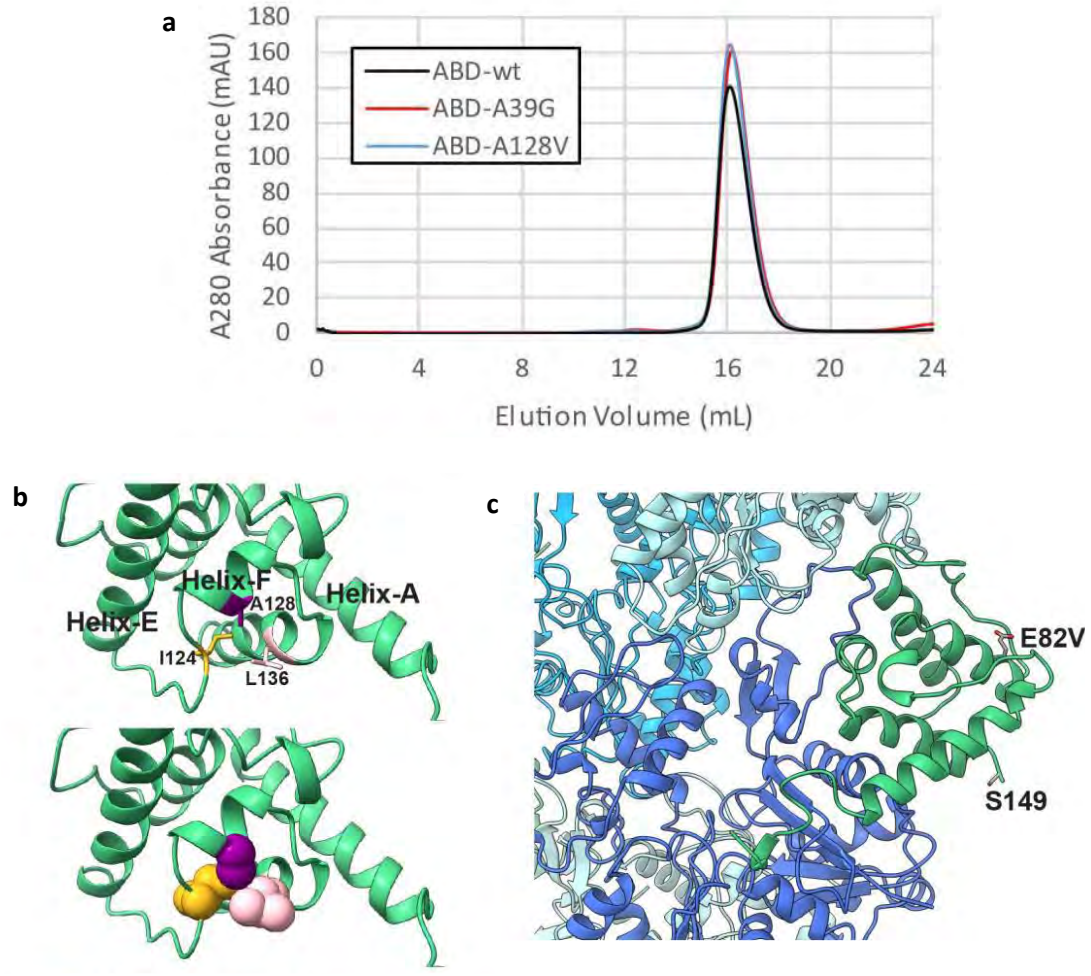

Figure 41. PVNH-associated mutations inhibit FLNaABD association with actin. a Analytical size-exclusion chromatography of purified bacterially expressed 6x-His-FLNaABD-WT, -A39G, or -A128V. **b** Top, the A128 residue is located in Helix-F of the CH1 domain and does not contact actin, though its mutation to valine would likely perturb this short helix (see space-filling models, bottom) which contains important actin-binding residues (not shown) and result in a loss of actin binding. **c** The FLNaCH1 E82 and S149 residues (mutated in PVNH) are situated far from actin binding sites in the actin-bound cryo-EM structure.

Discussion

My high-resolution cryo-EM structure of FLNaABD-E254K bound to actin filaments provides a detailed foundation for understanding the molecular basis of actin binding by tandem CH domains, revealing several new features of the ABD-actin binding mechanism. It shows that upon actin binding, FLNa residues immediately N-terminal to the CH1 domain become ordered and contribute to actin binding. By identifying three actin-binding sites (ABS-N, ABS2' and ABS2) we resolve controversy surrounding the specific sites involved in actin binding. We find that ABS-N participates in hydrophobic and cation-π interactions with subdomain 1 of actin while ABS2' binds an adjacent actin subunit. The previously mapped ABS2 also makes key ionic and hydrophobic interactions. The functional importance of each of these sites was validated using structure-guided mutations. My structure also indicates CH2 domain movement associated with actin-binding, establishing that, as previously proposed based on earlier lower-resolution structures, binding involves ABD opening and does not involve direct CH2-actin interactions. In addition to avoiding steric clashes of the CH2 domain with actin, ABD opening exposes the highly-conserved actin-binding residue W142 in ABS2 which, in the closed conformation, binds the CH2 domain, serving as a regulatory latch to stabilize the closed ABD. Finally, combining cellular and biochemical analysis of disease-associated FLNaABD mutations with our structural studies helps explain the localization of PVNH disease-associated loss-of-function point mutations to the actin-binding CH1 domain and gain-of-function OPDSD mutations to the regulatory CH2 domain.

The N-terminal flanking regions of ABDs are diverse in length and sequence, but the ABS-N sequence is conserved in filamins and α-actinins and, despite relatively low sequence similarity with the FLNa N-terminus, deletion of residues 1-27 in utrophin ABD or 1-51 in β-III-spectrin ABD

has been shown to dramatically reduce actin binding (91, 101). Thus, residues N-terminal to CH1 have functionally conserved biological significance in multiple ABDs.

Notably, at least in the case of FLNa, residues preceding ABS-N are not necessary for actin binding as N-terminal truncations (Δ1-27 and Δ1-32) did not diminish ABD co-localization with actin filaments. Consistent with this, an alternate FLNa transcript that results in initiation at M28 (equivalent to our Δ1-27 ABD) produces functional FLNa protein that targets to actin (96). Furthermore, FLNb also has a relatively short N-terminus (equivalent to the Δ1-27 FLNaABD) and the FLNbABD binds actin filaments with affinities comparable to the FLNaABD (shown here and (107)). This suggests that the variability in sequence N-terminal to ABS-N may provide mechanisms to regulate ABD binding to actin. Indeed, calmodulin binding to N-terminal residues of plectin has been proposed to regulate plectin interactions with actin filaments(108, 109). Calmodulin has also been reported to inhibit FLNa binding to actin (110) but, rather than binding the N-terminal region, calmodulin was proposed to utilize a cryptic binding site (residues 87-96) in the FLNaCH1 domain that became exposed upon actin binding. We now show that the proposed calmodulin-binding site faces away from actin and we observe no substantial conformational changes in this site upon actin binding, making it unclear how calmodulin would selectively bind this region in the FLNaABD-actin filament complex to drive dissociation. Furthermore, despite the strong sequence and structural conservation between FLNa and FLNb, calmodulin did not inhibit FLNb binding to actin (107). The structural basis for any effect of calmodulin on FLNa binding to actin therefore remains to be determined.

FLNa binding to actin filaments is however clearly influenced by the CH2 domain and my structural data show that when bound to actin the FLNaABD domain adopts an “open” position distinct from the closed conformations seen in FLNaABD crystal structures (31, 32). However, even in the actin-bound FLNaABD E254K structure, the lower resolution of the CH2 domain

reveals that this domain is mobile and this presumably explains why it was not visible in most other ABD-actin complexes (88, 91). An open conformation is necessary to avoid steric clashes with actin and to expose the otherwise occupied actin binding residue W142 in ABS2. Notably, W142 plays alternative functional roles by either binding actin when the ABD is in an open conformation or binding CH2 in the closed unbound conformation. W142 is completely conserved across ABDs and has been implicated in latching α-actinin-4 (102) and plectin (111) closed, indicating that this switching mechanism may be conserved mechanism for controlling the conformational equilibrium of many, if not all, tandem CH ABDs.

The cellular and biochemical experiments performed by Daniel Iwamoto demonstrate loss-of-actin binding with most of the human PVNH mutations that localize to FLNaCH1. While some appear to disrupt direct molecular interactions with actin (M102V, V122G, K127N), others likely elicit their effects by deforming actin-binding sites or the CH1 domain in general (A39G, I119D, A128V). Conversely, we propose that the FLNaABD exists in a conformational equilibrium in solution and that the gain-of-function OPDSD mutations in the CH2 domain exert their effects by shifting that equilibrium towards open states. The decreased melting temperature and increased affinity of FLNaABD-E254K and -Q170P for actin filaments (shown here and (32)) are consistent with this model but solution dynamics experiments, as recently applied to the β-III-spectrin ABD (91), will be required to test it further. Notably, the FLNaABD is apparently also dynamic even when bound to actin filaments, and this motility presumably accounts for the lower resolution (or lack of resolution) of the CH2 domain in actin-bound structures (88, 91), and suggests that there may be many “open” conformations compatible with actin binding.

In conclusion, our work resolves historical controversies in mapping the actin-binding sites of tandem CH domains and provides structural and functional insight into the ramifications of FLNa disease mutations.

Methods

Molecular biology, cell culture, protein purification, actin filament targeting assays, actin co-sedimentation assays, and differential scanning fluorimetry experiments were performed by our Daniel Iwamoto from the Calderwood laboratory at Yale University. For protocols, see 'Materials and Methods' as described in Iwamoto *et. al.* (26).

Cryo-Electron Microscopy Sample Preparation and Data Collection

Purified 6xHis-FLNaABD-WT, -Q170P, or -E254K were incubated at 60 µM with 15 µM phalloidin-stabilized actin filaments in a low salt co-sedimentation assay buffer at least 30 minutes before freezing. The Q170P and E254K samples were diluted 1:1 in H_2O immediately prior to freezing. Samples were prepared using holey carbon grids (Quantifoil R1.2/1.3 Micro Tools GmbH, Grosslöbichau, Germany) and a manual plunger device. Micrographs data sets were collected on a 200-kV FEI Tecnai F20 electron microscope equipped with a Gatan K2 Summit direct electron-counting camera at a pixel size of 1.247 Å. Micrographs were recorded in 0.3 second sub-frames over 7.2-10.2 seconds for a total dose of 47-60 $e^-/Å^2$ over a nominal defocus range of 1.1–2.7 µm. Later, a separate data set on the E254K sample was collected on a 300-kV Titan Krios microscope equipped with an energy filter and a Gatan K2 Summit camera in super-resolution mode at a physical pixel size of 1.33 Å. Micrographs were recorded in 0.25 second sub-frames over 12 seconds for a total dose of 50 $e^-/Å^2$ over a nominal defocus range of 1.0–2.9 µm.

3D Refinement

Micrographs were aligned and dose-corrected using MotionCor2 (64), where sub-frame motion correction (3x3 array) was applied to the wt and Tecnai F20 E254K data sets, while the Krios E254K data set was binned by 2. The Krios E254K data set was corrected for magnification distortion using parameters estimated by mag_distortion_estimate (112). Contrast transfer function parameters were calculated using Gctf (113), and micrographs where Gctf did not

detect signal at resolutions better than <4 Å were excluded from structural refinement for the Krios E254K data set. Filaments were manually selected using *e2helixboxer* from the EMAN software package (69) and extracted at a spacing of ~27.5 Å. The WT, Q170P, and E254K data sets collected on the Tecnai F20 used a box size of 390 pixels, while the Krios E254K data set used a box size of 210 pixels. Structure refinement was performed using IHRSR single-particle helical processing (45, 46) as implemented in RELION (version 2.0.3) (47, 48). The first round of refinement employed masks generated from earlier refinements that were low-pass filtered to 60 Å and included 10-20 Å soft edges using the *relion_mask_create* tool. The Tecnai F20 E254K and Q170P data sets were further processed in a second round of refinement using a mask generated from the 7 central actin subunits and CH1 domains that were low-pass filtered to 60 Å and included 15 Å soft edges. The Krios E254K data set was also improved in a second round of refinement using a helical mask generated from the results of the first round of refinement but constrained to the central 30% Z-slice, low-pass filtered to 60 Å, and included 6.5 Å soft edges. The WT data was subjected to a particle subtraction and masked 3D classification approach described elsewhere (44) to determine occupancy at the single subunit level. The decorated class (~33% particles) was then restored to its unsubtracted state and further refined using the same mask as earlier in the first round of refinement.

The resolution and B-factor of the final maps were calculated from the FSC correlation of independent half-maps in postprocessing with RELION following gold standard protocols. Symmetry was first imposed in real space on the independent half maps in the Tecnai F20 E254K (27.67 Å rise, -166.89° twist), Q170P (27.52 Å rise, -166.88˚ twist), and Krios E254K (27.54 Å rise, -166.73˚ twist) data sets using the *relion_helix_toolbox* command. The imposed helical parameters were derived from local searches of symmetry on the full map in RELION. The FSC calculations for the Tecnai F20 E254K and Q170P data sets used a mask generated from earlier

refinements that was thresholded to contain only actin subunits and CH1 domains, low-pass filtered to 20 Å, and included 15 Å soft edges. The resolution of the Tecnai F20 E254K map reach 7.4 Å, while the Q170P map reached 6.6 Å. The symmetrized Krios E254K volume was used to generate a mask that included only actin and the CH1 domains, was low-pass filtered to 15 Å, and included 8 Å soft edges. This mask was next used in postprocessing calculations, where the final Krios E254K map reached a resolution of 3.6 Å. The final symmetrized Krios E254K map is low-pass filtered to 3.6 Å and sharpened with a B-factor of -150. The FSC calculations for the WT data set used the same mask from its structural refinement, and reached a resolution of 9.8 Å.

Model Building, Refinement, and Validation

PDB models of phalloidin-stabilized F-actin (PDB ID 6C1D, chain B, residues 1-375) (34) and FLNa CH1 (PDB ID 3HOC, chain A, residues 39-153) (32) were first fit as rigid bodies into the final symmetrized Krios E254K map using UCSF Chimera (68). This model was refined against the final map in Phenix (74) using real space refinement with simulated annealing. Next, the model was refined by manual adjustments and all molecule real-space refinement with Ramachandran restraints in Coot (75) and real-space refinement in Phenix without simulated annealing. After several iterations, additional N-terminal FLNa residues were built by the N-terminal addition of residues into the cryo-EM density in Coot and followed by real-space refinement in Phenix. Multiple subunits and phalloidin subunits (PDB ID 6C1D) were loaded into the neighboring densities and evaluated in MolProbity (76) for steric clashes, which were manually fixed in Coot. Next, structural data for phalloidin (ChEBI ID 8040) (114) was used to generate geometric restraints in eLBOW (115) for real-space refinement with the final map in phenix. The refined phalloidin chains were combined with the model. The final model was evaluated by MolProbity. Cation-π interactions were investigated using the CaPTURE program (116). Structural figures were generated in ChimeraX (117).

Chapter III. High-resolution cryo-EM structures of actin-bound myosin states reveal the mechanism of myosin force sensing

Introduction

The myosin family of cytoskeletal motors performs diverse biological and mechanical functions, ranging from muscle contraction to intracellular motility (118). This versatility relies on the ability of myosin motors to adjust their power outputs in response to mechanical load in an isoform-dependent manner. However, the structural mechanism of this behavior is unknown (119).

Myosins generate force via the rotation of their lever arms in response to actin binding and phosphate release (120). Following these steps, a second rotation of the lever is a force-sensitive conformational transition that affects the rate of ADP release, which is often the step that limits that rate of motility (35, 121-124). ADP release is thus an important mechanical control point affecting power output, and is a source of the substantial kinetic diversity among myosin isoforms (119). Recent progress revealed subdomain motions within actin-bound myosin that accompany ADP release (125), but the mechanisms by which these changes are connected to the active-site have not been resolved.

Here, I describe the results of a collaboration (34) with the Ostap and Shuman laboratories at the University of Pennsylvania. In this project I prepared actomyosin samples provided by the Ostap laboratory for cryo-EM experiments, collected several data sets, and refined and classified the resulting structures. Ahmet Mentes, a postdoc in the Ostap laboratory, refined atomic models of the cryo-EM maps, and the Ostap and Shuman groups spearheaded model interpretation. Together, we report high-resolution structures of actin-bound myosin-IB (myo1b), a motor characterized by its high force-sensitivity (35). The structures reveal an allosteric linkage between MgADP release from the myosin active site and the lever arm

rotation during the force-sensitive transition. Additionally, we provide the high-resolution structure of the actin binding interface of myo1b, finding that, despite the conserved spatial topology of actin-binding loops, the precise nature of actin binding among myosins is quite diverse. Finally, we provide the first high-resolution structure of phalloidin bound to actin.

Results and Discussion

Cryo-EM of Actomyosin

I generated complexes of actin filaments decorated with a myo1b construct containing a single IQ motif with calmodulin bound, and solved near-atomic resolution structures both in the absence (rigor) and presence of 1 mM MgADP. The resolution for the motor domain was calculated as 3.3 Å for the ADP-bound state (AM.ADP^{A}) and 3.9 Å for the rigor state (AM) allowing us to trace the protein chains throughout most of the map, discriminate side chains in the best regions, visualize the MgADP, and determine the structure of actin-bound phalloidin (see below). The resolution of the lever arm was poorer in all maps, so to preserve the high resolution of the actin filament and the motor without over-refining the lever arm, we generated hybrid maps (Fig. 19).

Consistent with previous EM and single-molecule studies (35, 121, 122, 126), the structures reveal a rotation in the lever arm resulting in two well-defined end states, AM.ADP^{A} and AM (Fig. 20). Following the initial refinement, I used 3D classification to search for alternate conformations and found a second ADP-bound population, termed AM.ADP^{B} and comprising ~15% of the total population (Fig. 20). While densities for ADP and associated Mg^{2+} cation are seen in the AM.ADP^{B} map (Fig. 20), the lever rotates ~21° toward the barbed-end of the actin filament compared to the AM.ADP^{A} state and assumes a position similar but not identical to that of the AM state (Fig. 20A , 21A). The three conformational states thus appear to give a mechanistic succession of states proceeding from ADP^{A} to ADP^{B} to AM.

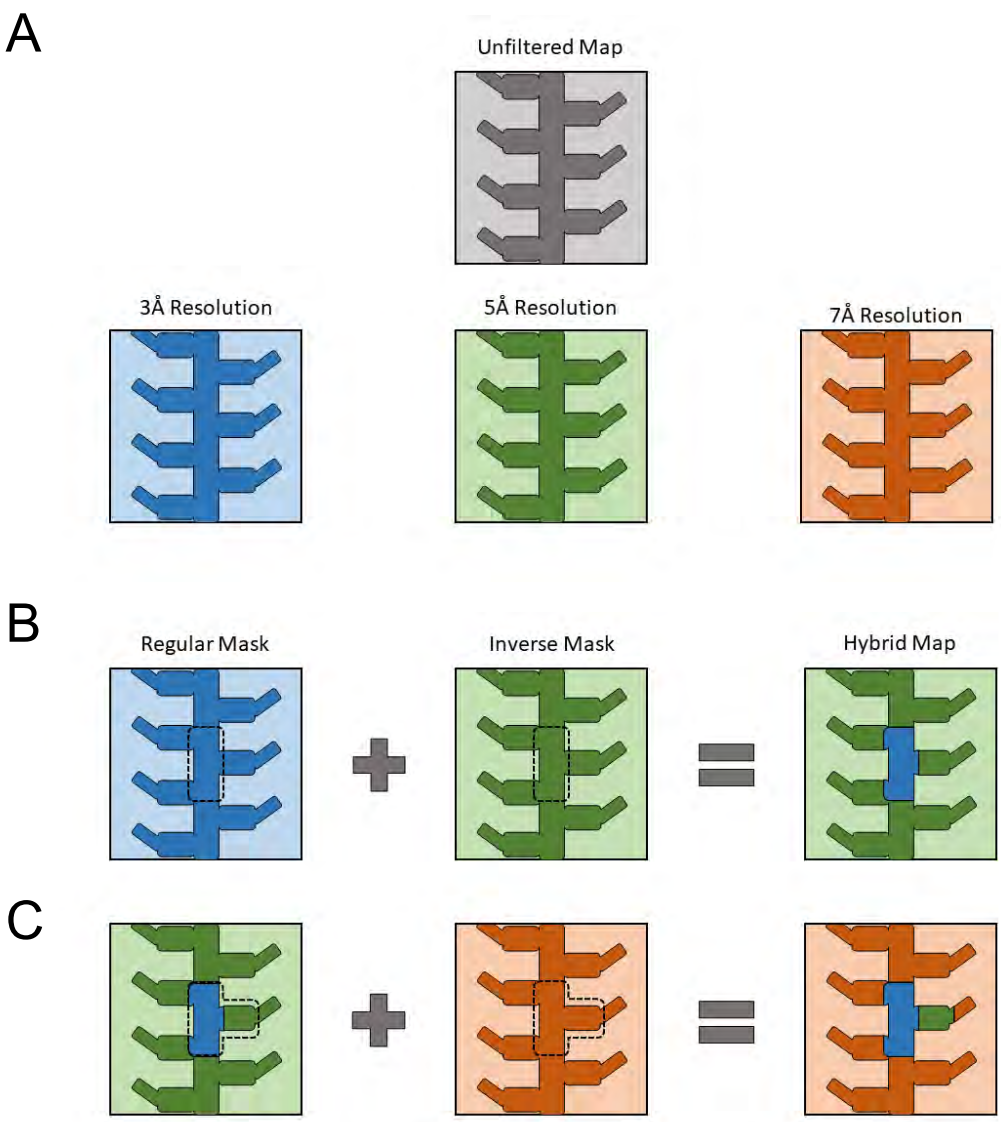

Figure 42. Hybrid map construction. (A) Hybrid maps are generated by filtering a reconstructed volume to different resolutions. In this example, an original map (grey) is filtered to 3Å, 5Å, and 7Å resolution (blue, green, orange). (B) Next, a map is applied to one of these filtered maps as normal, while the inverse of the same mask is applied to a different filtered map. These masked maps are then added together to generate a hybrid map. (C) Next, the resulting hybrid map can be used in additional rounds of map hybridization to generate complex hybrid maps.

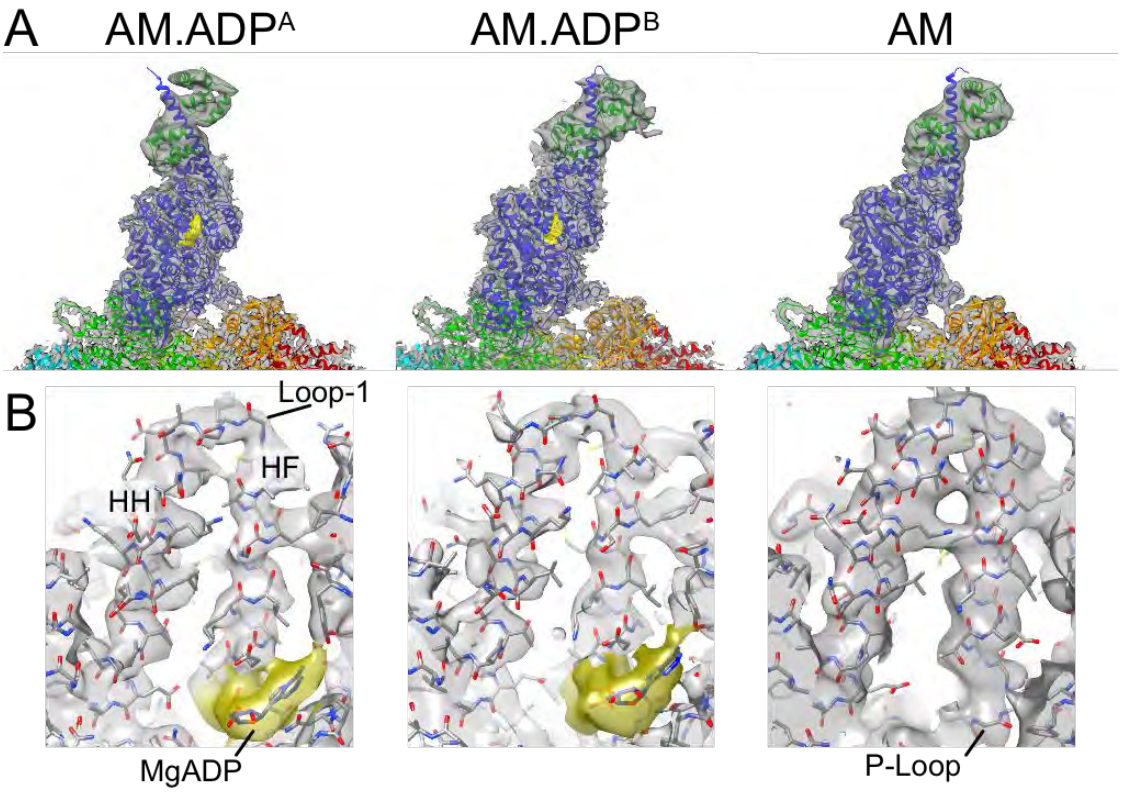

Figure 43. Structural states of actin-bound Myo1b in the presence and absence of MgADP. (A) Cryo-EM density maps (grey) and final fitted AM.ADP^{A}, AM.ADP^{B} and AM models. The (blue) Myo1b protein construct with a single IQ motif and bound (dark green) calmodulin are bound to (cyan, green, light green, orange, red) actin subunits. Cryo-EM Density for MgADP is highlighted in gold. (B) Cryo-EM density map showing the nucleotide binding site. The (gold) MgADP is bound to the P-loop and framed by the HF and HH helices, which are connected by loop-1.

Connection between MgADP Release and Lever Rotation

A comparison of the AM.ADP^{A} and AM structures reveals details of the pathway that couples MgADP release with a lever arm swing (Fig. 20), which is distinct from the pathway that drives the power stroke that is linked to closing of the actin-binding cleft, phosphate release, and movement of the SH1, SH2, and relay helices (120, 127). Using DynDom (128), our collaborators identified myosin subdomains (motor, lever, N-terminal subdomain) that rotate and translate semi-independently about hinge axes and bending residues (Fig. 21, Table 1). During this transition, the N-terminal subdomain (blue) pivots to open the nucleotide cleft, moving ~4 Å away from the upper 50 KD region of the motor (Fig. 21B). This rotation of the N-terminal subdomain was also observed in the 8-Å cryo-EM structure of myosin-V (125). Opening of the nucleotide cleft involves substantial axial and lateral shifts of the P-loop and adjoining helix (HF; K114-V128) in the N-terminal subdomain, relative to the HH helix (A133-F152; connected to HF via loop-1). The lever position in AM.ADP^{A} is accompanied by unwinding of the C-terminus of the relay helix relative to AM by 24°, resulting in a break in the alpha-helical hydrogen-bonds. This disruption in the helix is not present in AM.ADP^{B} and AM, and it is in the position of the relay helix that kinks in the pre-power-stroke state of myosin (127, 129, 130).

The quality of the AM.ADP^{A} and AM density maps is sufficiently high to visualize the density of some key side chains that directly and indirectly interact with MgADP (Fig. 22). Nucleotide cleft opening and MgADP release disrupts a conserved hydrogen-bonding pair, T115-D387, that coordinates Mg in most nucleotide-bound structures of myosin. These changes are accompanied by the formation of a salt bridge between K114 (P-loop) and D387 (which precedes switch-2) and the loss of coordination of the MgADP phosphates by K114. Consequently, the network of interactions holding the HH-helix and switch-1 to the HF helix and P-loop is lost, facilitating repositioning of the N-terminal subdomain.

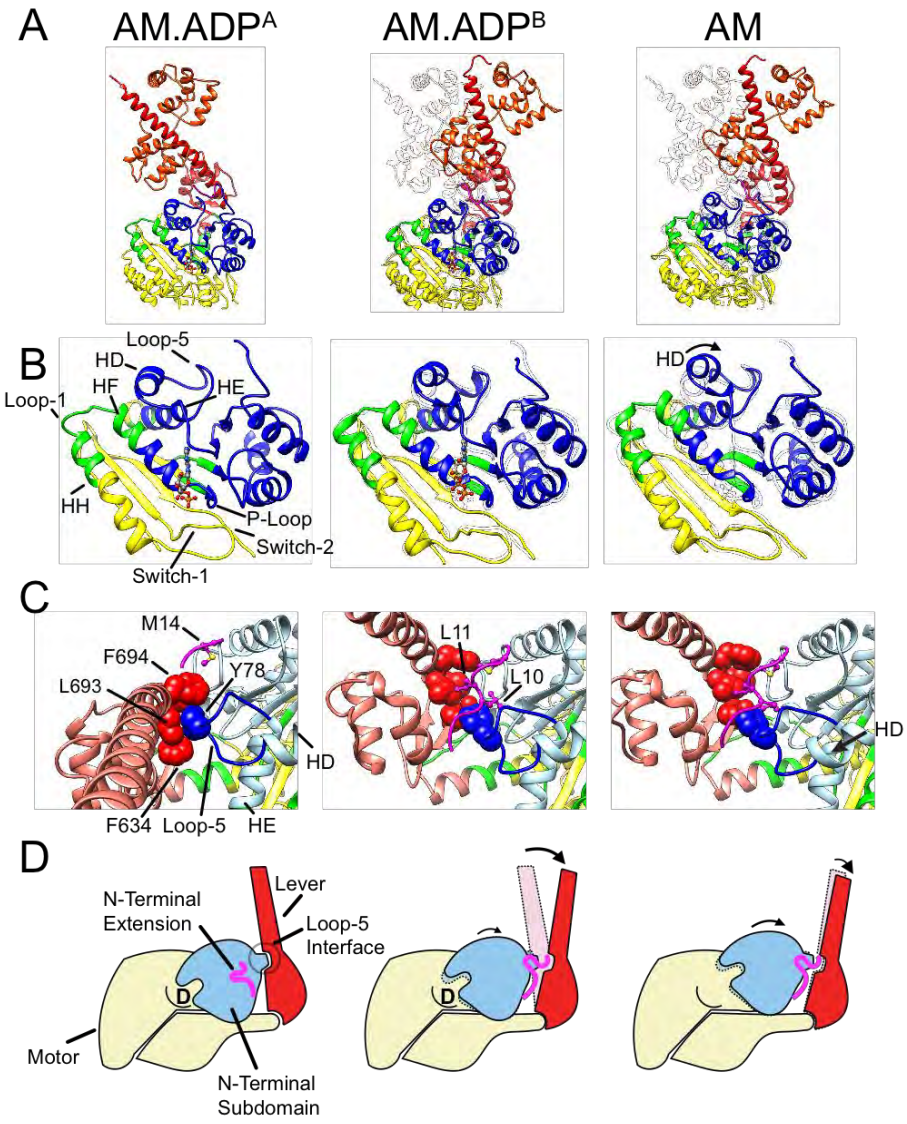

Figure 44. Coupling of nucleotide-dependent changes at the active site to lever rotation. (A) Structural models showing changes in the myo1b active site and lever position. Coloring of subdomains is as defined by DynDom: (yellow) motor; (blue) N-terminal subdomain, which includes sequences in the N- and C- termini and the transducer; (red), lever, which includes the converter domain and bound calmodulin. The (magenta) N-terminal extension is docked and resolved in the density maps for AM.ADP^{B} and AM structures, but not AM.ADP^{A}**.** Structural models are aligned by aligning bound actin subunits. (B) Enlarged region showing the nucleotide binding site and conformational rearrangements in the N-terminal subdomain. Coloring and orientation are identical to (A). AMDP^{A} structure is shown as an outline in the AM.ADP^{B} and AM panels of (A) and (B). (C) Interaction of (dark blue) loop-5 in the (light blue) N-terminal subdomain with the (red) lever and (magenta) N-terminal extension. The side chains in loop-5 are not resolved in the Cryo-EM density and were placed based on MD. (D) Cartoon model showing the conformational changes in the structural subdomains that accompany lever rotation.

Table 1: Rotations, translations and bending/hinge residues of moving domains relative to a fixed domain defined by DynDom from AM.ADP^{A} to AM state.

Fixed Domain	Moving Domain	Rotation Angle (in degrees)	Translation (Å)	Bending Residues	Hinge Residues
N-term (blue)	Lever (red)	21	1.5	629 - 633	No mechanical hinges
N-term (blue)	Motor (yellow)	9.2	0.84	94-95, 106-107, 123-141, 590-594	P590, N591, I592, I593, R594
Lever (red)	Motor (yellow)	24	0.43	419-423, 433-440	L420 , K421, T435, Y439

N-Terminal Subdomain (Nterm) includes residues: 12-94,107-129,591-591,594-629
Lever includes residues: 420-433,630-734
Motor includes residues: 95-106,141-419,440-590,592-593

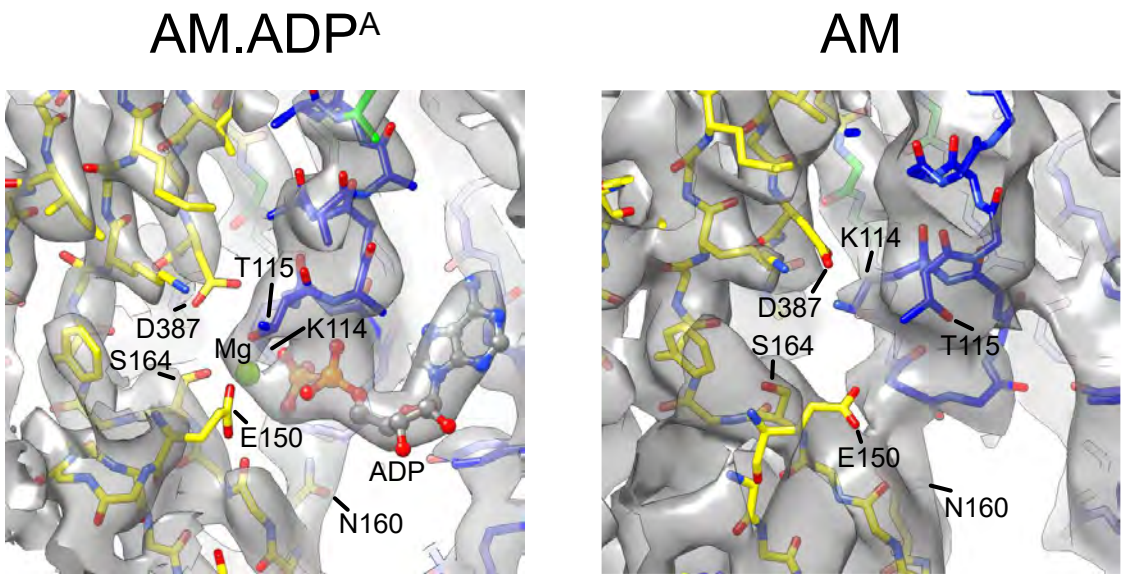

Figure 45. MgADP-induced conformational changes at the active site. Nucleotide binding site of myo1b in the (left) AM.ADP^{A} and (right) AM states showing sidechains that interact directly or indirectly with MgADP. Cryo-EM density for the E150 side chain is not resolved, but is included as a nucleotide-interacting residue based on MD results. Coloring is as in Fig. 21.

MgADP Changes the Interface Between the Lever, N-Terminal Subdomain, and the N-Terminal Extension

We identified a novel interface between the AM.ADP^{A} lever and a region within the N-terminal subdomain which we named loop-5 (Y72 - H83), located between the HD (P66 - D71) and HE helices (I84-Q98) (131) (Fig. 21B,C). Residue Y78 in loop-5, conserved in the myosin I family, is nestled within a cluster of hydrophobic side chains from the converter and the base of the lever to stabilize the lever position (Fig. 21C). As the N-terminal subdomain rotates towards the lever in AM, Y78 is pulled out of its position in the lever cavity and occludes the AM.ADP^{A} position of the lever via steric clashes between Y78 and L693 of the lever. Consistent with this observation, multiple rounds of structural classification of the AM cryo-EM data set failed to yield evidence that the lever can assume the AM.ADP^{A}-like orientation. These observations indicate that the ADP-like position of the lever and opening of the nucleotide cleft (in order to release ADP) are mutually exclusive.

Accompanying the lever swing, a structural element, which we call the N-terminal extension (residues V6 - I15), becomes sandwiched between the motor and lever in AM, contributing side chains L10 and L11 to the hydrophobic cluster of residues (Fig. 21C, 23) as found in the apo crystal structure (131). The binding site of the N-terminal extension is sterically occluded in AM.ADP^{A}, and residues preceding L11 are unresolved. The N-terminal extension of myo1b is important for activation of ADP release, as its deletion slows the rate of ADP release 10-fold, while the force dependence of the step is unchanged (131). However, changing the sequence of this region impacts myosin-I force sensing (132). Therefore, docking of the N-terminal extension likely facilitates the movement of the N-terminal subdomain to the AM position and opening of the nucleotide-binding site, allowing for ADP release.

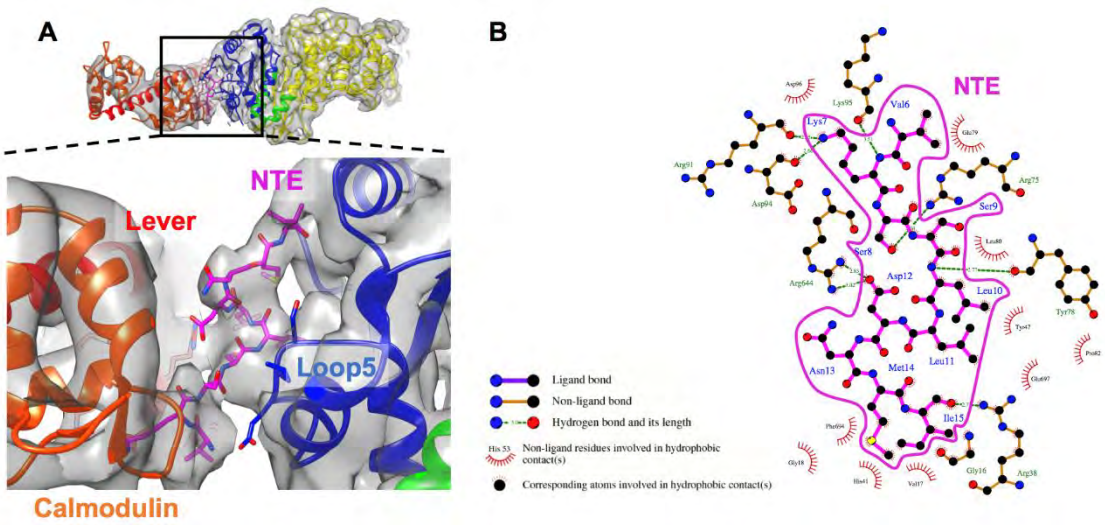

Figure 46. Conformation of the N-terminal extension. (A) The N-terminal extension (6-15) in AM state shown with cryo-EM density map. The N-terminal extension residue side-chains and side-chains of surrounding residues of Loop-5 (blue) and lever (red) are shown with stick representation. (B) The interaction of N-terminal extension (NTE) with surrounding residues in a two-dimensional interaction map prepared with LigPlot (133). The sidechain interaction map was created using the apo-Myo1b crystal structure (PDB: 4L79) and is consistent with the lower resolution cryo-EM map.

The AM.ADP^{B} structure represents an intermediate state in which the lever swing is nearly finalized, but is incompletely coupled to opening of the nucleotide cleft. The lower resolution of the AM.ADP^{B} state does not allow the same precision of modeling as the other two structures, but the interface created by the lever, the N-terminal subdomain, and the N-terminal extension is clearly similar to AM (Fig. 21C). However, the N-terminal subdomain in AM.ADP^{B} rotates only halfway (4°) toward the AM position (9° total rotation). Consequently, the AM.ADP^{B} nucleotide binding site remains mostly closed, except for a ~1.5 Å axial shift of helix HF and the adjoining P-loop compared with AM.ADP^{A} (Fig. 21). The similarity of the AM.ADP^{B} nucleotide cleft to AM.ADP^{A} suggests a similar coordination of the nucleotide in both states. Upon the transition from AM.ADP^{B} to AM, the additional rotation of the N-terminal subdomain results in the oblique rotation of the lever due to these elements being linked to each other by the N-terminal

extension sandwich configuration (Fig. 24). These observations indicate that the structure of the ADP-occupied active site is not tightly coupled to the position of the lever, in contrast to previous suggestions (125).

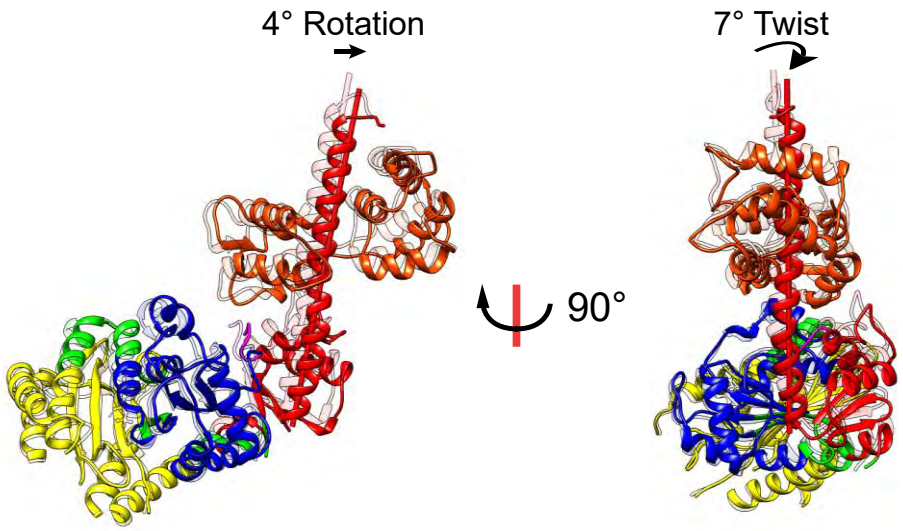

Figure 47. Movement of the N-terminal subdomain results in the oblique rotation of the lever as it transitions from AM.ADP^{B} (transparent color) to AM (solid color) state. N-terminal subdomain (blue), lever (red) and calmodulin (orange-red). The lever arm rotates 4 degrees and twists 7 degrees from AM.ADP^{B} to AM.

Mechanism of Myosin Force Sensing

As a mechanism for force sensing, we propose that mechanical loads that prevent the rotation of the myosin lever toward the AM position block the translation and rotation of the N-terminal subdomain required for breaking the network of interactions that hold MgADP in place. This inhibition is not only due to the steric blocking of the N-terminal subdomain rotation, but is also due to interactions between the lever and N-terminal subdomain that stabilize the AM.ADP^{A} state (Fig. 21C,D), holding the P-loop, HF and HH helices, and switch-1 in a position to

coordinate the MgADP. It is likely that all myosin isoforms require the rotation of the N-terminal subdomain to release MgADP, but different isoforms have structural modifications that differentially link N-terminal subdomain rotation to the magnitude of lever rotation. These modifications may include the variable angular positions of the lever, as in myo1b and myosin-V (125), as well as the sequence of an N-terminal extension that interacts with the N-terminal subdomain, as found in myosin-I (131, 132) and myosin-II (134). We propose that myosins in which the N-terminal subdomain is able to rotate without requiring a large amplitude rotation of the lever, or lack stabilizing interactions between the lever and the N-terminal subdomain, are less force dependent than those that have N-terminal subdomain rotations linked to large lever rotations.

The Actin-Binding Site of Myosin is Structurally Diverse

The myo1b actin-binding site is well resolved and is nearly identical in the AM.ADP^{A} and AM states. Thus, myo1b binding to actin during ADP release, as found for myosin-V (125), holds fixed the geometric relationship between the upper and lower 50kD domains helping orchestrate the above-described coupling pathway between the nucleotide pocket and the lever, in particular by constraining the relative position of the lever and the N-terminal subdomain.

Like myosins-II and –V (125, 135), a helix-loop-helix motif (L457 - T485) in the lower 50 KD region of myosin fits in a hydrophobic pocket between two actin subunits, which includes a well-ordered DNase I binding loop (D-loop) of actin (Fig. 25). Modeling within this region shows interactions between myosin E477 and the side-chain of actin K50, myosin Q481 side-chain oxygen with the backbone hydrogen of actin G48, and myosin E462 with S350 and T351 in actin. Finally, the backbone of myosin G468 hydrogen bonds with actin G146. Also within the lower 50KDa region, residues within the myosin activation-loop (N452 and T453) interact with S350 of

actin, but density for an interaction with the actin N-terminus as predicted for myosin-II (135) and observed for myosin-V (125) was not resolved.

Although the spatial topology of the CM-loop and loops-2, -3, and -4 is also conserved in all myosins, our myo1b structures show that the precise nature of actin binding among myosins is quite diverse (Fig. 26), as described more fully in the published paper(34).

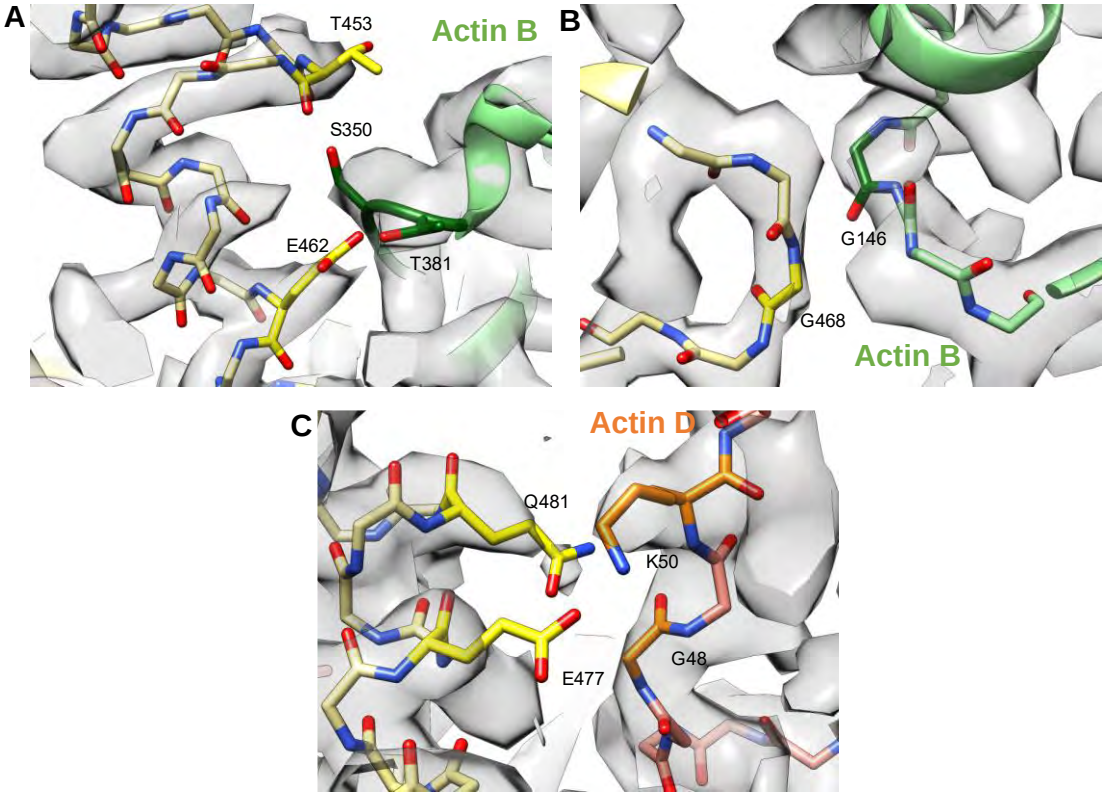

actin subunits. (A) Interaction of myosin E462 with S350 and T351 in actin (subunit B-green) and the myosin activation-loop T453 interaction with S350 of actin. (B**)** Interaction of myosin G468 with actin G146 (subunit B-green). (C) Interactions between myosin E477 and the side-chain of actin K50 (subunit D-orange); myosin Q481 side-chain oxygen with the backbone hydrogen of actin G48 (subunit D-orange).

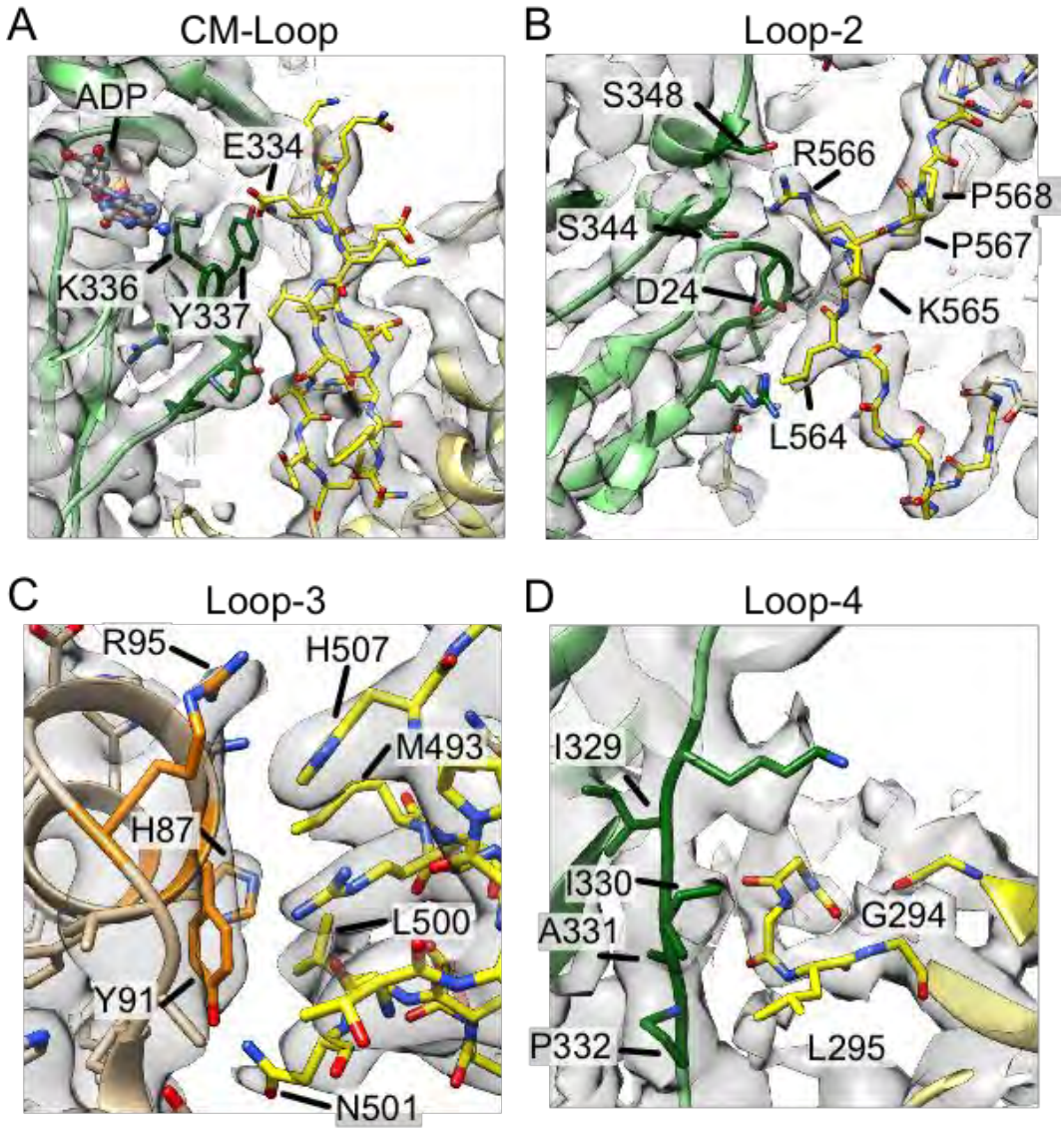

Figure 49. Myo1b has a unique actin-binding interface. (Grey) Cryo-EM densities and structural models of (yellow) myo1b loops binding to actin. The relationship of actin subunits in the filament to the myosin binding site is shown by the actin coloring (green and orange) in Fig. 1A. Actin residues that interact with myosin are shown in darker colors. (A) CM-loop binding to actin. E334 is the TEDS site that interacts with K336 and Y337. The actin-bound ADP molecule is shown and interacts with E334 through K336. (B) Loop-2 binding to (green) actin. (C) Loop-3 becomes ordered upon actin binding and interacts through a group of hydrophobic interactions clustered around Y91. (D) Loop-4 interacts with (green) actin via a network of hydrophobic interactions. The cryo-EM map is less resolved than above, suggesting a weaker interaction.

High-Resolution Structure of Actin-Bound Phalloidin

The cryo-EM data sets contain regions of excess density at the interface of three actin monomers. We assume these densities represent phalloidin, the bicyclic heptapeptide (cyclic(L-Ala1-D-Thr2-L-Cys3-*cis*-4-hydroxy-Pro4-L-Ala5-2-mercapto-L-Trp6-4,5-dihydroxy-L-Leu7) cyclic (3->6) sulfide), which was used to stabilized the actin filaments.

The position and orientation of phalloidin was near that predicted from X-ray fiber diffraction (136, 137) and negative stained EM of gold labeled phalloidin (138) with the dihydroxyleucine7 facing the outside of the filament. The phalloidin-actin interactions predicted from the fit are shown in the atomic model (Fig. 27A) and the schematic determined by LigPlot (Fig. 27B) (133). The phalloidin interactions primarily couple adjacent actin monomers of the one-start short pitch helix (actin C and actin D) or equivalently laterally (transversely) between strands of the two-start long pitch helices. The additional predicted axial (longitudinal) coupling is the hydrophobic interaction of I287 of actin B with actin D through phalloidin. The lateral contacts of native filaments are composed of a small number of electrostatic interactions which are expected to be comparatively weak (139, 140). On the other hand, the phalloidin coupled lateral interactions are composed of extensive hydrophobic contacts and five additional hydrogen bonds which are expected to be strong. The Van der Waals surfaces of phalloidin and its binding site suggests that Trp6 provides a large measure of its binding strength while the remainder of the molecule provide its specificity. Interestingly, the pocket in which Trp6 binds is a major site of jasplakinolide binding (141). Our results are consistent with mutational analysis of Drubin et al. (1993) that predicted the importance of R177 and D179 as phalloidin binding residues (142).

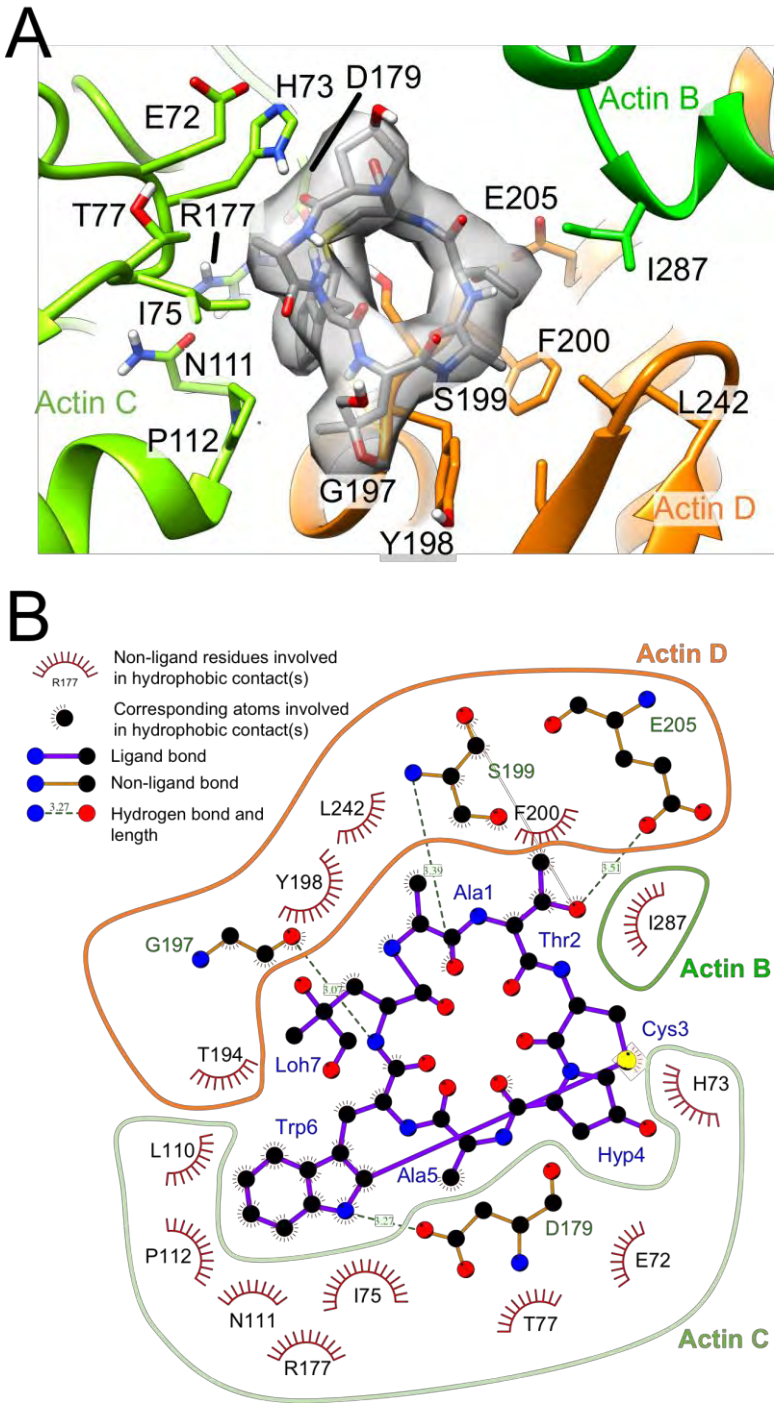

Figure 50. Phalloidin structure and actin-binding site. (A) The phalloidin model (grey) in cryo-EM density and its interactions with residues in three actin subunits, Actin B (green), C (light green) and D (orange). The pointed end of the filament is at the top and barbed end at the bottom of the figure. (**B)** Two-dimensional interaction map of phalloidin with actin subunits as calculated using Ligplot (133). Actin and phalloidin residues are denoted by 1- or 3-letter amino acid abbreviations, respectively. Phalloidin contains dihydroxy-L-Leucine (Loh7) and 4-hydroxy-Proline (Hyp4) amino acids.

Methods

Myo1b.Li_2SO_4 crystallization and structure determination, molecular dynamics flexible fitting (MDFF) and MD simulations, the definition of domain movements by DynDom, and manual editing of phalloidin structure were performed by our collaborators in the Ostap and Shuman laboratories, and details can be found within the online 'SI Materials and Methods' section of Mentes *et. al*. (34).

Cryo-EM Sample Preparation

Actin, calmodulin, and myosin-Ib (myo1b) containing the motor domain and the IQ motif of the lever arm helix with bound calmodulin, containing a C-terminal AviTag and FLAG tag, were expressed and purified by our collaborators as described (131, 143, 144). Fresh samples of F-actin and frozen aliquots of myo1b and calmodulin were prepared at the University of Pennsylvania and shipped to Yale University. The myo1b and calmodulin samples were thawed and centrifuged prior to sample preparation. F-actin with excess myo1b and calmodulin were briefly mixed and incubated before centrifugation at approximately 350,000g for 15 minutes at 4˚C. The resulting pellet was resuspended in a buffer containing 10 mM KCl, 10 mM MOPS pH 7, 1 mM $MgCl_2$, 1 mM EGTA, 1 mM DTT, and 1 µM calmodulin (KMg10 with calmodulin). The ADP sample resuspension buffer also included 1 mM K_2ADP and an additional 1 mM $MgCl_2$. Samples were plunge-frozen on carbon grids (Quantifoil R1.2/1.3) using a manual plunger device. The grids for the ADP samples were lightly glow discharged (10 seconds, 15 mA), while no glow discharge was used for the rigor samples. Samples were mixed with concentrated myo1b or resuspension buffer to optimize filament density and improve decoration based on the appearance of test grids analyzed on Yale University's 200kV FEI-F20 electron microscope. The final ADP sample included approximately 6 µM F-actin, 14 µM myo1b, and 0.75 mM MgADP

in KMg10 with calmodulin. The final rigor sample included approximately 7.5 µM F-actin and 17 µM myo1b in KMg10 with calmodulin.

Data Collection and Processing

Micrographs were collected at Purdue University's cryo-EM facility with a 300kV Titan Krios electron microscope equipped with a Gatan K2 Summit direct electron-counting camera. Automatic data collection was performed with Leginon (145). Micrographs were recorded with 55 subframes in 11 second exposures with a dose rate of approximately 4.7 e-/Å^2/sec over a defocus range of 0.8 to 2.8 µm. These images were collected in super-resolution mode with a pixel size of 0.65 Å. In total 660 micrographs were collected for the ADP sample, and 1050 micrographs were collected for the rigor sample.

Micrographs were binned by 2 during movie alignment and dose correction in MotionCor2 (64). Relatively higher filament density in the ADP data set enabled sub-frame motion correction (3 by 3 patches). CTF parameters were calculated using Gctf (146). Particles were manually picked using e2helixboxer from EMAN2 (69) and structure refinement was performed in RELION with helical processing (47, 48) using a box size of 520 Å. 76,000 particles were selected from 280 micrographs in the ADP data set and 96,000 particles from 860 micrographs in the rigor data set. A 'full-particle' 3D soft mask, generated from an initial 3D reconstruction by the 'relion_mask_create' tool, was applied after each cycle of refinement. This procedure yielded maps with a global resolution of 3.9 Å for the ADP state and 5.4 Å for the rigor state. 'Particle polishing' was applied to the rigor data set and the refinement was continued, although this step did not significantly affect the resolution of the map. Additional refinements were then performed using the 'unpolished' ADP data and the 'polished' rigor data, applying a smaller soft mask (generated from the three central actin and myo1b subunits) to the reference volume

after every cycle of refinement. Following this procedure, the global resolution reached 3.2 Å in the ADP sample and 4.1 Å in the rigor sample.

Particles were then sorted in 2 rounds of masked 3D classification in RELION. First, a low-pass filtered map of the central subunit of the filament were generated by fitting atomic models of actin and myo1b into each map, generating a 3D volume with pdb2mrc from the EMAN software suite (65), and then applying 'relion_mask_create'. The resulting 'central-subunit masks' were then subtracted from the full-particle soft masks utilized in the previous refinement steps, using the relion_image_handler tool. The resulting 'reverse' masks were applied to the refined 3D maps, and projections of the resulting volume were subtracted from the particle stacks to highlight the central actin and myo1b subunit. 3D classification was then performed on these 'subtracted' particle stacks, fixing the shift and orientation parameters obtained from the previous refinement. The ADP state 3D classification was performed with 10 classes, yielding a dominant occupied class (corresponding to actomyosin) with 70% of particles (53,000) and an unoccupied class (corresponding to bare actin) with 25% of particles (19,000). The remaining 5% of particles, which were dispersed among the remaining 8 classes, exhibited poorly resolved or artifactual density features and were discarded. The rigor state 3D classification was performed with 14 classes, yielding a single occupied class with 84.6% of the particles (80,000) and a single unoccupied class with 14.4% of the particles (14,000). The remaining 2% of particles (dispersed among the 12 other classes) were discarded. Particles corresponding to occupied classes were restored to the 'unsubtracted' state before initiating a new round of refinement, applying the 'full-particle' mask in the first cycle and continuing with a 3-subunit reference-volume mask as before. Following this classification procedure, the relative density of the central myosin subunit in the occupied class increased with respect to actin (reflecting increased occupancy), although there were no significant changes in resolution.

A second round of particle subtraction and 3D classification was then performed, utilizing the above procedure but substituting PDB models of the N-terminal subdomain, lever arm, and light chain in place of the complete central subunit, in order to further focus the classification on conformational changes within myosin. The ADP state 3D classification was performed with 7 classes (again with fixed orientation and shift parameters), yielding a primary class (class A) with 75% of particles (40,000) and a secondary class (class B) with 14.6% of particles (7700). The remaining 10% of particles, dispersed among the remaining 5 classes, exhibited poor resolution and/or weak density in the lever arm region (although consistent with the class 'A' orientation) and were discarded. The rigor state 3D classification was performed with 10 classes, yielding a class with 75.4% of the particles (60,000). The remaining 24.6% of particles were dispersed among the 9 other classes, which included between 5.4% and 0% of particles; these classes were poorly resolved and hence discarded. All 3D classification steps in both rounds used references that were low pass filtered to 60 Å, a regularization parameter of T=2, and a high-resolution limit of 6-8 Å. After refining these classes first with full-particle reference-volume masks and continuing with 3-subunit masks as before, the ADP state A class reached 3.3 Å, ADP state B reached 3.9 Å, and the rigor state reached 4.1 Å (all at FSC=0.5) as calculated by post-processing in RELION using 3-subunit soft masks (Fig. 19).

Separate soft masks for the 5 central actin subunits together and the different subdomains of the central myo1b subunit were generated in RELION. These masks were used to calculate the resolution and b-factor of these regions separately in post-processing with RELION. Hybrid maps were generated for MDFF calculations that included these regions filtered to their respective resolutions according to the FSC=0.5 criterion or FSC=0.143. Briefly, hybrid maps were generated by filtering the final map of a reconstruction to two different resolutions. A soft mask was applied to one of these filtered maps as normal, while the inverse mask was applied to the

other filtered map. These masked maps were then summed together. As the same mask was applied to each filtered map, the overall cryo-EM density remains consistent throughout the resulting hybrid map. This process was iterated to add multiple separately filtered regions to the hybrid map. Finally, a soft mask that included the central 5 actin subunits and the central myo1b subunits was applied as normal. These operations were performed in python.

Chapter IV: Conclusions and Future Directions

Cofilin

The results presented here demonstrate that the propagation of allosteric conformational changes from a cofilactin segment remain local to subunits in contact with cofilin, in agreement with nearest neighbor models of cooperative cofilin binding. Furthermore, these results explain why severing is more efficient at the pointed end boundaries, as cofilin only disrupts the D-loop of actin subunits to which it is bound, resulting in far more severe disruptions of the filament lattice at the pointed end of the filament. The comparison of my WT and S3D single bound cofilin structures also points to an important role for the N terminus of cofilin in promoting filament severing. Finally, my results also suggest that the minimal cluster size of two adjacent cofilin-decorated subunits is required to promote full cofilin binding cooperativity and maximal severing activity.

While I used the structure of single bound cofilin to make inferences about the pointed end of a full boundary (decorated on both strands), I have not yet resolved such a boundary to sufficient resolution for a detailed analysis, leaving open the possibility that it may behave differently. The lower frequency of large cluster pointed end boundaries in the data set resulted in a lower resolution reconstruction. Fortunately, with the collection of a larger data set I will be able to achieve results similar to the current barbed end boundary structure, as downsampling particles from the barbed boundary reconstruction generated a lower resolution structure comparable to the pointed end boundary. In addition, I would like to investigate the structure of a cluster with two adjacent cofilin-decorated subunits. This is challenging as according to our model full cofilin cooperativity should activate at this point, leaving few such particles in the data set as clusters rapidly grow. However, I may be able to increase the frequency with molecular biology techniques; if I generate a forced cofilin dimer by linking two subunits to each

other via fusion proteins on their C terminus, such as with the SpyTag/SpyCatcher (147) system, I may be able to increase the frequency of such clusters in the data set, although varying of the concentrations of dimers and actin will likely be required to achieve optimal results. This strategy could also help isolate the structures of lateral and longitudinal bound dimers by altering the length of the linker to the SpyTag/SpyCatcher system for more restrictive or permissive intersubunit distances.

Filamin A

I provided the first high resolution structure of actin-bound tandem CH domains, the actin-binding domains of crosslinking proteins. This structure enabled us to describe the key actin binding interfaces, all of which reside in the CH1 domain and includes a previously unidentified interface we termed ABS2'. The biological relevance of these interfaces was validated through biochemical assays performed by Daniel Iwamoto. My structure also confirmed the earlier 'open' and 'closed' hypothesis of ABD binding, where the low resolution CH2 domain is repositioned relative to X-ray crystal structures, which would otherwise clash with the actin filament. This structure enabled us to rationalize why loss-of-function missense mutations cluster in the CH1 domain while gain-of-function mutations cluster in the CH2 domain; since actin interactions occur with the CH1 domain, mutations here disrupt actin-binding, while mutations in the CH2 domain enhance actin binding because they promote the 'open' conformation of the ABD. Finally, we identified a key residue (W142) that may play an important role in mediating this self-regulation. Currently, I have no future plans for working with FLNa.

Myosin-IB

I resolved the first high resolution structure of a member of the myosin-I family, and my AM.ADP^{A} and AM structures remain the highest resolution myosin maps to date. I also identified an intermediate state (AM.ADP^{B}) for which no previous structural model existed. These

structures enabled us to propose a mechanism of myo1b tension sensitivity, where force sensitivity is conferred by both the tight coupling of the rotation of the N-term subdomain to the lever arm position as well as a large rotation of the N-terminal subdomain during the ADP to rigor transition. Myosins which lack tight coupling between the N-terminal subdomain and the lever arm or for which the N-terminal subdomain does not rotate significantly during this transition are likely force insensitive. These structures also revealed specific actin-binding interactions, which were diverse compared to other myosins, as well as the first high resolution structure of phalloidin bound to an actin filament.

The myosin superfamily remains an exciting area of research, as the diverse members of this family feature both specialized kinetics and structural features to accomplish their varied biological roles. I'm currently investigating the structures of *Drosophila* myosin-IC and myosin-ID as a part of a collaboration with the Ostap laboratory at the University of Pennsylvania. These myosins feature the extraordinary capability of inducing chirality in fly larvae when ectopically expressed at the cellular, tissue, organ, and organismal levels in opposing directions (148). This asymmetry could be significantly attenuated by swapping the neck domain from the opposing myosin, indicating that motor-neck coupling is important to inducing asymmetry. I am currently in the process of investigating the structural basis for this behavior by performing cryo-EM on both full-length myosin-IC and -ID.

Bibliography

1. V. Galkin *et al.*, Remodeling of actin filaments by ADF/cofilin proteins. *PNAS* **108**, 20568-20572 (2011).
2. T. D. Pollard, Actin and Actin-Binding Proteins. *Cold Spring Harb Perspect Biol* **8** (2016).
3. V. Galkin, A. Orlova, M. Vos, G. Schroder, E. Egelman, Near-atomic resolution for one state of F-actin. *Structure* **23**, 173-182 (2014).
4. X. C. Bai, G. McMullan, S. H. Scheres, How cryo-EM is revolutionizing structural biology. *Trends Biochem Sci* **40**, 49-57 (2015).
5. A. Huehn *et al.*, The actin filament twist changes abruptly at boundaries between bare and cofilin-decorated segments. *J Biol Chem* **293**, 5377-5383 (2018).
6. A. R. Huehn *et al.*, Structures of cofilin-induced structural changes reveal local and asymmetric perturbations of actin filaments. *Proc Natl Acad Sci U S A* **117**, 1478-1484 (2020).
7. G. Kanellos, M. C. Frame, Cellular functions of the ADF/cofilin family at a glance. *J Cell Sci* **129**, 3211-3218 (2016).
8. E. De La Cruz, How cofilin severs an actin filament. *Biophysical Reviews* **1**, 51-59 (2009).
9. E. De La Cruz, Cofilin binding to muscle and non-muscle actin filaments: Isoform-dependent cooperative interactions. *Journal of Molecular Biology* **346**, 557-564 (2005).
10. E. Andrianantoandro, T. Pollard, Mechanism of actin filament turnover by severing and nucleation at different concentrations of ADF/cofilin. *Molecular Cell* **24**, 13-23 (2006).
11. K. X. Ngo, N. Kodera, E. Katayama, T. Ando, T. Q. P. Uyeda, Cofilin-induced unidirectional cooperative conformational changes in actin filaments revealed by high-speed atomic force microscopy. *Elife* **4**, e04806 (2015).
12. W. Cao, J. Goodarzi, E. De La Cruz, Energetics and kinetics of cooperative cofilin-actin filament interactions. *Journal of Molecular Biology* **361**, 257-267 (2006).
13. I. V. Dedova, O. P. Nikolaeva, V. V. Mikhailova, C. G. dos Remedios, D. I. Levitsky, Two opposite effects of cofilin on the thermal unfolding of F-actin: a differential scanning calorimetric study. *Biophys Chem* **110**, 119-128 (2004).
14. E. De La Cruz, D. Sept, The kinetics of cooperative cofilin binding reveals two states of the cofilin-actin filament. *Biophysical Journal* **98**, 1893-1901 (2010).
15. E. Prochniewicz, N. Janson, D. Thomas, E. De La Cruz, Cofilin increases the torsional flexibility and dynamics of actin filaments. *Journal of Molecular Biology* **353**, 990-1000 (2005).
16. J. Pfaendtner, E. De La Cruz, G. Voth, Actin filament remodeling by actin depolymerization factor/cofilin. *PNAS* **107**, 7299-7304 (2010).
17. W. Elam, H. Kang, E. De La Cruz, Biophysics of actin filament severing by cofilin. *FEBS Letters* **587**, 1215-1219 (2013).
18. K. Hayakawa, S. Sakakibara, M. Sokabe, H. Tatsumi, Single-molecule imaging and kinetic analysis of cooperative cofilin-actin filament interactions. *Proceedings of the National Academy of Sciences of the United States of America* **111**, 9810-9815 (2014).
19. W. A. Elam *et al.*, Phosphomimetic S3D cofilin binds but only weakly severs actin filaments. *J Biol Chem* **292**, 19565-19579 (2017).
20. A. Bobkov *et al.*, Cooperative effects of cofilin (ADF) on actin structure suggest allosteric mechanism of cofilin function. *Journal of Molecular Biology* **356**, 325-334 (2006).
21. B. McCullough *et al.*, Cofilin-linked changes in actin filament flexibility promote severing. *Biophysical Journal* **101**, 151-159 (2011).

22. C. Suarez *et al.*, Cofilin tunes the nucleotide state of actin filaments and severs at bare and decorated segment boundaries. *Current Biology* **21**, 862-868 (2011).
23. H. Kang *et al.*, Site-specific cation release drives actin filament severing by vertebrate cofilin. *Proceedings of the National Academy of Sciences of the United States of America* **111**, 17821-17826 (2014).
24. L. Gressin, A. Guillotin, C. Guerin, L. Blanchoin, A. Michelot, Architecture dependence of actin filament network disassembly. *Curr Biol* **25**, 1437-1447 (2015).
25. H. Wioland *et al.*, ADF/Cofilin Accelerates Actin Dynamics by Severing Filaments and Promoting Their Depolymerization at Both Ends. *Curr Biol* **27**, 1956-1967 e1957 (2017).
26. D. V. Iwamoto *et al.*, Structural basis of the filamin A actin-binding domain interaction with F-actin. *Nat Struct Mol Biol* **25**, 918-927 (2018).
27. R. Niederman, P. C. Amrein, J. Hartwig, Three-dimensional structure of actin filaments and of an actin gel made with actin-binding protein. *J Cell Biol* **96**, 1400-1413 (1983).
28. Z. Razinia, T. Makela, J. Ylanne, D. A. Calderwood, Filamins in mechanosensing and signaling. *Annu Rev Biophys* **41**, 227-246 (2012).
29. B. Sjoblom, J. Ylanne, K. Djinovic-Carugo, Novel structural insights into F-actin-binding and novel functions of calponin homology domains. *Curr Opin Struct Biol* **18**, 702-708 (2008).
30. M. Gimona, K. Djinovic-Carugo, W. J. Kranewitter, S. J. Winder, Functional plasticity of CH domains. *FEBS Lett* **513**, 98-106 (2002).
31. S. Ruskamo, J. Ylanne, Structure of the human filamin A actin-binding domain. *Acta Crystallogr D Biol Crystallogr* **65**, 1217-1221 (2009).
32. A. R. Clark, G. M. Sawyer, S. P. Robertson, A. J. Sutherland-Smith, Skeletal dysplasias due to filamin A mutations result from a gain-of-function mechanism distinct from allelic neurological disorders. *Hum Mol Genet* **18**, 4791-4800 (2009).
33. S. P. Robertson, Filamin A: phenotypic diversity. *Curr Opin Genet Dev* **15**, 301-307 (2005).
34. A. Mentes *et al.*, High-resolution cryo-EM structures of actin-bound myosin states reveal the mechanism of myosin force sensing. *Proc Natl Acad Sci U S A* 10.1073/pnas.1718316115 (2018).
35. J. M. Laakso, J. H. Lewis, H. Shuman, E. M. Ostap, Myosin I can act as a molecular force sensor. *Science* **321**, 133-136 (2008).
36. J. Bamburg, Proteins of the ADF/cofilin family: Essential regulators of actin dynamics. *Annual Review of Cellular and Developmental Biology* **15**, 185-230 (1999).
37. A. McGough, B. Pope, A. Weeds, Cofilin changes the twist of F-actin: Implications for actin filament dynamics and cellular function. *Journal of Cell Biology* **138**, 771-781 (1997).
38. V. Galkin, A. Orlova, N. Lukoyanova, W. Wriggers, E. Egelman, Actin depolymerizing factor stabilizes and existing state of F-actin and can change the tilt of F-actin subunits. *Journal of Cell Biology* **153**, 75-86 (2001).
39. W. Elam, H. Kang, E. De La Cruz, Competitive displacement of cofilin can promote actin filament severing. *Biochemical and Biophysical Research Communications* **438**, 728-731 (2013).
40. E. De La Cruz, M. Gardel, Actin mechanics and fragmentation. *Journal of Biological Chemistry* **290**, 17137-17144 (2015).
41. S. M. Chin, S. Jansen, B. L. Goode, TIRF microscopy analysis of human Cof1, Cof2, and ADF effects on actin filament severing and turnover. *Journal of molecular biology* **428**, 1604-1616 (2016).
42. K. Tanaka *et al.*, Structural basis for cofilin binding and actin filament disassembly. *Nature Communications* **9**, 1860 (2018).

43. V. Galkin *et al.*, ADF/cofilin use an intrinsic mode of F-actin instability to disrupt actin filaments. *Journal of Cell Biology* **163**, 1057-1066 (2003).
44. A. Huehn *et al.*, The actin filament twist changes abruptly at boundaries between bare and cofilin-decorated segments. *J Biol Chem* 10.1074/jbc.AC118.001843 (2018).
45. E. H. Egelman, A robust algorithm for the reconstruction of helical filaments using single-particle methods. *Ultramicroscopy* **85**, 225-234 (2000).
46. E. Egelman, Reconstruction of helical filaments and tubes. *Methods in Enzymology* **482**, 167-183 (2010).
47. S. H. Scheres, RELION: implementation of a Bayesian approach to cryo-EM structure determination. *J Struct Biol* **180**, 519-530 (2012).
48. S. He, S. H. W. Scheres, Helical reconstruction in RELION. *J Struct Biol* **198**, 163-176 (2017).
49. T. Oda, M. Iwasa, T. Aihara, Y. Maeda, A. Narita, The nature of the globular- to fibrous-actin transition. *Nature* **457**, 441-445 (2009).
50. T. Fujii, A. Iwane, T. Yanagida, K. Namba, Direct visualization of secondary structures of F-actin by electron cryomicroscopy. *Nature* **467**, 724-728 (2010).
51. S. T. Huber, T. Kuhm, C. Sachse, Automated tracing of helical assemblies from electron cryo-micrographs. *Journal of structural biology* **202**, 1-12 (2018).
52. S. Z. Chou, T. D. Pollard, Mechanism of actin polymerization revealed by cryo-EM structures of actin filaments with three different bound nucleotides. *Proc Natl Acad Sci U S A* 10.1073/pnas.1807028115 (2019).
53. D. Pavlov, A. Muhlrad, J. Cooper, M. Wear, E. Reisler, Actin filament severing by cofilin. *Journal of Molecular Biology* **365**, 1350-1358 (2007).
54. T. Oda, S. Takeda, A. Narita, Y. Maeda, Structural Polymorphism of Actin. *J Mol Biol* **431**, 3217-3228 (2019).
55. B. Pope, S. Gonsior, S. Yeoh, A. McGough, A. Weeds, Uncoupling actin filament fragmentation by cofilin from increased subunit turnover. *Journal of Molecular Biology* **298**, 649-661 (2000).
56. A. Schramm *et al.*, Actin filament strain promotes severing and cofilin dissociation. *Biophysical Journal* **112**, 2624-2633 (2017).
57. A. C. Schramm, G. M. Hocky, G. A. Voth, J. L. Martiel, E. M. De La Cruz, Plastic Deformation and Fragmentation of Strained Actin Filaments. *Biophys J* **117**, 453-463 (2019).
58. E. De La Cruz, J. Martiel, L. Blanchoin, Mechanical heterogeneity favors fragmentation of strained actin filaments. *Biophysical Journal* **108**, 2270-2281 (2015).
59. X. F. Zhang *et al.*, Regulation of axon growth by myosin II-dependent mechanocatalysis of cofilin activity. *J Cell Biol* **218**, 2329-2349 (2019).
60. B. McCullough, L. Blanchion, J. Martiel, E. De La Cruz, Cofilin increases the bending flexibility of actin filaments: Implications for severing and cell mechanics. *Journal of Molecular Biology* **381**, 550-558 (2008).
61. E. De La Cruz, J. Roland, B. McCullough, L. Blanchoin, J. Martiel, Origin of twist-bend coupling in actin filaments. *Biophysical Journal* **99**, 1852-1860 (2010).
62. J. Fan *et al.*, Molecular origins of cofilin-linked changes in actin filament mechanics. *Journal of Molecular Biology* **425**, 1225-1240 (2013).
63. E. M. De La Cruz, T. D. Pollard, Nucleotide-free actin: stabilization by sucrose and nucleotide binding kinetics. *Biochemistry* **34**, 5452-5461 (1995).
64. S. Q. Zheng *et al.*, MotionCor2: anisotropic correction of beam-induced motion for improved cryo-electron microscopy. *Nat Methods* **14**, 331-332 (2017).
65. S. J. Ludtke, P. R. Baldwin, W. Chiu, EMAN: semiautomated software for high-resolution single-particle reconstructions. *J Struct Biol* **128**, 82-97 (1999).

66. D. Liu, X. Liu, Z. Shang, C. V. Sindelar, Structural basis of cooperativity in kinesin revealed by 3D reconstruction of a two-head-bound state on microtubules. *Elife* **6** (2017).
67. X. C. Bai, E. Rajendra, G. Yang, Y. Shi, S. H. Scheres, Sampling the conformational space of the catalytic subunit of human gamma-secretase. *Elife* **4** (2015).
68. E. Pettersen *et al.*, UCSF Chimera- A visualization system for exploratory research and analysis. *Journal of Computational Chemistry* **25**, 1605-1612 (2004).
69. G. Tang *et al.*, EMAN2: an extensible image processing suite for electron microscopy. *J Struct Biol* **157**, 38-46 (2007).
70. W. Kabsch, H. Mannherz, D. Suck, E. Pai, K. Holmes, Atomic structure of the actin:DNase I complex. *Nature* **347**, 37-44 (1990).
71. D. T. Gillespie, Exact Stochastic Simulation of Coupled Chemical-Reactions. *Abstr Pap Am Chem S* **173**, 128-128 (1977).
72. I. R. Epstein, Kinetics of Nucleic Acid Large Ligand Interactions - Exact Monte-Carlo Treatment and Limiting Cases of Reversible Binding. *Biopolymers* **18**, 2037-2050 (1979).
73. P. V. Afonine *et al.*, New tools for the analysis and validation of cryo-EM maps and atomic models. *Acta Crystallogr D Struct Biol* **74**, 814-840 (2018).
74. P. D. Adams *et al.*, PHENIX: a comprehensive Python-based system for macromolecular structure solution. *Acta Crystallogr D Biol Crystallogr* **66**, 213-221 (2010).
75. P. Emsley, B. Lohkamp, W. G. Scott, K. Cowtan, Features and development of Coot. *Acta Crystallogr D Biol Crystallogr* **66**, 486-501 (2010).
76. V. B. Chen *et al.*, MolProbity: all-atom structure validation for macromolecular crystallography. *Acta Crystallogr D Biol Crystallogr* **66**, 12-21 (2010).
77. T. Svitkina, The Actin Cytoskeleton and Actin-Based Motility. *Cold Spring Harb Perspect Biol* **10** (2018).
78. A. R. Bresnick, V. Warren, J. Condeelis, Identification of a short sequence essential for actin binding by Dictyostelium ABP-120. *J Biol Chem* **265**, 9236-9240 (1990).
79. B. A. Levine, A. J. Moir, V. B. Patchell, S. V. Perry, The interaction of actin with dystrophin. *FEBS Lett* **263**, 159-162 (1990).
80. A. M. Karinch, W. E. Zimmer, S. R. Goodman, The identification and sequence of the actin-binding domain of human red blood cell beta-spectrin. *J Biol Chem* **265**, 11833-11840 (1990).
81. B. A. Levine, A. J. Moir, V. B. Patchell, S. V. Perry, Binding sites involved in the interaction of actin with the N-terminal region of dystrophin. *FEBS Lett* **298**, 44-48 (1992).
82. K. Corrado, P. L. Mills, J. S. Chamberlain, Deletion analysis of the dystrophin-actin binding domain. *FEBS Lett* **344**, 255-260 (1994).
83. S. C. Goldsmith *et al.*, The structure of an actin-crosslinking domain from human fimbrin. *Nat Struct Biol* **4**, 708-712 (1997).
84. N. H. Keep *et al.*, Crystal structure of the actin-binding region of utrophin reveals a head-to-tail dimer. *Structure* **7**, 1539-1546 (1999).
85. F. L. Norwood, A. J. Sutherland-Smith, N. H. Keep, J. Kendrick-Jones, The structure of the N-terminal actin-binding domain of human dystrophin and how mutations in this domain may cause Duchenne or Becker muscular dystrophy. *Structure* **8**, 481-491 (2000).
86. J. Liu, D. W. Taylor, K. A. Taylor, A 3-D reconstruction of smooth muscle alpha-actinin by CryoEm reveals two different conformations at the actin-binding region. *J Mol Biol* **338**, 115-125 (2004).
87. V. E. Galkin, A. Orlova, O. Cherepanova, M. C. Lebart, E. H. Egelman, High-resolution cryo-EM structure of the F-actin-fimbrin/plastin ABD2 complex. *Proc Natl Acad Sci U S A* **105**, 1494-1498 (2008).

88. V. E. Galkin, A. Orlova, A. Salmazo, K. Djinovic-Carugo, E. H. Egelman, Opening of tandem calponin homology domains regulates their affinity for F-actin. *Nat Struct Mol Biol* **17**, 614-616 (2010).
89. A. Y. Lin, E. Prochniewicz, Z. M. James, B. Svensson, D. D. Thomas, Large-scale opening of utrophin's tandem calponin homology (CH) domains upon actin binding by an induced-fit mechanism. *Proc Natl Acad Sci U S A* **108**, 12729-12733 (2011).
90. M. J. Broderick, A. Bobkov, S. J. Winder, Utrophin ABD binds to F-actin in an open conformation. *FEBS Open Bio* **2**, 6-11 (2012).
91. A. W. Avery *et al.*, Structural basis for high-affinity actin binding revealed by a beta-III-spectrin SCA5 missense mutation. *Nat Commun* **8**, 1350 (2017).
92. F. Nakamura, T. M. Osborn, C. A. Hartemink, J. H. Hartwig, T. P. Stossel, Structural basis of filamin A functions. *J Cell Biol* **179**, 1011-1025 (2007).
93. F. Nakamura, T. P. Stossel, J. H. Hartwig, The filamins: organizers of cell structure and function. *Cell Adh Migr* **5**, 160-169 (2011).
94. V. L. Sheen *et al.*, Mutations in the X-linked filamin 1 gene cause periventricular nodular heterotopia in males as well as in females. *Hum Mol Genet* **10**, 1775-1783 (2001).
95. E. Parrini *et al.*, Periventricular heterotopia: phenotypic heterogeneity and correlation with Filamin A mutations. *Brain* **129**, 1892-1906 (2006).
96. M. H. Chen *et al.*, Thoracic aortic aneurysm in patients with loss of function Filamin A mutations: Clinical characterization, genetics, and recommendations. *Am J Med Genet A* **176**, 337-350 (2018).
97. G. Sole *et al.*, Bilateral periventricular nodular heterotopia in France: frequency of mutations in FLNA, phenotypic heterogeneity and spectrum of mutations. *J Neurol Neurosurg Psychiatry* **80**, 1394-1398 (2009).
98. S. P. Robertson, Otopalatodigital syndrome spectrum disorders: otopalatodigital syndrome types 1 and 2, frontometaphyseal dysplasia and Melnick-Needles syndrome. *Eur J Hum Genet* **15**, 3-9 (2007).
99. S. P. Robertson *et al.*, Localized mutations in the gene encoding the cytoskeletal protein filamin A cause diverse malformations in humans. *Nat Genet* **33**, 487-491 (2003).
100. Z. Razinia, M. Baldassarre, G. Cantelli, D. A. Calderwood, ASB2alpha, an E3 ubiquitin ligase specificity subunit, regulates cell spreading and triggers proteasomal degradation of filamins by targeting the filamin calponin homology 1 domain. *J Biol Chem* **288**, 32093-32105 (2013).
101. S. M. Singh, S. Bandi, K. M. G. Mallela, The N-Terminal Flanking Region Modulates the Actin Binding Affinity of the Utrophin Tandem Calponin-Homology Domain. *Biochemistry* **56**, 2627-2636 (2017).
102. A. Weins *et al.*, Disease-associated mutant alpha-actinin-4 reveals a mechanism for regulating its F-actin-binding affinity. *Proc Natl Acad Sci U S A* **104**, 16080-16085 (2007).
103. R. Valdes-Mas *et al.*, Mutations in filamin C cause a new form of familial hypertrophic cardiomyopathy. *Nat Commun* **5**, 5326 (2014).
104. R. D. Bagnall, L. K. Molloy, J. M. Kalman, C. Semsarian, Exome sequencing identifies a mutation in the ACTN2 gene in a family with idiopathic ventricular fibrillation, left ventricular noncompaction, and sudden death. *BMC Med Genet* **15**, 99 (2014).
105. S. Kunishima *et al.*, ACTN1 mutations cause congenital macrothrombocytopenia. *Am J Hum Genet* **92**, 431-438 (2013).
106. J. L. Theis *et al.*, Echocardiographic-determined septal morphology in Z-disc hypertrophic cardiomyopathy. *Biochem Biophys Res Commun* **351**, 896-902 (2006).

107. G. M. Sawyer, A. R. Clark, S. P. Robertson, A. J. Sutherland-Smith, Disease-associated substitutions in the filamin B actin binding domain confer enhanced actin binding affinity in the absence of major structural disturbance: Insights from the crystal structures of filamin B actin binding domains. *J Mol Biol* **390**, 1030-1047 (2009).
108. J. Kostan, M. Gregor, G. Walko, G. Wiche, Plectin isoform-dependent regulation of keratin-integrin alpha6beta4 anchorage via Ca2+/calmodulin. *J Biol Chem* **284**, 18525-18536 (2009).
109. J. G. Song *et al.*, Structural insights into Ca2+-calmodulin regulation of Plectin 1a-integrin beta4 interaction in hemidesmosomes. *Structure* **23**, 558-570 (2015).
110. F. Nakamura, J. H. Hartwig, T. P. Stossel, P. T. Szymanski, Ca2+ and calmodulin regulate the binding of filamin A to actin filaments. *J Biol Chem* **280**, 32426-32433 (2005).
111. B. Garcia-Alvarez, A. Bobkov, A. Sonnenberg, J. M. de Pereda, Structural and functional analysis of the actin binding domain of plectin suggests alternative mechanisms for binding to F-actin and integrin beta4. *Structure* **11**, 615-625 (2003).
112. T. Grant, N. Grigorieff, Automatic estimation and correction of anisotropic magnification distortion in electron microscopes. *J Struct Biol* **192**, 204-208 (2015).
113. K. Zhang, Gctf: Real-time CTF determination and correction. *Journal of Structural Biology* **193**, 1-12 (2016).
114. J. Hastings *et al.*, ChEBI in 2016: Improved services and an expanding collection of metabolites. *Nucleic Acids Res* **44**, D1214-1219 (2016).
115. N. W. Moriarty, R. W. Grosse-Kunstleve, P. D. Adams, electronic Ligand Builder and Optimization Workbench (eLBOW): a tool for ligand coordinate and restraint generation. *Acta Crystallogr D Biol Crystallogr* **65**, 1074-1080 (2009).
116. J. P. Gallivan, D. A. Dougherty, Cation-pi interactions in structural biology. *Proc Natl Acad Sci U S A* **96**, 9459-9464 (1999).
117. T. D. Goddard *et al.*, UCSF ChimeraX: Meeting modern challenges in visualization and analysis. *Protein Sci* **27**, 14-25 (2018).
118. S. M. Heissler, J. R. Sellers, Kinetic Adaptations of Myosins for Their Diverse Cellular Functions. *Traffic* **17**, 839-859 (2016).
119. M. J. Greenberg, G. Arpag, E. Tuzel, E. M. Ostap, A Perspective on the Role of Myosins as Mechanosensors. *Biophys J* **110**, 2568-2576 (2016).
120. A. Houdusse, H. L. Sweeney, How Myosin Generates Force on Actin Filaments. *Trends Biochem Sci* **41**, 989-997 (2016).
121. C. Veigel, J. E. Molloy, S. Schmitz, J. Kendrick-Jones, Load-dependent kinetics of force production by smooth muscle myosin measured with optical tweezers. *Nat Cell Biol* **5**, 980-986 (2003).
122. C. Veigel *et al.*, The motor protein myosin-I produces its working stroke in two steps. *Nature* **398**, 530-533 (1999).
123. C. Veigel, F. Wang, M. L. Bartoo, J. R. Sellers, J. E. Molloy, The gated gait of the processive molecular motor, myosin V. *Nat Cell Biol* **4**, 59-65 (2002).
124. M. Capitanio *et al.*, Two independent mechanical events in the interaction cycle of skeletal muscle myosin with actin. *Proc Natl Acad Sci U S A* **103**, 87-92 (2006).
125. S. F. Wulf *et al.*, Force-producing ADP state of myosin bound to actin. *Proc Natl Acad Sci U S A* **113**, E1844-1852 (2016).
126. M. Whittaker *et al.*, A 35-A movement of smooth muscle myosin on ADP release. *Nature* **378**, 748-751 (1995).

127. S. Munnich, M. H. Taft, D. J. Manstein, Crystal structure of human myosin 1c--the motor in GLUT4 exocytosis: implications for Ca2+ regulation and 14-3-3 binding. *J Mol Biol* **426**, 2070-2081 (2014).
128. S. Hayward, A. Kitao, H. J. Berendsen, Model-free methods of analyzing domain motions in proteins from simulation: a comparison of normal mode analysis and molecular dynamics simulation of lysozyme. *Proteins* **27**, 425-437 (1997).
129. C. A. Smith, I. Rayment, X-ray structure of the magnesium(II).ADP.vanadate complex of the Dictyostelium discoideum myosin motor domain to 1.9 A resolution. *Biochemistry* **35**, 5404-5417 (1996).
130. R. Dominguez, Y. Freyzon, K. M. Trybus, C. Cohen, Crystal structure of a vertebrate smooth muscle myosin motor domain and its complex with the essential light chain: visualization of the pre-power stroke state. *Cell* **94**, 559-571 (1998).
131. H. Shuman *et al.*, A vertebrate myosin-I structure reveals unique insights into myosin mechanochemical tuning. *Proc Natl Acad Sci U S A* **111**, 2116-2121 (2014).
132. M. J. Greenberg, T. Lin, H. Shuman, E. M. Ostap, Mechanochemical tuning of myosin-I by the N-terminal region. *Proc Natl Acad Sci U S A* **112**, E3337-3344 (2015).
133. A. C. Wallace, R. A. Laskowski, J. M. Thornton, LIGPLOT: a program to generate schematic diagrams of protein-ligand interactions. *Protein Eng* **8**, 127-134 (1995).
134. I. Rayment *et al.*, Three-dimensional structure of myosin subfragment-1: a molecular motor. *Science* **261**, 50-58 (1993).
135. J. von der Ecken, S. M. Heissler, S. Pathan-Chhatbar, D. J. Manstein, S. Raunser, Cryo-EM structure of a human cytoplasmic actomyosin complex at near-atomic resolution. *Nature* **534**, 724-728 (2016).
136. M. Lorenz, D. Popp, K. C. Holmes, Refinement of the F-actin model against X-ray fiber diffraction data by the use of a directed mutation algorithm. *J Mol Biol* **234**, 826-836 (1993).
137. T. Oda, K. Namba, Y. Maeda, Position and orientation of phalloidin in F-actin determined by X-ray fiber diffraction analysis. *Biophys J* **88**, 2727-2736 (2005).
138. M. O. Steinmetz *et al.*, Evaluating atomic models of F-actin with an undecagold-tagged phalloidin derivative. *J Mol Biol* **276**, 1-6 (1998).
139. T. Fujii, A. H. Iwane, T. Yanagida, K. Namba, Direct visualization of secondary structures of F-actin by electron cryomicroscopy. *Nature* **467**, 724-728 (2010).
140. R. Dominguez, K. C. Holmes, Actin structure and function. *Annu Rev Biophys* **40**, 169-186 (2011).
141. S. Pospich *et al.*, Near-atomic structure of jasplakinolide-stabilized malaria parasite F-actin reveals the structural basis of filament instability. *Proc Natl Acad Sci U S A* 10.1073/pnas.1707506114 (2017).
142. D. G. Drubin, H. D. Jones, K. F. Wertman, Actin structure and function: roles in mitochondrial organization and morphogenesis in budding yeast and identification of the phalloidin-binding site. *Mol Biol Cell* **4**, 1277-1294 (1993).
143. J. M. Laakso, J. H. Lewis, H. Shuman, E. M. Ostap, Control of myosin-I force sensing by alternative splicing. *Proc Natl Acad Sci U S A* **107**, 698-702 (2010).
144. T. Lin, N. Tang, E. M. Ostap, Biochemical and motile properties of Myo1b splice isoforms. *J Biol Chem* **280**, 41562-41567 (2005).
145. C. Suloway *et al.*, Automated molecular microscopy: the new Leginon system. *J Struct Biol* **151**, 41-60 (2005).
146. K. Zhang, Gctf: Real-time CTF determination and correction. *J Struct Biol* **193**, 1-12 (2016).

147. S. C. Reddington, M. Howarth, Secrets of a covalent interaction for biomaterials and biotechnology: SpyTag and SpyCatcher. *Curr Opin Chem Biol* **29**, 94-99 (2015).
148. G. Lebreton *et al.*, Molecular to organismal chirality is induced by the conserved myosin 1D. *Science* **362**, 949-952 (2018).